The Astrophysical Journal Supplement Series, 235:7 (40pp), 2018 March https://doi.org/10.3847/1538-4365/aaa89c

The 7-year *MAXI*/GSC Source Catalog of the Low-Galactic-latitude Sky (3MAXI)

T. Hori[1], M. Shidatsu[2], Y. Ueda[1], T. Kawamuro[3], M. Morii[4], S. Nakahira[2], N. Isobe[5], N. Kawai[6], T. Mihara[2], M. Matsuoka[2], T. Morita[1], M. Nakajima[7], H. Negoro[8], S. Oda[1], T. Sakamoto[9], M. Serino[9], M. Sugizaki[2], A. Tanimoto[1], H. Tomida[10], Y. Tsuboi[11], H. Tsunemi[12], S. Ueno[10], K. Yamaoka[13], S. Yamada[1], A. Yoshida[14], W. Iwakiri[2], Y. Kawakubo[9], Y. Sugawara[15], S. Sugita[6], Y. Tachibana[6], and T. Yoshii[6]

[1] Department of Astronomy, Kyoto University, Kitashirakawa-Oiwake-cho, Sakyo-ku, Kyoto 606-8502, Japan; hori@kusastro.kyoto-u.ac.jp
[2] MAXI team, RIKEN, 2-1, Hirosawa, Wako-shi, Saitama 351-0198, Japan
[3] National Astronomical Observatory of Japan, Osawa, Mitaka, Tokyo 181-8588, Japan
[4] The Institute of Statistical Mathematics, 10-3 Midori-cho, Tachikawa, Tokyo 190-8562, Japan
[5] School of Science, Tokyo Institute of Technology, 2-12-1 Ookayama, Meguro, Tokyo 152-8551, Japan
[6] Department of Physics, Tokyo Institute of Technology, 2-12-1 Ookayama, Meguro-ku, Tokyo 152-8551, Japan
[7] School of Dentistry at Matsudo, Nihon University, 2-870-1, Sakaecho-nishi, Matsudo, 271-8587, Chiba, Japan
[8] Department of Physics, Nihon University, 1-8 Kanda-Surugadai, Chiyoda-ku, Tokyo 101-8308, Japan
[9] College of Science and Engineering, Department of Physics and Mathematics, Aoyama Gakuin University, 5-10-1 Fuchinobe, Chuo-ku, Sagamihara, Kanagawa 252-5258, Japan
[10] Institute of Space and Astronautical Science, Japan Aerospace Exploration Agency, 3-1-1 Yoshinodai, Chuo, Sagamihara, Kanagawa 252-5210, Japan
[11] Department of Physics, Faculty of Science & Engineering, Chuo University, 1-13-27 Kasuga, Bunkyo, Tokyo 112-8551, Japan
[12] Department of Earth and Space Science, Graduate School of Science, Osaka University, 1-1 Machikaneyama-cho, Toyonaka, Osaka 560-0043, Japan
[13] Institute for Space-Earth Environmental Research (ISEE), Nagoya University, Furo-cho, Chikusa-ku, Nagoya, Aichi 464-8601, Japan
[14] College of Science and Engineering, Department of Physics and Mathematics, Aoyama Gakuin University, 5-10-1 Fuchinobe, Chuo, Sagamihara, Kanagawa 252-5258, Japan
[15] Institute of Space and Astronautical Science, Japan Aerospace Exploration Agency, 3-1-1 Yoshinodai, Sagamihara, Kanagawa 252-5210, Japan
Received 2017 October 4; revised 2018 January 9; accepted 2018 January 10; published 2018 February 26

Abstract

We present the first MAXI/GSC X-ray source catalog in the low-Galactic-latitude sky $|b| < 10°$ outside the Galactic center region ($|b| < 5°$, $l < 30°$, and $l > 330°$) based on 7-year data from 2009 August 13 to 2016 July 31. To overcome source confusion in crowded regions, we have accurately calibrated the position-dependent shape of the point-spread function of the MAXI/GSC by analyzing onboard data. We have also taken into account the Galactic ridge X-ray emission. Using a maximum likelihood image fitting method, we have detected 221 sources with a significance threshold $>6.5\sigma$, 7 of which are transients only detected in 73-day time-sliced images. The faintest source has a flux of 5.2×10^{-12} erg cm^{-2} s^{-1} (or an intensity of 0.43 mCrab) in the 4–10 keV band. We have identified the counterparts for about 81% of the detected sources, by cross-matching with the *Swift*, *Uhuru*, *RXTE*, *XMM-Newton*, MCXC, and *ROSAT* all-sky survey catalogs. Our catalog contains the source name, position and its error, flux and detection significance in the 3–4 keV, 4–10 keV, and 10–20 keV bands, hardness ratios, and information on the likely counterpart for the individual detected sources. We have obtained 73-day bin light curves of all the cataloged sources over 7 years and have calculated their periodograms. On the basis of the mean properties of time variability and spectral hardness, we suggest that the majority of the unidentified sources are low-mass X-ray binaries or blazars. Finally, we present the log N–log S relations at different Galactic longitudes and for different source populations.

Key words: catalogs – surveys – X-rays: binaries

1. Introduction

Demographic studies of Galactic X-ray sources provide important clues for understanding the evolutionary history of our Galaxy. Many X-ray emitters over the sky, such as X-ray binaries, supernova remnants, and cataclysmic variables, form classes of objects at their last evolutionary stages, and their formation and evolution must have been influenced by their environments. This is reflected in the current spatial and luminosity distributions of each class of Galactic X-ray sources. Complete X-ray source catalogs in the Galactic plane become the basis for such statistical studies.

Since the majority of Galactic sources are subject to heavy interstellar absorption, observations in hard X-rays above a few keV are essential. Deep imaging observations of the Galactic plane have been conducted by various X-ray observatories covering energies above 2 keV, such as *ASCA* (Sugizaki et al. 2001), *Chandra* (Ebisawa et al. 2005; Grindlay et al. 2005), and *XMM-Newton* (Hands et al. 2004; Nebot Gómez-Morán et al. 2013). While these observations achieve high sensitivities, they cover limited regions around the Galactic center or at very low Galactic latitudes. Wider area surveys that completely cover the low-Galactic-latitude region are necessary to provide a complete picture of Galactic X-ray populations.

The Monitor of All-sky X-ray Image (MAXI; Matsuoka et al. 2009) is an all-sky X-ray monitor on board the *International Space Station* (ISS), and has been operating for more than 8 years since 2009 August. Its main instrument, the Gas Slit Camera (GSC; Mihara et al. 2011), covers the energy band of 2–30 keV and scans nearly the entire sky every 92 minutes, with an instant field of view of $3.^{\circ}0 \times 160°$. The GSC is composed of 12 one-dimensional gas counters (GSC0 to GSC9, GSCA, and GSCB) with slat collimators attached on the individual counters. Of the 12 units, 6 are placed in front of MAXI, and the others are on top of it, producing wide rectangular fields of view in the horizontal and zenithal directions (see Mihara et al. 2011, for more detailed information). The exposure time of a point source is ∼40–140 s for 1 counter and 1 scan. The scan duration of a counter is longer for a source located closer to the pole of the ISS rotation (Sugizaki et al. 2011). The effective area of a point source is proportional to $\cos(\phi)$, where ϕ is the photon incident angle along the collimators. The typical value is $\sim$5 cm^2 at a scan angle of $0°$ (Sugizaki et al. 2011). For each event, its recorded time and ϕ value (estimated from the detected position along the anode direction and the energy) are converted into celestial coordinates by referring to the attitude data of MAXI (Sugizaki et al. 2011).

The MAXI/GSC achieves the highest sensitivity in the 4–10 keV band among the previous and on-going all-sky surveys, such as the *Uhuru* (Forman et al. 1978), *HEAO-1* (Wood et al. 1984), and *RXTE* slew surveys (Revnivtsev et al. 2004), and is complementary to those in the soft X-ray band below 2 keV (*ROSAT*: Voges et al. 1999) and above 10 keV (*INTEGRAL*: Bird et al. 2007, 2010, 2016; Ebisawa et al. 2003; and *Swift*: Baumgartner et al. 2013; Oh et al. 2018). In particular, the 4–10 keV band survey has the advantage of detecting X-ray populations with soft spectra without suffering from absorption as long as the hydrogen column density is smaller than $\sim 10^{23}$ cm^{-2}. In addition, MAXI provides us with a unique opportunity to study the long-term variability of each object, thanks to its almost continuous all-sky monitoring for >7 years.

While the MAXI/GSC source catalogs in the high-Galactic-latitude region, $|b| > 10°$, were released by Hiroi et al. (2011) and Hiroi et al. (2013) from the first 7-month and 38-month data, respectively, the catalog in the low-latitude region below $|b| = 10°$ has not been produced yet. This is mainly because the Galactic plane region is heavily crowded with sources and is contaminated by the Galactic Ridge X-ray Emission (GRXE), making it difficult to separate signals from individual X-ray sources and determine their positions and fluxes accurately. In this case, it is crucial to accurately estimate the spatial distribution of the GRXE and to reduce systematic uncertainties in the point-spread function (PSF) of the GSC.

In this paper, we present the first MAXI/GSC source catalog for $|b| < 10°$ in the 4–10 keV band produced by integrating the 7 year data from 2009 August 13 to 2016 July 31. We utilize the same image fitting technique as that employed in the 37-month catalog (Hiroi et al. 2013). To overcome source confusion, we calibrate the position-dependent shape of the GSC PSF and estimate the contribution of the GRXE. We also determine the 3–4 keV and 10–20 keV fluxes of the individual detected sources, to calculate their hardness ratios (HRs). For the remaining sky area ($|b| > 10°$), a new source catalog, which is an updated version of Hiroi et al. (2013) and complementary to ours, will be provided in another paper (T. Kawamuro et al. 2018, in preparation).

Sections 2 and 3 describe the data reduction and analysis, respectively. The PSF calibration is summarized in the Appendix. The resultant source catalog and its properties are described in Section 4, and our conclusions are given in Section 5. We define the fluxes of the MAXI sources in Crab units (i.e., relative to the 7-year averaged flux of the Crab Nebula) unless otherwise stated. The Crab Nebula spectrum is assumed to be an absorbed power-law model,[16] with a column density of 2.6×10^{21} cm^{-2}, a photon index of 2.1, and a normalization at 1 keV of 10.0 photons cm^{-2} s^{-1} keV^{-1}, which corresponds to 3.98×10^{-9}, 1.21×10^{-8}, and 8.51×10^{-9} erg cm^{-2} s^{-1} in the 3–4 keV, 4–10 keV, and 10–20 keV bands, respectively.

2. Data Reduction

We used the MAXI/GSC cleaned event data version 1.8 from 2009 August 13 to 2016 July 31, and reduced them with essentially the same method as that in the MAXI/GSC 37-month high-latitude catalog (Hiroi et al. 2013). The data reduction was carried out with MXSOFT, which is an original software package developed by the MAXI team, and Heasoft version 6.15. We ignored the cameras operated at the nominal high-voltage levels (1650 V or 1550 V) for only less than 1 year (GSC6, GSC9, GSCa). The GSC0 data after 2013 June 15, when the detector was leaking its gas, were not used either. We also discarded the data from GSC3, which have large systematic uncertainties in position calibration and suffer from high background levels due to damage to its veto cells (Sugizaki et al. 2011).

The data screening was performed with mostly the same selection criteria as those adopted in Hiroi et al. (2013). The only differences from the previous work were that (1) we found that the contamination of the calibration sources is not negligible in the edge of some GSC counters, and thus imposed a tighter restriction on the incident angles of photons, $|\phi| < 36.8°$, where the incident angle ϕ is defined by the photon-detected position on the detector (see Mihara et al. 2011, for more detail), and that (2) we excluded the events acquired when the attitude data files, which are needed in the source/background simulations described below, were unavailable or contained incorrect values.[17] These changes were made to remove any possible systematic errors and to improve the sensitivity for detecting faint sources in the crowded regions on and around the Galactic plane. They only negligibly affect the results from the previous high-latitude catalogs.

Figure 1 presents the coverage map created after the data screening. We utilized the MAXI event simulator "*maxisim*" (Eguchi et al. 2009), which generates events from X-ray point/diffuse sources based on the input energy spectra and source position (and spatial distribution for extended sources). Referring to the calibration database and the attitude orbit, and time data included in the auxiliary files provided by the MAXI team, it correctly considers the angle dependence of the slit area, the collimator field of view, and the responses of the individual GSC cameras. The large-scale patterns seen in the coverage map reflect the difference in the duty cycles and the operation periods of the individual GSC cameras and the dependence of the directions of their field of view on the ISS orbit.

3. Analysis

We performed an image analysis in basically the same way as that described in Hiroi et al. (2013), fully taking into account

[16] The spectral parameters are adopted from the *INTEGRAL* General Reference Catalog (version 40): http://www.isdc.unige.ch/integral/science/catalogue. One has to bear in mind that the X-ray flux of the Crab Nebula is not constant (Wilson-Hodge et al. 2011), which could cause a systematic uncertainty of a few percent levels in the absolute flux calibration.

[17] We ignored the event data taken when (a) the interval of two neighboring attitude data is >60 s, and/or (b) the attitude quaternions of two neighboring data, $\boldsymbol{q} = (q_1, q_2, q_3, q_4)$ and $\boldsymbol{q}' = (q_1', q_2', q_3', q_4')$, have unusually large or small differences. For the latter condition, we defined $\Delta q = \sqrt{\Sigma_{i=1}^{4}(q_i - q_i')^2} \geqslant 2.5 \times 10^{-4}$ and $\Delta q \leqslant 1.5 \times 10^{-3}$, considering the trend in Δq for the whole period of MAXI operation. The data taken 30 s before and after the periods with these bad conditions were additionally removed.

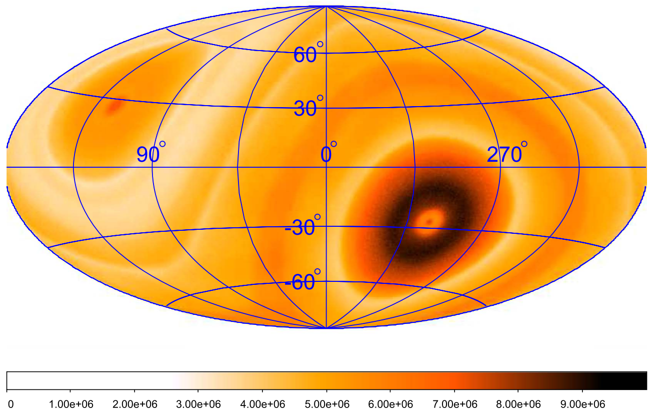

Figure 1. Coverage map for the 7-year MAXI/GSC data for $|b| < 10°$ in Galactic coordinates projected with the Hammer–Aitoff projection. The units are cm^2 s.

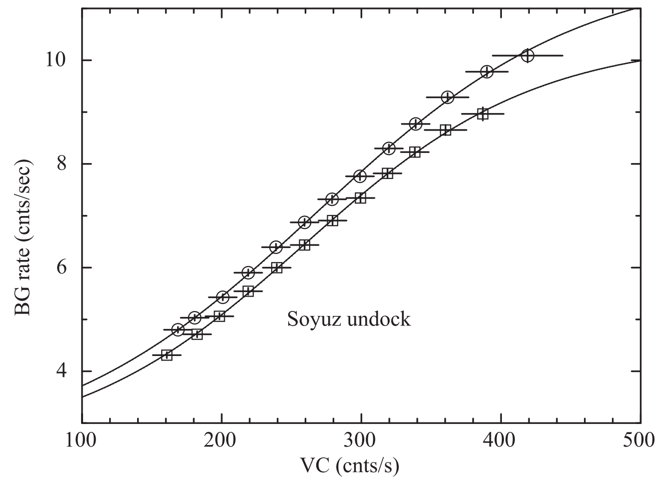

Figure 2. Correlations between the VC count rates vs. the 3–20 keV background event rates of GSC2, when the Russian spacecraft *Soyuz* was not present on the docking port close to MAXI. The data are fitted with the function $f(\mathrm{VC}) = a + b/(1 + c \times \exp(-d(\mathrm{VC} - e)))$, where $a \sim e$ are free parameters. The open circles and squares plot the data when the *ISS* travels northward and southward, respectively.

the image response and background contribution. We first divided the entire sky into 768 square regions with a size of 7°.3 × 7°.3 in the sky coordinates (see Hiroi et al. 2013, for the definition), whose central positions were determined through the Healpix software package (Górski et al. 2005), and produced tangentially projected images from the screened event data. We next made the list of source candidates in each image, and constructed the models of the PSFs of these sources. Finally, we estimated their positions and fluxes by fitting the individual images with the model composed of the PSFs and the other contributors: the non-X-ray background (NXB), the cosmic X-ray background (CXB), and the GRXE. The normalizations of the PSFs give the source fluxes in Crab units, because we measure the total count rates relative to those of the PSFs simulated on the basis of the Crab Nebula spectrum. To make the source search complete, the last two steps were iterated by including additional sources that appeared as positive residual signals in the previous image fitting. We found, however, serious source confusion was unavoidable in the Galactic center region within $|b| < 5°$, $l < 30°$, and $l > 330°$. Because faint sources with significances of $\sim 6.5\sigma$ were difficult to detect, we excluded the images in that region in this image analysis. The complete catalog in this region will be provided in a future paper.

Following Hiroi et al. (2013), the data in 4–10 keV, where a high signal-to-noise ratio can be achieved, were used to detect X-ray sources, while energy fluxes in the 3–4 keV and 10–20 keV bands were also estimated for all the detected sources, to derive their spectral information. In the next subsections, we describe the details of our analysis, mainly focusing on the procedures that are different from those adopted in Hiroi et al. (2013).

3.1. Background Modeling

We constructed the model of the GSC background, by which we mean the combination of the NXB and the CXB, in the same manner as Hiroi et al. (2013), using the so-called "VC" count rate (the rate of the coincident events between a carbon anode for signal detection and a veto anode) as a tracer of the intensity and energy distribution of the GSC background. Unlike the previous works, we created the background models separately for the periods when the ISS moves northward and southward. Figure 2 demonstrates the difference in the correlation of the background rate and the VC count rate between the direction of ISS motion; the background rate tends to be higher when the *ISS* travels from north to south than it is when it travels from south to north. This trend was found to be seen in all the cameras. More detailed properties of the GSC background will be described in a future paper (M. Shidatsu et al. 2018, in preparation).

We produced simulated background data based on our newly created model, utilizing *maxisim*. We found that our new background model improved the reproducibility of the GSC background strength, especially above $\sim$5 keV. The simulated data were processed in exactly the same way as the real event data, before being used in the image fitting. We produced 10 times more events than what was predicted from the actual background level, so that the statistical errors in the model became negligible compared with the real data.

3.2. GRXE Modeling

To detect faint sources in the low-Galactic-latitude region, we have to estimate the contribution of GRXE accurately. The GRXE can be separated into two emission components: the Galactic bulge (or bar) and disk (Cooke et al. 1970; Yamauchi & Koyama 1993). Following Revnivtsev et al. (2006), we modeled these components with an ellipsoid plus disk profile, adopting the parameters given in Table 1 of that work. On the basis of this model, we created the simulated GRXE data through *maxisim*, processed them with the same criteria as the real data and simulated background data, and incorporated them in the image analysis. Because the intensity of the GRXE is much lower than the level of NXB+CXB, we adopted 50 times higher intensity than that of the actual GRXE in the simulation, to reduce statistical errors. Because this geometrical model gives only an approximation of the large-scale profile of the GRXE, its normalization was left as a free parameter in the image analysis to allow a small adjustment of its local flux level. We have confirmed that a constant correction factor over each image (11° × 11°) improves the fit sufficiently well.

Table 1
Conversion Factors in the Energy Bands of 3–4 keV, 4–10 keV, and 10–20 keV in Units of 10^{-11} erg cm^{-2} s^{-1} mCrab^{-1}

		Photon Index in Power Law (Γ)							
		1.0	1.5	1.7	1.9	2.1	2.3	2.5	3.0
3–4 keV	$\log(N_{\rm H}) = 21$	0.409	0.404	0.402	0.399	0.396	0.392	0.389	0.380
	$\log(N_{\rm H}) = 22$	0.413	0.409	0.407	0.404	0.401	0.398	0.395	0.386
	$\log(N_{\rm H}) = 23$	0.440	0.446	0.446	0.446	0.445	0.443	0.442	0.437
4–10 keV	$\log(N_{\rm H}) = 21$	1.288	1.264	1.249	1.231	1.212	1.192	1.171	1.119
	$\log(N_{\rm H}) = 22$	1.292	1.271	1.255	1.238	1.219	1.199	1.179	1.127
	$\log(N_{\rm H}) = 23$	1.330	1.323	1.312	1.298	1.282	1.265	1.247	1.200
10–20 keV	$\log(N_{\rm H}) = 21$	0.917	0.895	0.882	0.867	0.851	0.835	0.818	0.776
	$\log(N_{\rm H}) = 22$	0.918	0.896	0.883	0.868	0.852	0.836	0.819	0.777
	$\log(N_{\rm H}) = 23$	0.928	0.907	0.894	0.879	0.864	0.848	0.831	0.788

3.3. PSF Modeling, Source Finding, and Position/Flux Measurements

To minimize the complexity with source confusion, which is more severe at lower Galactic latitudes, we searched for new sources after identifying those listed in the *Swift*/BAT 105 month catalog[18] (hereafter BAT105 Oh et al. 2018), instead of a blind source search as performed by Hiroi et al. (2013). We adopted the *Swift*/BAT catalog, which covers the hard X-ray band in 14–195 keV, as a reference catalog, instead of catalogs in the soft X-ray band below 10 keV, because hard X-rays have stronger penetrating power than soft X-rays and give a more complete catalog. We first prepared the PSF models for all the sources in the *Swift*/BAT 105 month catalog by simulating their photon distributions with *maxisim*, assuming the same conditions as the actual observations with the GSC. Here, we used our newly created calibration database for the PSF of the GSC (see the Appendix for details). As the input source positions and spectra, we adopted the coordinates of the optical counterparts, and for simplicity, the canonical model of the Crab Nebula (see Section 1) for all the sources, respectively. We also assumed that the flux was constant in the PSF simulation; this means that we would obtain a time-averaged flux when the source was variable. We have confirmed that the spectral difference from the Crab Nebula and the observed time variability has little effect on the integrated PSF shape and hence does not affect our results.

We fit the individual images created from the real data, with a model consisting of the background, GRXE, and PSF components, using the MINUIT package[19] in root version 6.06/08. Besides the fluxes of the sources, we also made the normalization of the background and that of the GRXE free parameters, to take into account possible small spatial-variation of the fluxes of the CXB and the GRXE (see above). Because the peak positions of the PSF models could be shifted from the actual positions in the GSC images by $\sim0.^{\circ}05$, presumably due to systematic errors in the alignment of attitude data, we allowed the source positions to vary within $0.^{\circ}1$ from the original coordinates. The best-fit parameters were determined on the basis of the Poisson likelihood algorithm (so-called *C*-statistics; Cash 1979). We defined the detection significance in the 4–10 keV band as

$$s_{D,4\text{–}10\,\mathrm{keV}} = \frac{\text{(best-fit 4–10 keV flux)}}{(\text{its } 1\sigma \text{ statistical error})}, \quad (1)$$

where we adopted the "MINOS" negative error calculated with the MINUIT package for the 1σ error. The flux was obtained in Crab units, because we basically measure the count rate relative to that of the Crab Nebula through the PSF fitting.

As a next step, we searched for source candidates that were not detected in the *Swift*/BAT catalog, utilizing the residual map of the previous image fitting, in the same manner as Hiroi et al. (2013). We smoothed the residual map with a circle of $r = 1^{\circ}$ with a constant weight of unity, and calculated the excess-signal significance as "$\mathrm{St}/\sqrt{\mathrm{St} + \mathrm{Bt}}$" at each point, where S and B are the count rate of the source and background signals, respectively, and t is the exposure time. Here, we adopted a conservative criterion, $>4\sigma$, in finding new source candidates. We then constructed the PSF models for those candidates and added them in the model to be used for the next image fitting, which determined the detection significances defined by Equation (1) for all the sources. We repeated these procedures (source search, PSF modeling, and image fitting) two times, not to miss any nearby sources, and obtained the final source list with $s_{D,4\text{–}10\,\mathrm{keV}}$. We ignored, however, the circular region with a radius of 3° around the Vela supernova remnant. Because its size is substantially larger than that of the PSF, significant residuals remained after the image fitting and it was difficult to detect any other sources in that region. Also, in the final catalog we excluded sources detected close to much brighter ones if their flux levels were lower than possible systematic errors in the PSF model of the nearby target (if the flux is $<1\%$ and $<0.4\%$ of the latter at a distance of 1°–2° and 2°–3°, respectively; see the Appendix).

We chose $s_{D,4\text{–}10\,\mathrm{keV}} = 6.5$ as the detection threshold to reduce the number of fake sources caused by background fluctuation (both statistical and systematic ones). In order to estimate it, we searched for negative signals in the smoothed residual map and performed image fitting to them using negative PSF models. Assuming that the systematic errors in the background model are symmetric in positive and negative sides, we estimate that $\sim$5 spurious sources may be detected in the Galactic plane region ($|b| \leqslant 10^{\circ}$) with a significance of

[18] Twelve MAXI sources in our final catalog are associated with *Swift*/BAT 105 month sources that were not detected in the *Swift*/BAT 70 month catalog (Baumgartner et al. 2013).
[19] CERN Program Library Long Writeup D506; https://cern-tex.web.cern.ch/cern-tex/minuit/minmain.html.

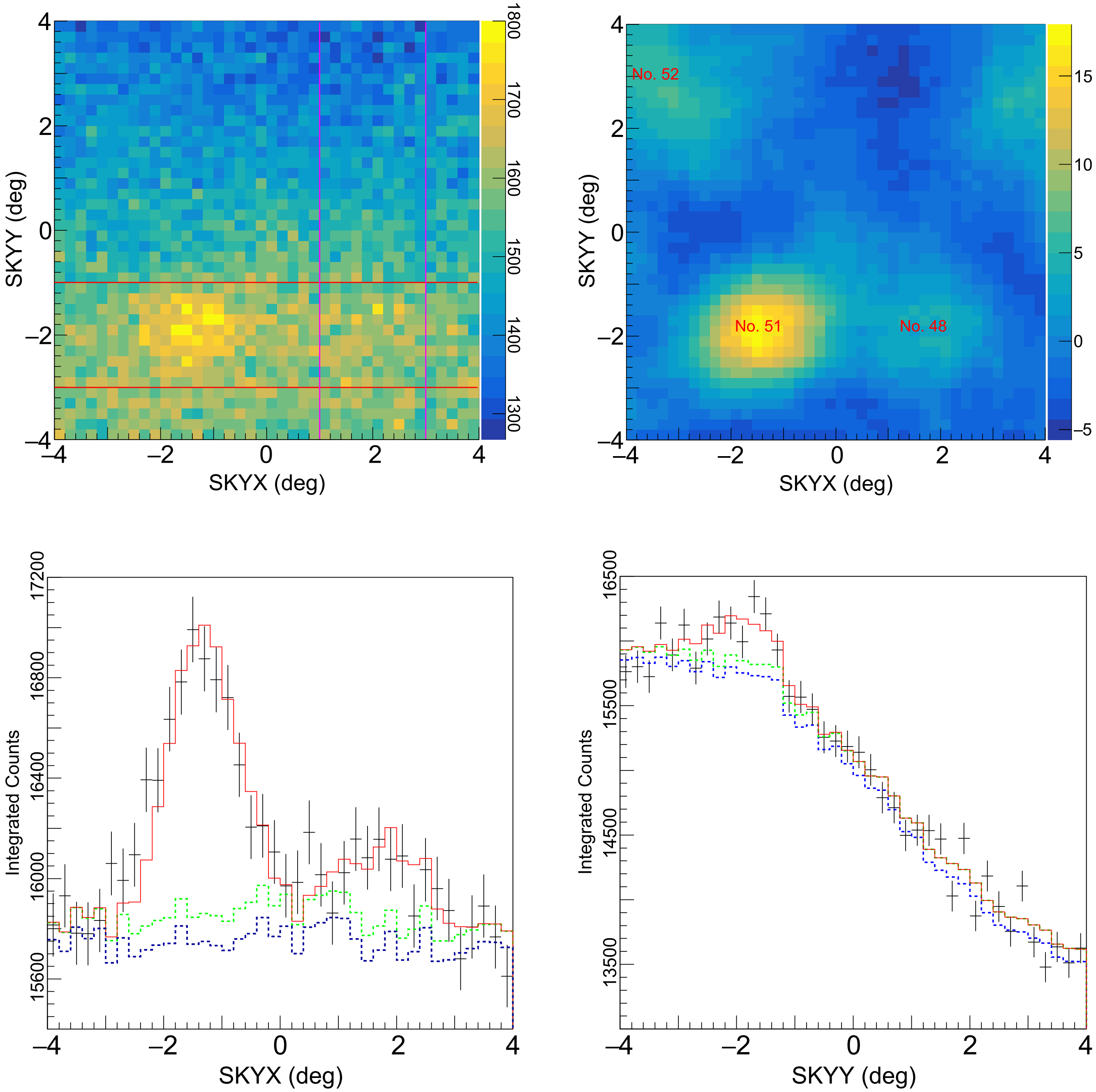

Figure 3. Example of our image analysis. The image size is $8^\circ \times 8^\circ$ and its center is located at (R.A., decl.) = (107°.89, −9°.59). Upper left: the observed image. Upper right: the smoothed significance map (see the text), where the positions of detected sources (No. 48, No. 51, and No. 52) are marked in red. Lower left (right): the projected image onto the X (Y) axis in the region between the two red (magenta) lines indicated in the upper left panel. The black points represent the data with 1σ errors. The red solid, green dotted, and blue dotted lines represent the best-fit models of the total (PSFs + background), the background (NXB+CXB+GRXE), and that without the GRXE, respectively.

$\geqslant 6.5\sigma$. We note that 11 spurious sources will be found in the case of $s_{D,4-10\,\mathrm{keV}} \geqslant 6.0$, which is too many to be accepted. The number of spurious sources was reduced to 3 and 1 in the case of $s_{D,4-10\,\mathrm{keV}} \geqslant 7.0$ and $\geqslant 8.0$, respectively.

Figure 3 shows an example of our image analysis. In this image, 3 sources are detected with $s_{D,4-10\,\mathrm{keV}} > 6.5$ (Nos. 48, 51, and 52). We plot the observed image in photon counts, the smoothed significance map, and the projected profiles of the observed image around source No. 48 onto the X and Y axes with their best-fit models.

3.4. 73-day Sources

To make a complete catalog it is essential to search for transient sources that are not detected with $s_{D,4-10\,\mathrm{keV}} > 6.5$ in the 7-year integrated map. To find these transient sources, we applied our image analysis method (Section 3.3) to 73-day (i.e., 0.2 year) integrated GSC images and obtained the light curve of each source with those time bins. We searched for sources with $s_{D,4-10\,\mathrm{keV}} > 6.5$ in the 73-day integrated images, and found 7 additional sources. Hereafter, we refer to these 7 sources as "73-day sources."

Table 2
HR1(3–4 keV, 4–10 keV), HR2(4–10 keV, 10–20 keV) in a Power-law-like Spectrum

		Photon Index in Power Law (Γ)							
		1.0	1.5	1.7	1.9	2.1	2.3	2.5	3.0
HR1	$\log(N_H) = 21$	0.32	0.17	0.11	0.05	−0.01	−0.06	−0.11	−0.24
	$\log(N_H) = 22$	0.35	0.20	0.15	0.09	0.03	−0.02	−0.08	−0.20
	$\log(N_H) = 23$	0.62	0.51	0.47	0.42	0.37	0.33	0.28	0.15
HR2	$\log(N_H) = 21$	0.40	0.23	0.15	0.08	−0.00	−0.08	−0.16	−0.35
	$\log(N_H) = 22$	0.41	0.24	0.17	0.09	0.01	−0.07	−0.15	−0.34
	$\log(N_H) = 23$	0.48	0.33	0.27	0.20	0.13	0.05	−0.03	−0.21

Table 3
Number of Matched Sources for the 7-year Sources

Catalog Name	BAT105	4U	XTEASMLONG	XMMSL2	MCXC	1RXS	One Catalog Only[a]
BAT105	143	⋯	⋯	⋯	⋯	⋯	143
4U	⋯	4(4)[b]	3	3	1	2	0
XTEASMLONG	⋯	⋯	8(9)[b]	2	1	2	5
XMMSL2	⋯	⋯	⋯	12(16)[b]	1	8	7
MCXC	⋯	⋯	⋯	⋯	8(9)[b]	2	6
1RXS	⋯	⋯	⋯	⋯	⋯	14(14)[b]	4
Number of Matched Sources for the 73-day Sources							
BAT105	1	⋯	⋯	⋯	⋯	⋯	1
4U	⋯	1(1)[b]	1	0	0	0	0
XTEASMLONG	⋯	⋯	4(4)[b]	0	0	0	3
XMMSL2	⋯	⋯	⋯	1(1)[b]	0	0	1
MCXC	⋯	⋯	⋯	⋯	0(0)[b]	0	0
1RXS	⋯	⋯	⋯	⋯	⋯	0(0)[b]	0

Notes.
[a] Number of MAXI sources matched only with one catalog given in the first column.
[b] Numbers in parentheses represent those of total matched counterparts in each catalog.

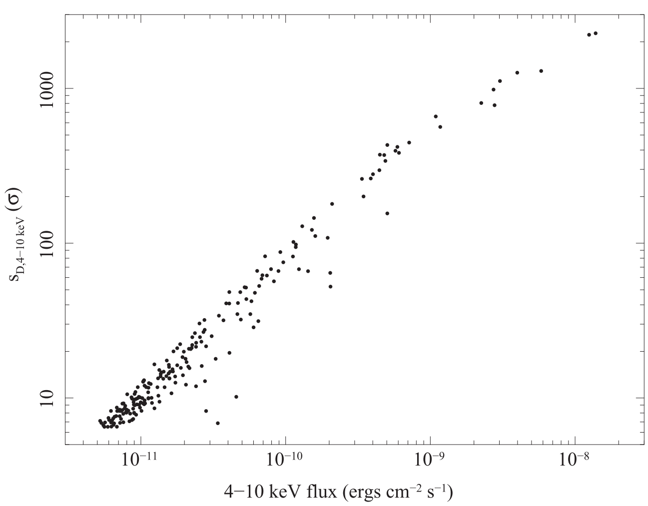

Figure 4. Correlation between the source flux and the detection significance for all the 7-year sources (in units of σ), in the 4–10 keV band.

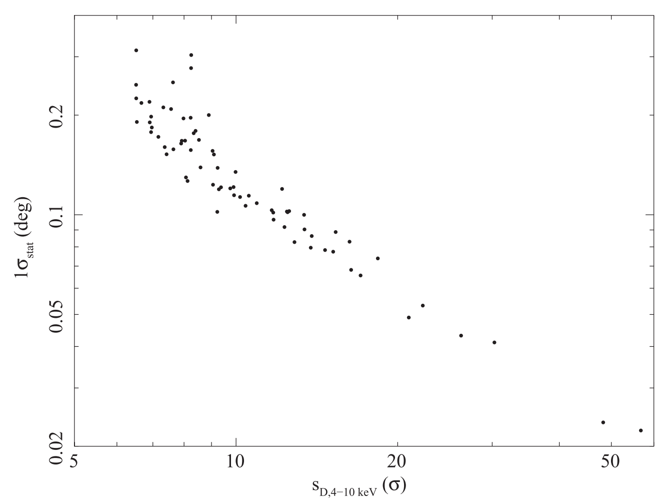

Figure 5. Correlation between the 4–10 keV detection significance and the 1σ positional error of the 71, 7-year sources without BAT105 counterparts.

3.5. Estimation of HR

We measured the 3–4 keV and 10–20 keV fluxes of the sources with a significance of $s_{D,4-10\,\mathrm{keV}} > 6.5$ via image fitting, to obtain their spectral information. The screened event data, simulated background, GRXE, and PSF data in the 3–4 keV and 10–20 keV bands were produced in the same way as those in the 4–10 keV band. The source positions were fixed at those determined in the analysis for the 4–10 keV data. HRs were defined by the fluxes in any two of the three bands:

$$\mathrm{HR\ (H,\ S)} = \frac{F_H - F_S}{F_H + F_S}, \tag{2}$$

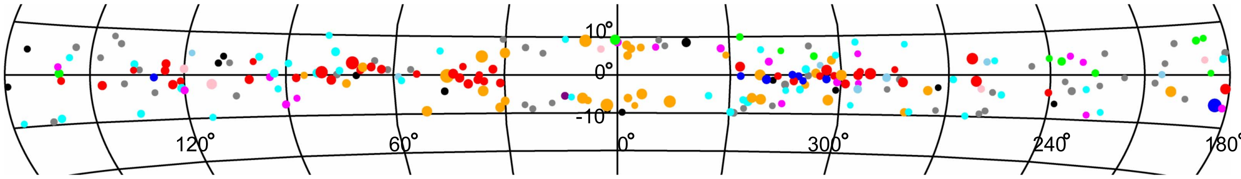

Figure 6. Location of the 7-year and 73-day sources in Galactic coordinates. The source fluxes on the logarithmic scale are indicated by the radii of the circles. The colors represent the object types: blazars and Seyfert galaxies (cyan), galaxy clusters (green), cataclysmic variables (magenta), stars (sky blue), pulsars (blue), supernova remnants (pink), high-mass, and low-mass X-ray binaries (red and orange, respectively), X-ray binaries (purple), sources whose types are unidentified in BAT105, 4U, XTEASMLONG, and XMMSL2 (black), and sources without any counterparts (gray).

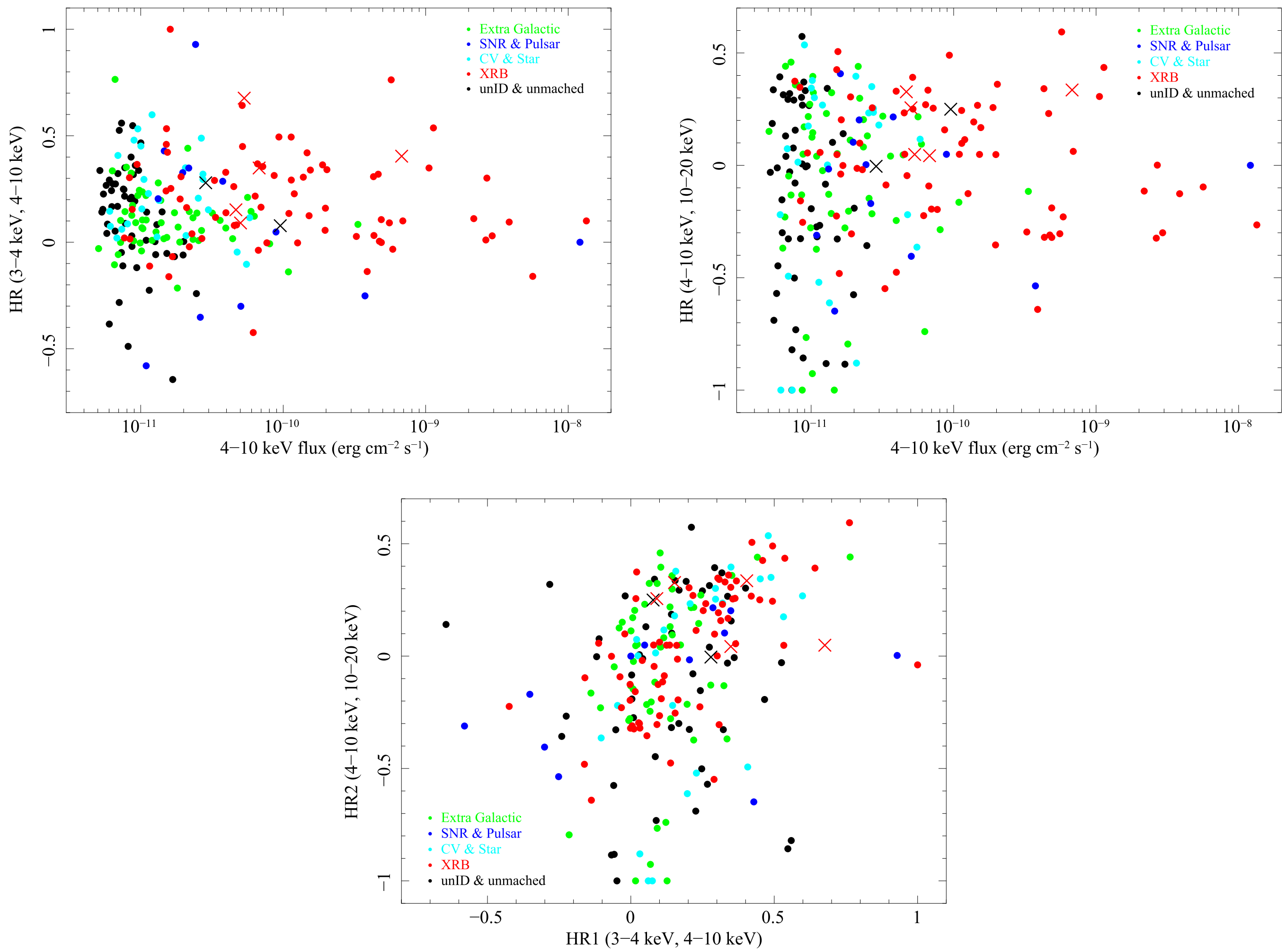

Figure 7. Scatter plots of HRs to the 4–10 keV flux (Upper panel). The colors represent the object types: blazars, galaxy clusters, and Seyfert galaxies (green), supernova remnants and pulsars (blue), cataclysmic variables and stars (sky-blue), X-ray binaries (red), and unidentified and unmatched sources (black). The 73-day sources are indicated by the cross marks.

where F_H and F_S correspond to the fluxes in the higher and lower energy bands, respectively. For the 73-day sources, we adopted the fluxes in one of the 73-day time bins when the 4–10 keV flux was the highest (the column (15) of Table 5). We defined HR1 as that between the 4–10 keV and 3–10 keV bands, and HR2 between the 10–20 keV and 4–10 keV bands.

4. Catalog

In this section, we present the catalog and discuss the statistical properties of the detected sources. In Table 4, we provide the 7-year MAXI/GSC catalog in the Galactic plane region $|b| < 10°$ (except for the Galactic center region $|b| < 5°$ and $|l| < 30°$), obtained from the GSC data in the 4–10 keV band. We detected 214 sources in total, with a significance of $s_{D,4\text{–}10\,\text{keV}} > 6.5$ in the 7-year integrated image, 143 of which are identified with sources listed in BAT105. Hereafter, these 214 sources are referred to as the "7-year sources." Seven sources are additionally detected in the 73-day time-sliced images ("73-day sources"; Table 5), one of which is identified with BAT105. The lowest source flux above $s_{D,4\text{–}10\,\text{keV}} = 6.5$ in the 7-year integrated image is 0.43 mCrab, which

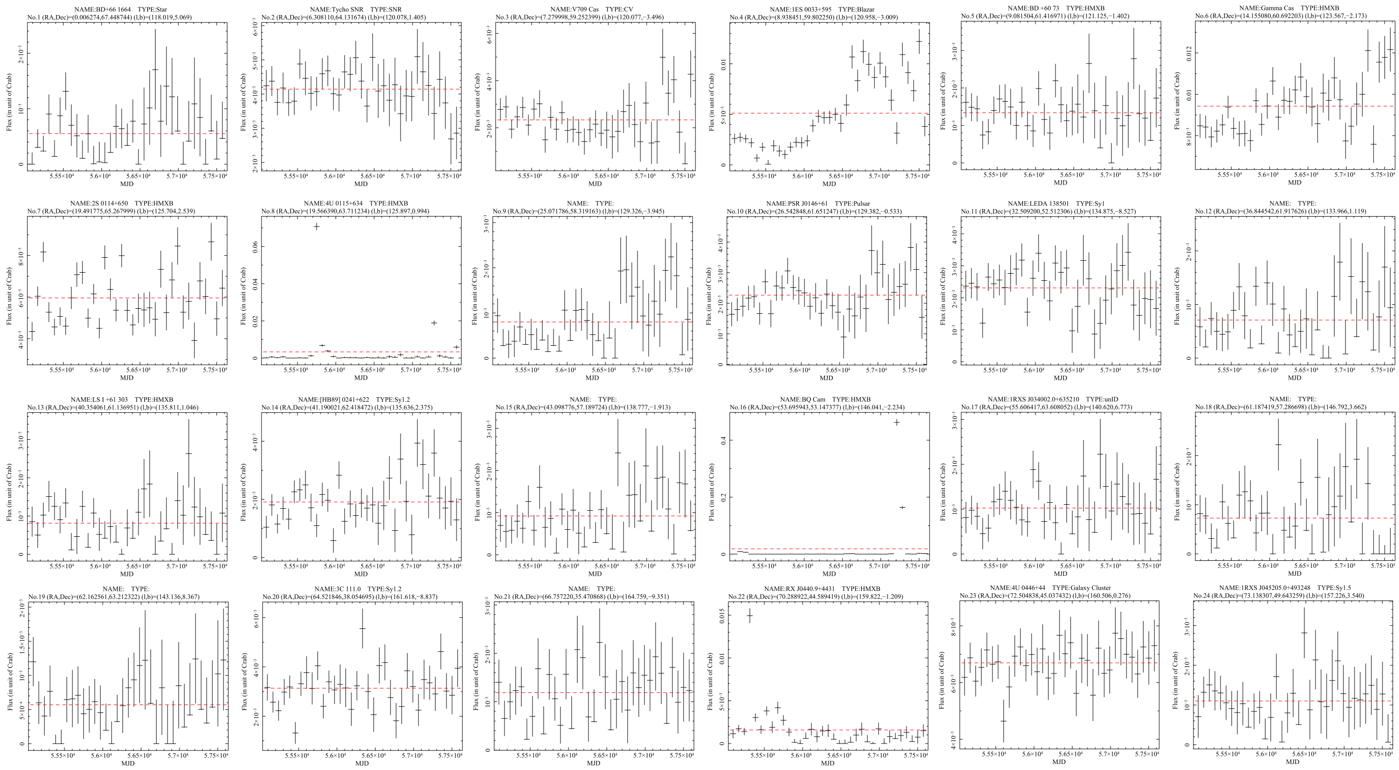

Figure 8. (a) 7-year light curves with 73-day bins. The mean flux of each source is plotted with a red dotted line. Flux margins are cut off at a flux of zero, sometimes resulting in small vertical error bars because the best-fit flux value is below zero. (b) 7-year light curves for 73-day sources with 73-day bins. The mean flux of each source is plotted with a red dotted line. Flux margins are cut off at a flux of zero, sometimes resulting in small vertical error bars because the best-fit flux value is below zero.

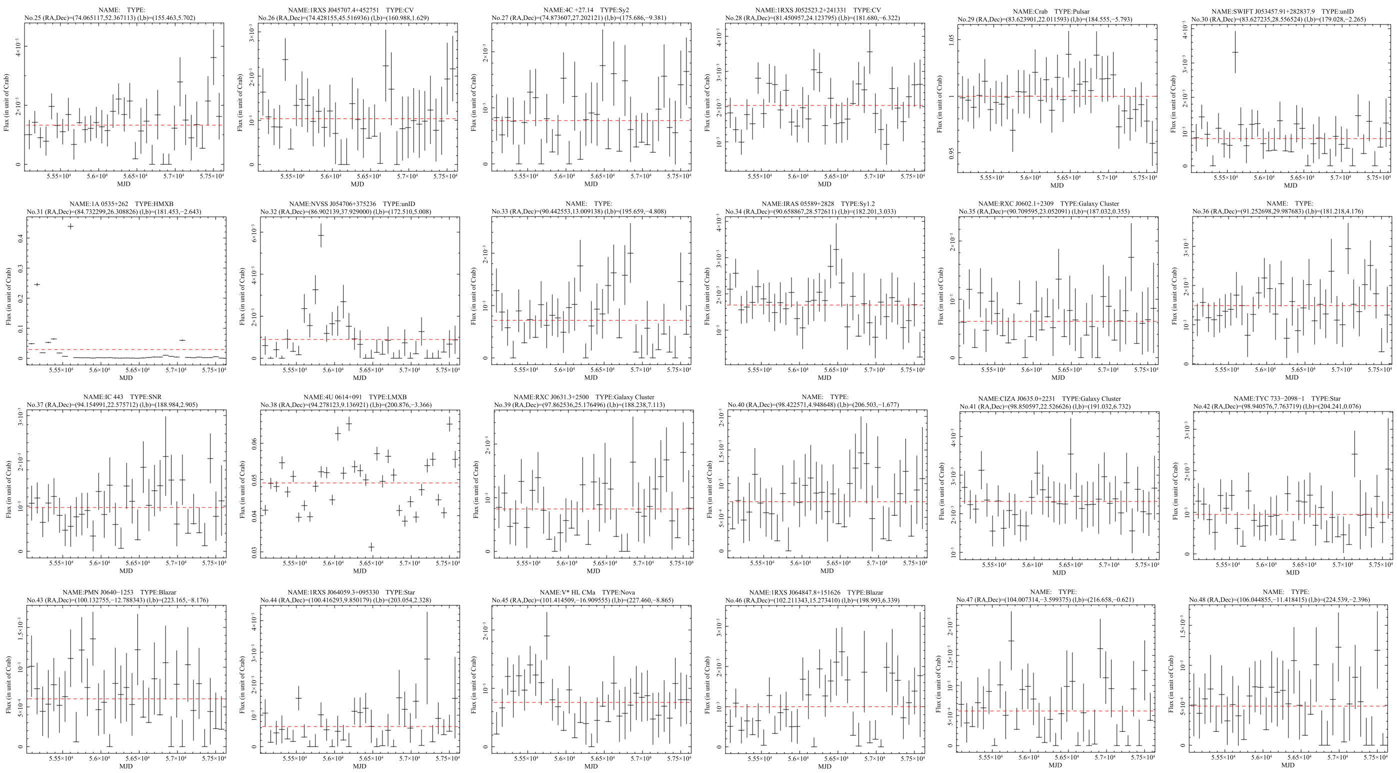

Figure 8. (Continued.)

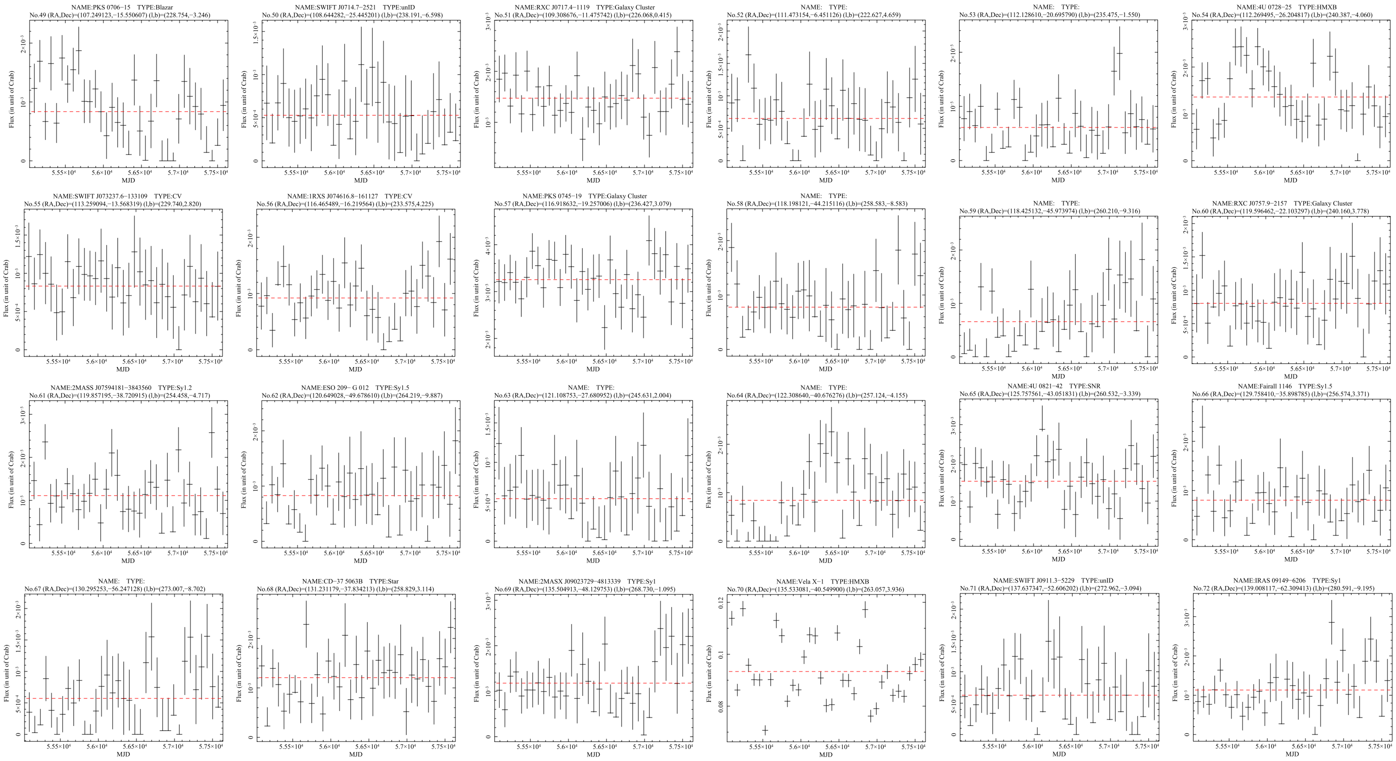

Figure 8. (Continued.)

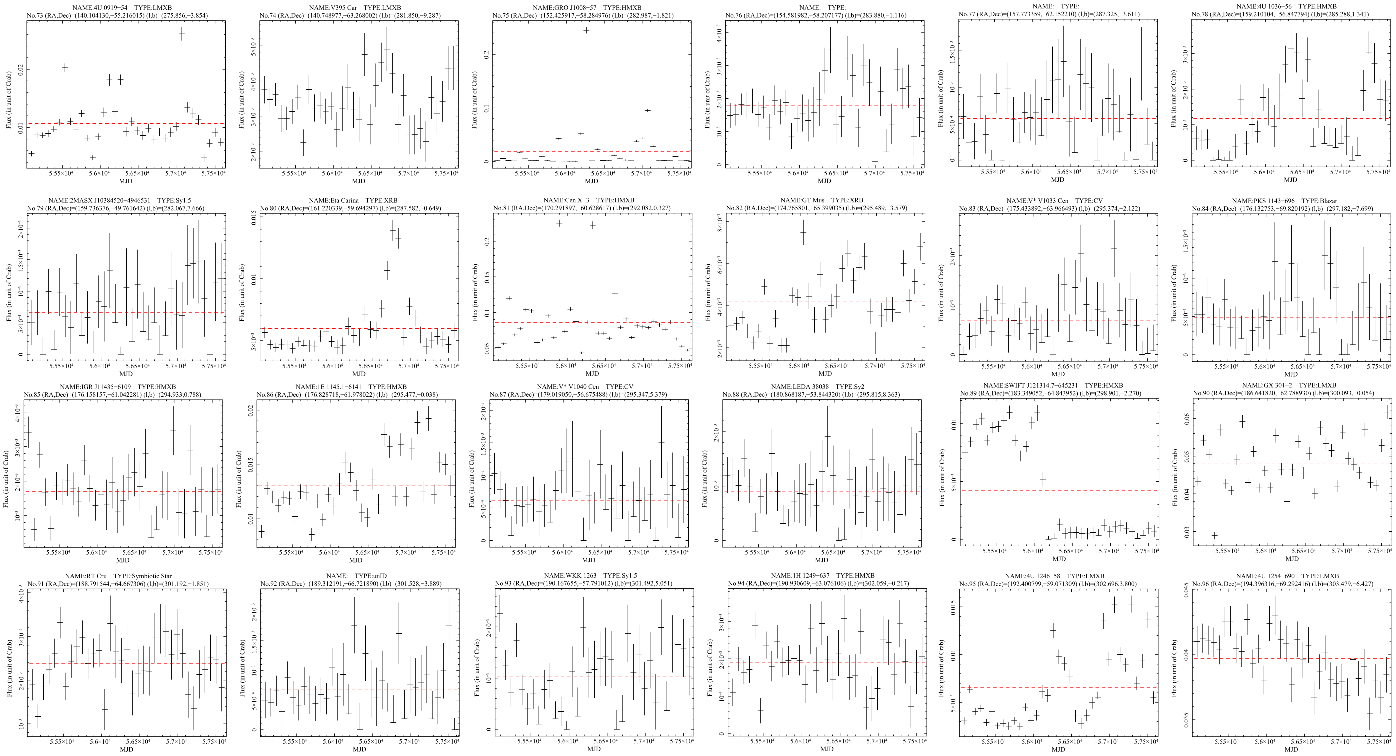

Figure 8. (Continued.)

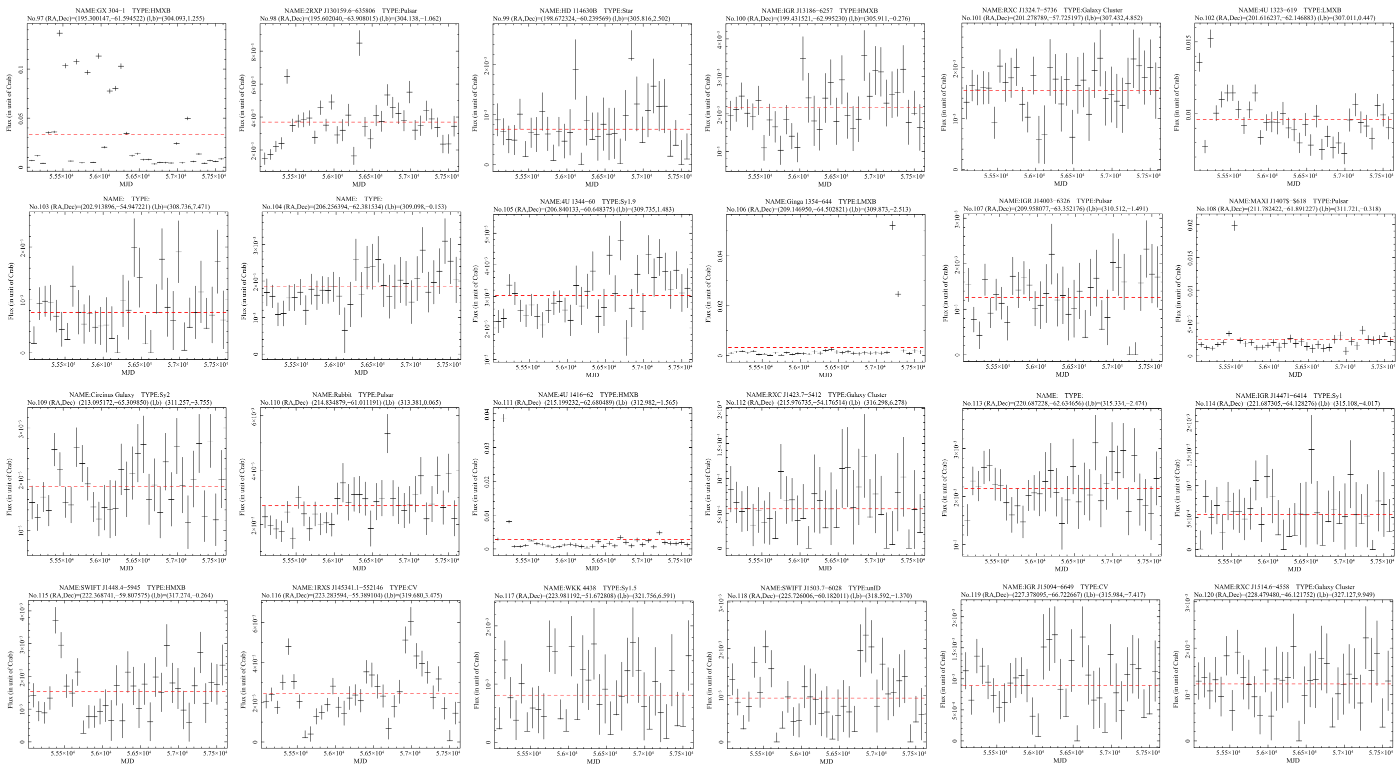

Figure 8. (Continued.)

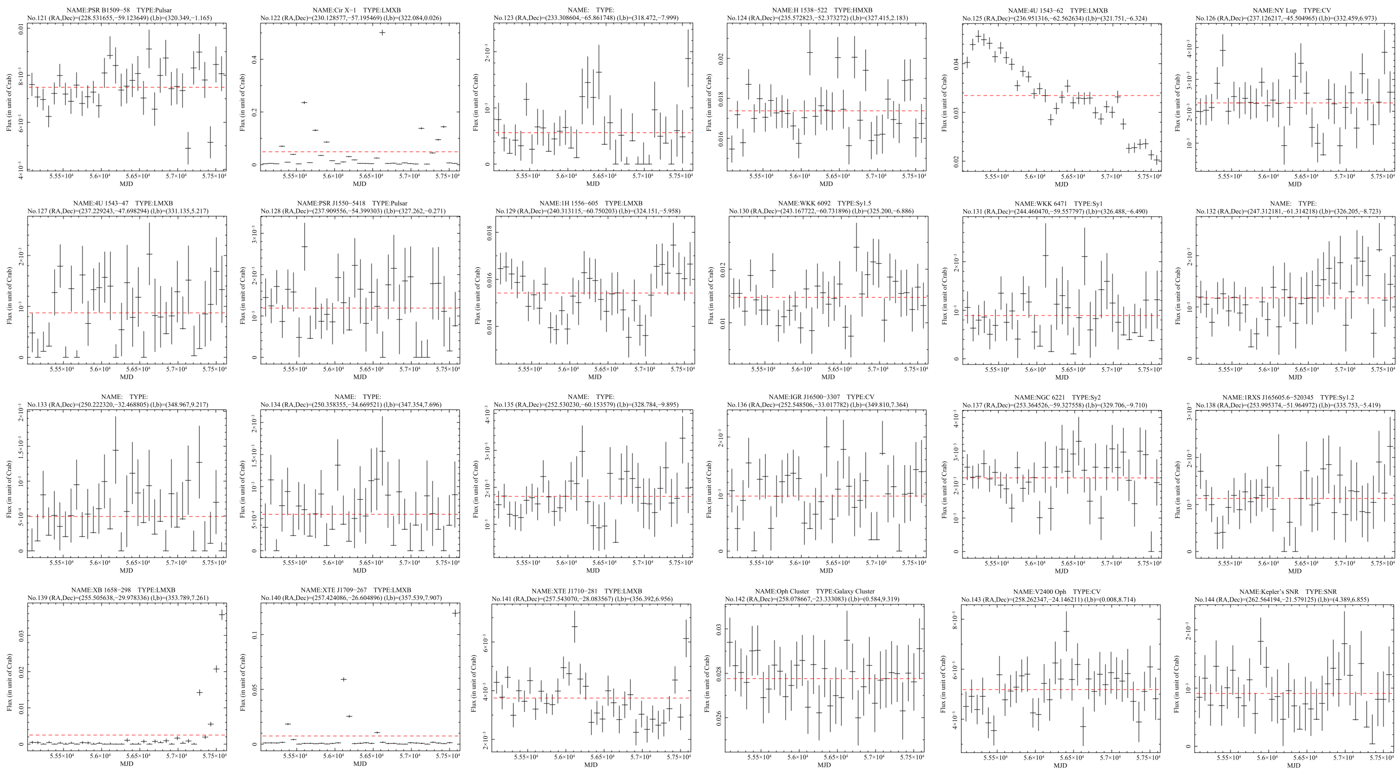

Figure 8. (Continued.)

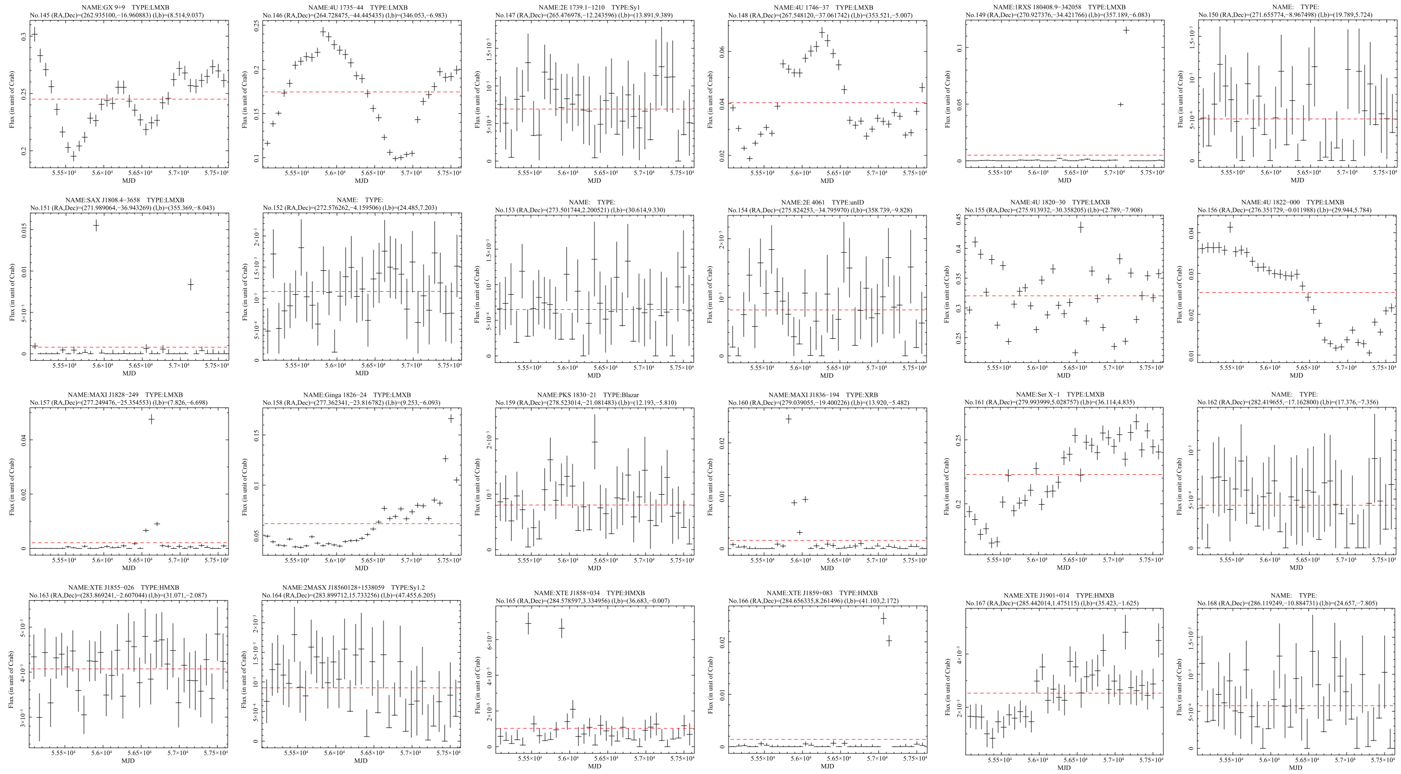

Figure 8. (Continued.)

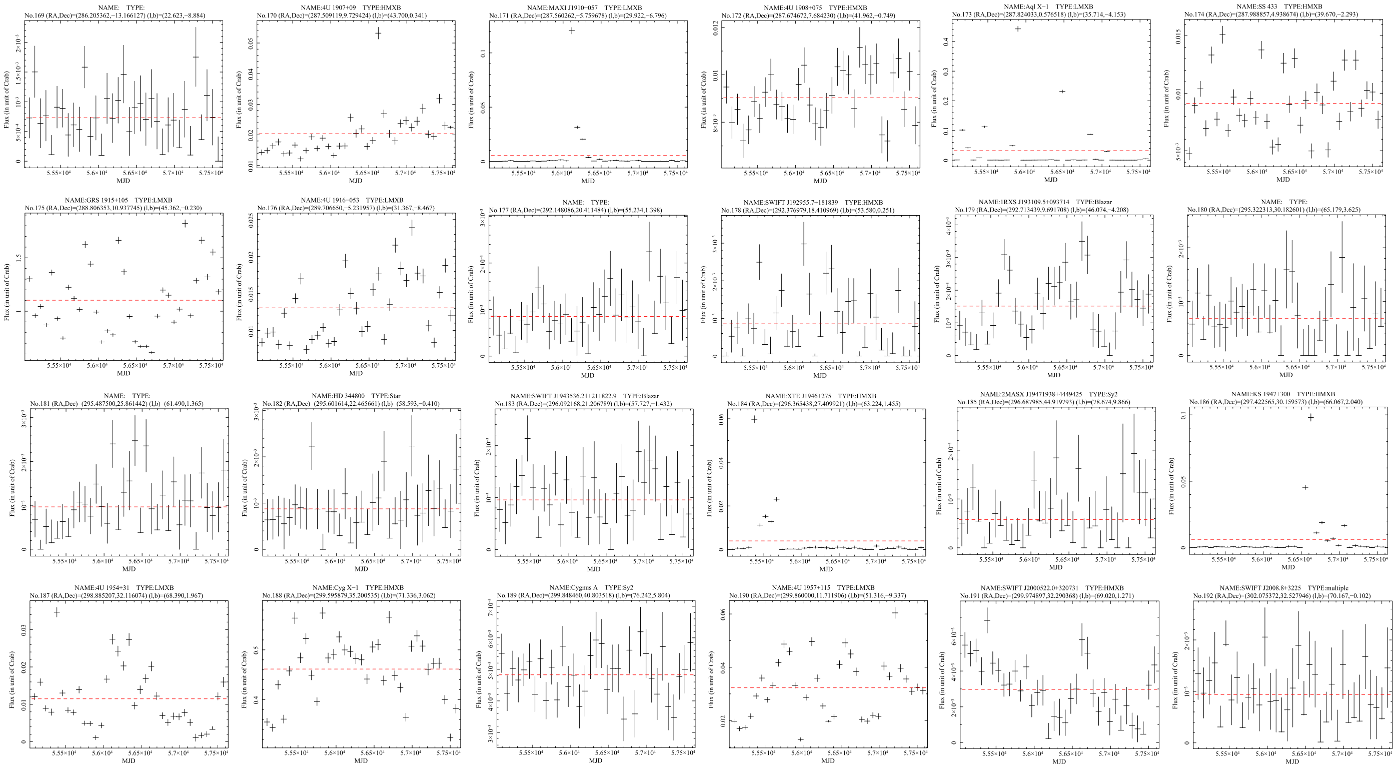

Figure 8. (Continued.)

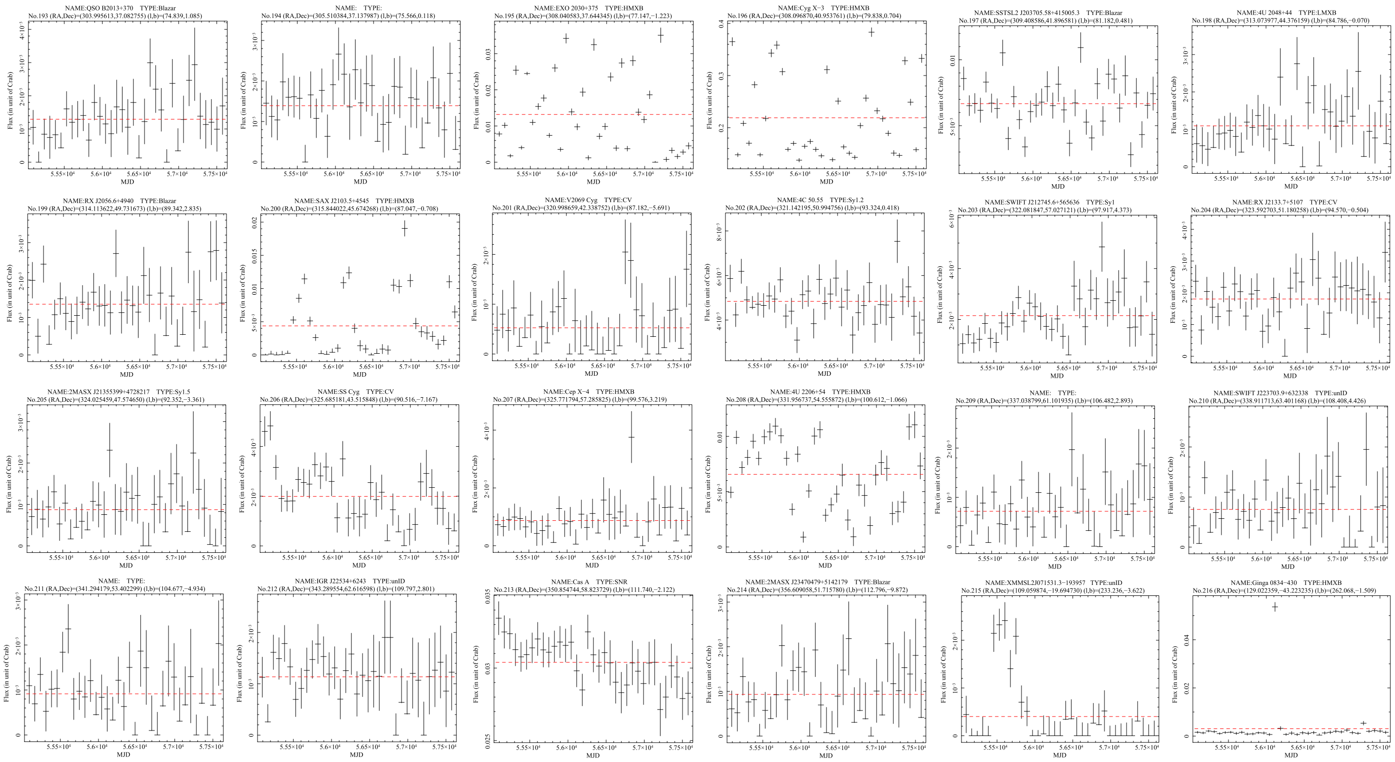

Figure 8. (Continued.)

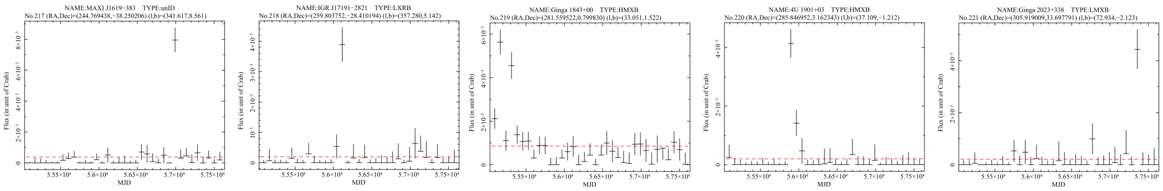

Figure 8. (Continued.)

corresponds to $5.2 \times 10^{-12}\,\mathrm{erg\,cm^{-2}\,s^{-1}}$ in the 4–10 keV band for a Crab-like spectrum. Note that the conversion factor from a flux in Crab units to a physical unit depends on the spectral shape. Table 1 summarizes those factors for various combinations of parameters of an absorbed power-law model. The corresponding values of HR1 and HR2 are listed in Table 2 (by definition HR1 = 0 and HR2 = 0 for a Crab-like spectrum).

Figure 4 shows the correlation between the 4–10 keV flux and the detection significance $s_{D,4-10\,\mathrm{keV}}$ for the 7-year sources. The observed trend can be understood by considering that the detection significance is approximately expressed as $s_{D,4-10\,\mathrm{keV}} \sim \mathrm{St}/\sqrt{\mathrm{St}+\mathrm{Bt}}$. At low fluxes, background events are dominant ($s_{D,4-10\,\mathrm{keV}} \sim S\sqrt{t/B}$), and hence we predict a linear correlation. By contrast, the source counts are dominant at high fluxes, $s_{D,4-10\,\mathrm{keV}}$ should be proportional to the square root of the source counts; $s_{D,4-10\,\mathrm{keV}} \sim \sqrt{\mathrm{St}}$. The data in Figure 4 indeed follow the trend. Note that our approximation of $s_{D,4-10\,\mathrm{keV}} \sim \mathrm{St}/\sqrt{\mathrm{St}+\mathrm{Bt}}$ does not represent the statistical significance of deviation from the background level in the source-photon-limited case. There are a few tens of sources that deviate from the trend and have relatively small detection significances, due to contamination by nearby bright sources.

4.1. Cross-matching with Other X-Ray Catalogs

For statistical studies of cataloged sources, it is important to find the counterparts and identify the object types of the detected sources. For this purpose, it is necessary to estimate the position accuracy of the detected sources. Figure 5 plots the detection significance in the 4–10 keV band and the 1σ positional errors of the 71, 7-year sources that are not listed in BAT105. They are roughly inversely proportional, as expected from statistics in determining the center of the PSF with limited source counts. The typical 1σ error at $s_{D,4-10\,\mathrm{keV}} \sim 7$ is $\sim 0\overset{\circ}{.}2$.

As a next step, we attempted to identify the sources without BAT105 counterparts, using other catalogs. The positional error σ_{posi} is defined as $\sigma_{\mathrm{posi}} \equiv \sqrt{\sigma_{\mathrm{stat}}^2 + \sigma_{\mathrm{sys}}^2}$, where σ_{stat} and σ_{sys} are the statistical and systematic errors, respectively. We adopted $\sigma_{\mathrm{sys}} = 0\overset{\circ}{.}05$, which is a typical systematic uncertainty associated with GSC alignment calibration (Hiroi et al. 2011). We searched for sources in the reference catalogs located within a $2.5\sigma_{\mathrm{posi}}$ error circle, which corresponds to the 95% confidence level. We utilized the data when the highest 4–10 keV flux was obtained among the individual 73-day bin images to estimate σ_{stat} for the 73-day sources (Table 5).

Because of the large positional errors, it is difficult to find the counterparts in optical or infrared catalogs, which have a much higher number density of sources with a much better position accuracy. We therefore performed cross-matching with major X-ray catalogs. We first matched the *Uhuru* fourth catalog (Forman et al. 1978, hereafter 4U) and found the counterparts of four sources. Then, we searched the *RXTE* All-Sky Monitor (ASM) long-term observed source table (hereafter XTEASMLONG), which is based on ASM light curve data products[20] for the remaining sources that have no counterparts in BAT105 and 4U. Finally, we carried out cross-matching with the *XMM-Newton* slew survey catalog (hereafter XMMSL2; Saxton et al. 2008), the Meta-Catalog of X-ray Detected Cluster of Galaxies (hereafter MCXC; Piffaretti et al. 2011), and the *ROSAT* all-sky survey bright source catalog (hereafter 1RXS; Voges et al. 1999). For XMMSL2 and 1RXS, we only referred to the sources with fluxes of $>1.0 \times 10^{-12}$ erg cm^{-2} s^{-1} and >0.30 cts s^{-1}, respectively, both corresponding to 0.3 mCrab for the Crab spectrum. Finally, as for the sources with BAT105 counterparts that are optically unidentified ("unidentified") and those without BAT105 counterparts that are not matched with any objects in the above 5 X-ray catalogs ("unmatched"), we also checked the MAXI transient source catalog summarized by Negoro et al. (2016).

As a result, 36 out of the 77 sources were matched with at least 1 counterpart. Tables 3(a) and (b) show the number of MAXI sources that were matched with the reference catalogs for the 7-year and 73-day sources, respectively. Tables 6 and 7 list the counterparts for 7-year and 73-day sources, respectively. If multiple sources were found within the error circles, we adopted the closest object to the position in our catalog as the most likely counterpart. For BAT105 sources, we did not attempt to find counterparts in other catalogs, because their positional errors were not estimated. The typical positional errors of the 4U, XMMSL2, and 1RXS counterparts are $0\overset{\circ}{.}5$, $3''$, and $10''$ respectively. The expected numbers of erroneous identification by chance are estimated to be 0.88, 1.48, 1.78, 0.31, and 2.45 for 4U, XTEASMLONG, XMMSL2, MCXC, and 1RXS, respectively, based on the mean number densities of the cross-matched sources in our survey region and the total area of the error circles (2.5σ) of the MAXI sources without BAT105 counterparts. Figure 6 plots the location of the MAXI sources in Galactic coordinates. Table 8 (second column) lists the number of each source type. The fluxes of the MAXI sources were found to be consistent with those of their counterparts in 4U, XTEASMLONG, XMMSL2, MCXC, and 1RXS catalogs within a factor of 4. In Figure 7, we present the correlation between the 4–10 keV flux and the HR (HR1 or HR2), and that between HR1 and HR2, for different object types.

4.2. Time Variabilities

Long-term variability is essential information for understanding the nature of the detected objects. Figures 8(a) and (b) show the light curves for all objects. We added a systematic error of 1.6% in each flux due to incomplete instrumental

[20] https://heasarc.gsfc.nasa.gov/W3Browse/xte/xteasmlong.html

Table 4
Properties of the 7-year Sources in the MAXI/GSC Catalog at $|b| < 10°$

(1) No.	(2) 3MAXI	(3) R.A.	(4) Decl.	(5) σ_{stat} [a]	(6) $s_{D,4-10\,keV}$	(7) $f_{4-10keV}$ [b]	(8) $s_{D,3-4\,keV}$	(9) $f_{3-4\,keV}$ [c]	(10) $s_{D,10-20\,keV}$	(11) $f_{10-20keV}$ [d]	(12) HR1 [e]	(13) HR2 [f]	(14) σ^2_{rms} [g]
1	J0000+674	0.006	67.449	0.173	7.2	6.3 ± 0.9	6.5	1.7 ± 0.3	0.0	<1.7	0.08 ± 0.13	−1.0 ± 0.2	0.14 ± 0.13
2	J0025+641	6.308	64.132	⋯	51.9	52.1 ± 1.0	80.4	30.9 ± 0.4	4.3	15 ± 4	−0.30 ± 0.01	−0.40 ± 0.09	−0.005 ± 0.005
3	J0029+592	7.280	59.252	⋯	8.2	28 ± 3	11.6	4.6 ± 0.4	6.8	31 ± 5	0.32 ± 0.11	0.24 ± 0.13	0.05 ± 0.02
4	J0035+598	8.938	59.802	⋯	10.2	46 ± 4	32.3	14.1 ± 0.4	7.3	34 ± 5	0.02 ± 0.06	0.05 ± 0.10	0.441 ± 0.007
5	J0036+614	9.082	61.417	⋯	14.4	15.6 ± 1.1	9.3	3.0 ± 0.3	1.7	6.7 ± 3.9	0.24 ± 0.07	−0.2 ± 0.3	−0.00 ± 0.04
6	J0056+606	14.155	60.692	⋯	101.9	113.3 ± 1.1	72.0	27.5 ± 0.4	22.9	85 ± 4	0.14 ± 0.01	0.05 ± 0.03	0.011 ± 0.002
7	J0117+652	19.492	65.268	⋯	61.8	74.3 ± 1.2	34.0	11.2 ± 0.3	23.1	85 ± 4	0.36 ± 0.02	0.25 ± 0.03	0.031 ± 0.003
8	J0118+637	19.566	63.711	⋯	43.5	53.5 ± 1.2	19.6	6.5 ± 0.3	16.1	61 ± 4	0.45 ± 0.03	0.25 ± 0.05	13.081 ± 0.006
9	J0140+583	25.072	58.319	0.121	8.1	8.0 ± 1.0	4.1	1.2 ± 0.3	2.0	7.5 ± 3.8	0.35 ± 0.14	0.2 ± 0.4	0.23 ± 0.09
10	J0146+616	26.543	61.651	⋯	26.7	27.1 ± 1.0	50.0	18.0 ± 0.4	3.5	13 ± 4	−0.35 ± 0.02	−0.17 ± 0.15	0.01 ± 0.02
11	J0210+525	32.509	52.512	⋯	11.9	24 ± 2	20.5	7.5 ± 0.4	5.6	25 ± 4	0.01 ± 0.06	0.20 ± 0.14	0.00 ± 0.02
12	J0227+619	36.845	61.918	0.153	8.1	7.9 ± 1.0	5.1	1.5 ± 0.3	0.0	<5.5	0.25 ± 0.13	−0.50 ± 0.12	0.15 ± 0.09
13	J0241+611	40.354	61.137	⋯	7.2	8.7 ± 1.2	8.1	2.7 ± 0.3	1.1	4.3 ± 4.0	0.02 ± 0.11	−0.2 ± 0.5	0.20 ± 0.08
14	J0244+624	41.190	62.418	⋯	22.0	22.6 ± 1.0	16.6	5.4 ± 0.3	7.4	28 ± 4	0.14 ± 0.04	0.30 ± 0.11	0.07 ± 0.02
15	J0252+571	43.099	57.190	0.094	8.5	8.8 ± 1.0	3.8	1.2 ± 0.3	2.8	11.2 ± 4.0	0.40 ± 0.14	0.3 ± 0.3	0.15 ± 0.07
16	J0334+531	53.696	53.147	⋯	75.3	96.4 ± 1.3	28.0	10.4 ± 0.4	42.3	192 ± 4	0.49 ± 0.02	0.49 ± 0.02	18.699 ± 0.008
17	J0342+636	55.606	63.608	0.099	12.5	11.4 ± 0.9	9.7	2.7 ± 0.3	1.2	4.0 ± 3.5	0.14 ± 0.08	−0.3 ± 0.4	−0.04 ± 0.06
18	J0404+572	61.187	57.287	0.203	6.5	6.8 ± 1.0	6.4	2.0 ± 0.3	1.5	6.1 ± 3.9	0.05 ± 0.13	0.1 ± 0.5	0.29 ± 0.09
19	J0408+632	62.163	63.212	0.219	6.5	5.9 ± 0.9	3.9	1.1 ± 0.3	0.0	<4.6	0.27 ± 0.17	−0.57 ± 0.16	−0.07 ± 0.12
20	J0418+380	64.522	38.055	⋯	31.8	37.2 ± 1.2	27.4	9.7 ± 0.4	6.6	28 ± 4	0.10 ± 0.03	0.04 ± 0.10	0.02 ± 0.01
21	J0427+354	66.757	35.471	0.102	11.7	13.0 ± 1.1	12.6	4.1 ± 0.3	1.8	7.5 ± 4.1	0.00 ± 0.07	−0.1 ± 0.3	−0.01 ± 0.05
22	J0441+445	70.289	44.589	⋯	15.6	21.7 ± 1.4	13.6	5.0 ± 0.4	3.2	14 ± 4	0.16 ± 0.06	−0.0 ± 0.2	2.41 ± 0.03
23	J0450+450	72.505	45.037	0.022	56.8	83.0 ± 1.5	58.9	26.8 ± 0.5	6.5	31 ± 5	−0.01 ± 0.01	−0.29 ± 0.07	−0.005 ± 0.003
24	J0452+496	73.138	49.643	⋯	9.2	10.7 ± 1.2	8.8	3.0 ± 0.3	3.2	14 ± 4	0.06 ± 0.10	0.3 ± 0.3	−0.03 ± 0.07
25	J0456+523	74.065	52.367	0.090	13.4	15.7 ± 1.2	15.9	5.6 ± 0.4	1.3	5.4 ± 4.3	−0.05 ± 0.06	−0.3 ± 0.3	0.12 ± 0.05
26	J0457+455	74.428	45.517	⋯	9.5	13.4 ± 1.4	10.9	4.1 ± 0.4	1.9	9.2 ± 4.7	0.03 ± 0.09	0.0 ± 0.3	0.01 ± 0.07
27	J0459+272	74.874	27.202	⋯	8.3	8.2 ± 1.0	4.4	1.2 ± 0.3	3.1	12 ± 4	0.35 ± 0.14	0.4 ± 0.3	0.15 ± 0.07
28	J0525+241	81.451	24.124	⋯	20.8	21.5 ± 1.0	20.4	6.4 ± 0.3	0.0	<4.6	0.03 ± 0.04	−0.88 ± 0.06	0.02 ± 0.02
29	J0534+220	83.624	22.012	⋯	2222.4	12494 ± 6	1507.1	3980 ± 3	997.7	8510 ± 8	0.00 ± 0.00	0.00 ± 0.00	−0.000 ± 0.000
30	J0534+285	83.627	28.557	⋯	9.0	9.1 ± 1.0	2.9	0.8 ± 0.3	0.0	<4.4	0.55 ± 0.15	−0.86 ± 0.14	0.34 ± 0.06
31	J0538+263	84.732	26.309	⋯	296.3	444.3 ± 1.5	153.3	74.9 ± 0.5	141.9	616 ± 4	0.31 ± 0.00	0.34 ± 0.01	8.004 ± 0.005
32	J0547+379	86.902	37.929	⋯	8.0	9.0 ± 1.1	9.1	3.0 ± 0.3	2.5	10.6 ± 4.2	−0.02 ± 0.10	0.3 ± 0.3	1.51 ± 0.06
33	J0601+130	90.443	13.009	0.156	7.9	7.6 ± 1.0	9.9	2.7 ± 0.3	0.0	<2.7	−0.05 ± 0.10	−1.00 ± 0.18	0.30 ± 0.06
34	J0602+285	90.659	28.573	⋯	24.7	25.6 ± 1.0	18.5	6.2 ± 0.3	5.8	23 ± 4	0.14 ± 0.04	0.13 ± 0.12	0.00 ± 0.03
35	J0602+230	90.710	23.052	0.166	6.9	7.2 ± 1.0	9.3	2.6 ± 0.3	1.2	4.4 ± 3.7	−0.06 ± 0.11	−0.1 ± 0.5	−0.05 ± 0.10
36	J0605+299	91.253	29.988	0.076	16.3	17.8 ± 1.1	19.4	6.5 ± 0.3	0.0	<5.0	−0.07 ± 0.05	−0.88 ± 0.08	−0.01 ± 0.03
37	J0616+225	94.155	22.576	0.100	11.7	11.3 ± 1.0	42.4	13.5 ± 0.3	1.1	4.0 ± 3.6	−0.58 ± 0.03	−0.3 ± 0.4	0.05 ± 0.05
38	J0617+091	94.278	9.137	⋯	383.5	606.6 ± 1.6	306.4	206.4 ± 0.7	73.0	259 ± 4	−0.03 ± 0.00	−0.23 ± 0.01	0.023 ± 0.001
39	J0631+251	97.863	25.176	0.128	9.1	8.9 ± 1.0	7.9	2.2 ± 0.3	0.0	<2.3	0.13 ± 0.10	−1.00 ± 0.16	0.08 ± 0.08
40	J0633+049	98.423	4.949	0.112	9.8	8.9 ± 0.9	10.3	2.7 ± 0.3	1.9	6.2 ± 3.3	0.03 ± 0.09	0.0 ± 0.3	−0.04 ± 0.07
41	J0635+225	98.851	22.527	⋯	27.6	27.6 ± 1.0	26.3	7.9 ± 0.3	3.3	12 ± 4	0.06 ± 0.03	−0.22 ± 0.15	−0.02 ± 0.01
42	J0635+077	98.941	7.764	0.091	12.3	11.7 ± 1.0	8.8	2.3 ± 0.3	0.0	<5.9	0.23 ± 0.08	−0.52 ± 0.08	0.03 ± 0.06
43	J0640−127	100.133	−12.788	⋯	9.2	7.5 ± 0.8	10.6	2.4 ± 0.2	1.3	3.9 ± 3.1	−0.00 ± 0.09	−0.1 ± 0.4	0.07 ± 0.07
44	J0641+098	100.416	9.850	0.054	6.5	6.3 ± 1.0	5.5	1.5 ± 0.3	0.0	<6.3	0.15 ± 0.14	−0.22 ± 0.12	0.39 ± 0.14
45	J0645−169	101.415	−16.910	⋯	7.1	8.3 ± 1.2	10.0	2.2 ± 0.2	1.9	5.8 ± 3.0	0.09 ± 0.11	0.0 ± 0.3	0.02 ± 0.06
46	J0648+152	102.211	15.273	0.108	10.0	10.2 ± 1.0	11.4	3.3 ± 0.3	1.0	3.9 ± 3.8	−0.00 ± 0.08	−0.3 ± 0.4	0.19 ± 0.07
47	J0656−035	104.007	−3.599	0.159	6.9	6.2 ± 0.9	4.4	1.1 ± 0.2	3.1	10 ± 3	0.29 ± 0.15	0.4 ± 0.3	0.35 ± 0.08

Table 4
(Continued)

(1) No.	(2) 3MAXI	(3) R.A.	(4) Decl.	(5) $\sigma_{\rm stat}$[a]	(6) $s_{D,4-10\,{\rm keV}}$	(7) $f_{4-10{\rm keV}}$[b]	(8) $s_{D,3-4\,{\rm keV}}$	(9) $f_{3-4\,{\rm keV}}$[c]	(10) $s_{D,10-20\,{\rm keV}}$	(11) $f_{10-20{\rm keV}}$[d]	(12) HR1[e]	(13) HR2[f]	(14) $\sigma^2_{\rm rms}$[g]
48	J0704−114	106.045	−11.418	0.162	6.9	5.7 ± 0.8	5.0	1.1 ± 0.2	0.0	<3.8	0.23 ± 0.14	−0.69 ± 0.16	0.02 ± 0.11
49	J0708−155	107.249	−15.551	…	12.9	10.5 ± 0.8	15.7	3.6 ± 0.2	3.0	9 ± 3	−0.04 ± 0.06	0.1 ± 0.2	0.28 ± 0.04
50	J0714−254	108.644	−25.445	…	7.2	6.0 ± 0.8	7.1	1.6 ± 0.2	0.0	<4.8	0.09 ± 0.12	−0.45 ± 0.13	−0.12 ± 0.10
51	J0717−114	109.309	−11.476	0.053	21.0	17.8 ± 0.8	17.9	4.3 ± 0.2	0.0	<9.9	0.14 ± 0.04	−0.28 ± 0.04	−0.01 ± 0.02
52	J0725−064	111.473	−6.451	0.155	8.2	7.1 ± 0.9	6.7	1.6 ± 0.2	2.8	8.9 ± 3.1	0.17 ± 0.12	0.3 ± 0.3	0.04 ± 0.08
53	J0728−206	112.129	−20.696	0.150	7.4	6.0 ± 0.8	7.9	1.8 ± 0.2	1.3	4.0 ± 3.1	0.04 ± 0.11	−0.0 ± 0.5	0.21 ± 0.07
54	J0729−262	112.269	−26.205	…	20.0	16.8 ± 0.8	13.6	3.2 ± 0.2	5.5	17 ± 3	0.25 ± 0.05	0.20 ± 0.14	0.11 ± 0.02
55	J0733−135	113.259	−13.568	…	12.7	10.4 ± 0.8	5.6	1.2 ± 0.2	4.7	14 ± 3	0.45 ± 0.10	0.34 ± 0.18	−0.12 ± 0.05
56	J0745−162	116.465	−16.220	…	13.0	10.5 ± 0.8	10.9	2.4 ± 0.2	5.2	16 ± 3	0.16 ± 0.07	0.38 ± 0.17	0.06 ± 0.04
57	J0747−192	116.919	−19.257	…	48.3	40.9 ± 0.8	45.1	11.4 ± 0.3	5.6	17 ± 3	0.07 ± 0.02	−0.25 ± 0.08	−0.003 ± 0.005
58	J0752−442	118.198	−44.215	0.150	7.9	8.4 ± 1.1	6.8	8 ± 1	2.4	36.7 ± 15.1	−0.49 ± 0.15	0.7 ± 0.5	0.07 ± 0.08
59	J0753−459	118.425	−45.974	0.170	7.0	7.6 ± 1.1	2.3	0.7 ± 0.3	0.0	<4.6	0.56 ± 0.19	−0.82 ± 0.18	0.33 ± 0.08
60	J0758−221	119.596	−22.103	0.097	11.7	9.5 ± 0.8	11.2	2.5 ± 0.2	0.0	<3.9	0.09 ± 0.08	−0.77 ± 0.10	−0.03 ± 0.05
61	J0759−387	119.857	−38.721	…	14.3	13.7 ± 1.0	9.3	2.5 ± 0.3	2.0	7.2 ± 3.5	0.28 ± 0.07	−0.1 ± 0.3	0.09 ± 0.04
62	J0802−496	120.649	−49.679	…	10.1	9.9 ± 1.0	7.2	2.0 ± 0.3	2.9	10.4 ± 3.6	0.22 ± 0.10	0.2 ± 0.3	−0.00 ± 0.07
63	J0804−276	121.109	−27.681	0.138	8.2	6.9 ± 0.8	5.5	1.2 ± 0.2	1.6	5.1 ± 3.1	0.27 ± 0.13	0.0 ± 0.4	0.01 ± 0.10
64	J0809−406	122.309	−40.676	0.143	8.0	8.0 ± 1.0	5.9	1.6 ± 0.3	1.3	4.6 ± 3.7	0.22 ± 0.12	−0.1 ± 0.5	0.32 ± 0.07
65	J0823−430	125.758	−43.052	0.070	15.3	16.6 ± 1.1	66.9	93 ± 1	1.9	26.8 ± 13.8	−0.89 ± 0.02	0.4 ± 0.5	0.02 ± 0.03
66	J0839−358	129.758	−35.899	…	8.4	8.0 ± 1.0	7.6	1.9 ± 0.3	3.4	12 ± 3	0.14 ± 0.11	0.4 ± 0.3	0.10 ± 0.06
67	J0841−562	130.295	−56.247	0.203	6.7	5.5 ± 0.8	5.4	1.3 ± 0.2	1.7	5.5 ± 3.1	0.14 ± 0.14	0.2 ± 0.4	0.27 ± 0.10
68	J0844−378	131.231	−37.834	0.078	14.6	13.9 ± 0.9	11.3	3.0 ± 0.3	0.0	<5.8	0.20 ± 0.07	−0.61 ± 0.07	−0.00 ± 0.04
69	J0902−481	135.505	−48.130	…	13.3	14.3 ± 1.1	9.9	3.1 ± 0.3	1.6	6.3 ± 4.0	0.20 ± 0.07	−0.2 ± 0.3	0.05 ± 0.04
70	J0902−405	135.533	−40.550	…	564.2	1170 ± 2	204.0	112.3 ± 0.6	371.2	2027 ± 6	0.54 ± 0.00	0.44 ± 0.00	0.015 ± 0.001
71	J0910−526	137.637	−52.606	…	6.7	6.5 ± 1.0	5.6	1.5 ± 0.3	0.0	<5.8	0.17 ± 0.14	−0.30 ± 0.12	0.07 ± 0.09
72	J0916−623	139.008	−62.309	…	10.3	13.2 ± 1.3	14.0	3.8 ± 0.3	4.6	14 ± 3	0.05 ± 0.07	0.23 ± 0.17	0.12 ± 0.03
73	J0920−552	140.104	−55.216	…	128.7	130.3 ± 1.0	116.0	41.7 ± 0.4	21.0	69 ± 3	−0.00 ± 0.01	−0.13 ± 0.03	0.156 ± 0.001
74	J0922−632	140.749	−63.268	…	19.6	41 ± 2	35.0	9.9 ± 0.3	3.2	10 ± 3	0.14 ± 0.04	−0.48 ± 0.12	0.013 ± 0.006
75	J1009−582	152.426	−58.285	…	108.4	195.2 ± 1.8	80.4	29.0 ± 0.4	61.7	225 ± 4	0.36 ± 0.01	0.26 ± 0.01	5.229 ± 0.004
76	J1018−582	154.582	−58.207	0.080	12.2	20.5 ± 1.7	21.6	7.4 ± 0.3	1.0	3.8 ± 3.7	−0.06 ± 0.06	−0.6 ± 0.3	0.09 ± 0.02
77	J1031−621	157.773	−62.152	0.132	6.9	5.3 ± 0.8	3.5	0.8 ± 0.2	1.2	3.4 ± 2.8	0.34 ± 0.17	−0.0 ± 0.5	0.17 ± 0.08
78	J1036−568	159.210	−56.848	…	10.1	8.6 ± 0.9	5.6	1.5 ± 0.3	3.9	12 ± 3	0.30 ± 0.11	0.3 ± 0.2	0.59 ± 0.03
79	J1038−497	159.736	−49.762	…	6.9	6.5 ± 1.0	3.8	1.0 ± 0.3	0.0	<5.6	0.34 ± 0.16	−0.37 ± 0.12	0.09 ± 0.09
80	J1044−596	161.220	−59.694	…	34.8	57.1 ± 1.6	64.3	22.4 ± 0.3	5.2	18 ± 4	−0.10 ± 0.02	−0.36 ± 0.08	0.131 ± 0.003
81	J1121−606	170.292	−60.629	…	658.8	1090.2 ± 1.7	300.6	167.8 ± 0.6	337.5	1398 ± 4	0.35 ± 0.00	0.31 ± 0.00	0.205 ± 0.001
82	J1139−653	174.766	−65.399	…	32.1	49.0 ± 1.5	58.3	17.1 ± 0.3	7.3	21 ± 3	−0.05 ± 0.02	−0.22 ± 0.07	0.101 ± 0.004
83	J1141−639	175.434	−63.966	0.155	8.4	7.1 ± 0.8	3.3	1.0 ± 0.3	0.0	<4.8	0.41 ± 0.15	−0.49 ± 0.11	0.25 ± 0.07
84	J1144−698	176.133	−69.820	…	7.1	5.2 ± 0.7	7.8	1.8 ± 0.2	1.9	4.8 ± 2.6	−0.03 ± 0.12	0.1 ± 0.4	0.17 ± 0.09
85	J1144−610	176.158	−61.042	…	14.0	19.5 ± 1.4	11.7	4.1 ± 0.4	6.4	25 ± 4	0.20 ± 0.07	0.30 ± 0.13	0.09 ± 0.03
86	J1147−619	176.829	−61.978	…	121.9	151.9 ± 1.2	49.5	19.8 ± 0.4	42.0	179 ± 4	0.42 ± 0.01	0.27 ± 0.02	0.037 ± 0.001
87	J1156−566	179.019	−56.675	0.090	9.2	7.6 ± 0.8	8.7	2.1 ± 0.2	0.0	<2.6	0.06 ± 0.10	−1.00 ± 0.15	0.00 ± 0.09
88	J1203−538	180.868	−53.844	…	12.0	10.6 ± 0.9	8.0	2.1 ± 0.3	2.9	9.7 ± 3.3	0.24 ± 0.09	0.1 ± 0.2	−0.00 ± 0.06
89	J1213−648	183.349	−64.844	…	82.3	72.1 ± 0.9	55.9	16.5 ± 0.3	11.7	33 ± 3	0.16 ± 0.01	−0.19 ± 0.04	1.011 ± 0.003
90	J1226−627	186.642	−62.789	…	419.1	591.6 ± 1.4	69.6	25.4 ± 0.4	353.0	1580 ± 4	0.76 ± 0.00	0.59 ± 0.00	0.020 ± 0.001
91	J1235−646	188.792	−64.667	…	31.9	27.5 ± 0.9	10.9	3.0 ± 0.3	12.9	39 ± 3	0.49 ± 0.04	0.35 ± 0.07	0.012 ± 0.010
92	J1237−667	189.312	−66.722	0.117	10.6	8.0 ± 0.8	8.9	2.1 ± 0.2	0.0	<3.6	0.09 ± 0.09	−0.73 ± 0.11	0.13 ± 0.07
93	J1240−577	190.168	−57.791	…	9.7	10.6 ± 1.1	10.4	2.7 ± 0.3	5.3	17 ± 3	0.10 ± 0.09	0.40 ± 0.17	0.19 ± 0.04
94	J1243−630	190.931	−63.076	…	19.9	19.8 ± 1.0	10.3	3.3 ± 0.3	2.1	7.2 ± 3.5	0.31 ± 0.06	−0.3 ± 0.2	0.04 ± 0.02

Table 4
(Continued)

(1) No.	(2) 3MAXI	(3) R.A.	(4) Decl.	(5) $\sigma_{\rm stat}$ [a]	(6) $s_{D,4-10\,\rm keV}$	(7) $f_{4-10\rm keV}$ [b]	(8) $s_{D,3-4\,\rm keV}$	(9) $f_{3-4\,\rm keV}$ [c]	(10) $s_{D,10-20\,\rm keV}$	(11) $f_{10-20\rm keV}$ [d]	(12) HR1 [e]	(13) HR2 [f]	(14) $\sigma^2_{\rm rms}$ [g]
95	J1249−590	192.401	−59.071	⋯	62.1	69.1 ± 1.1	75.9	23.8 ± 0.3	12.7	39 ± 3	−0.04 ± 0.01	−0.09 ± 0.05	0.338 ± 0.002
96	J1257−692	194.396	−69.292	⋯	431.0	504.4 ± 1.2	325.5	161.1 ± 0.5	65.1	177 ± 3	−0.00 ± 0.00	−0.32 ± 0.01	0.001 ± 0.000
97	J1301−615	195.300	−61.595	⋯	371.1	479.9 ± 1.3	180.1	78.8 ± 0.4	146.7	523 ± 4	0.32 ± 0.00	0.23 ± 0.01	1.444 ± 0.002
98	J1302−639	195.602	−63.908	⋯	40.9	38.9 ± 1.0	21.0	6.9 ± 0.3	12.7	41 ± 3	0.29 ± 0.03	0.22 ± 0.06	0.114 ± 0.005
99	J1314−602	198.672	−60.240	0.162	8.3	7.0 ± 0.8	7.9	2.2 ± 0.3	1.8	5.5 ± 3.1	0.02 ± 0.11	0.1 ± 0.4	0.21 ± 0.07
100	J1317−629	199.432	−62.995	⋯	10.7	16.3 ± 1.5	20.4	7.2 ± 0.4	1.1	3.9 ± 3.4	−0.16 ± 0.06	−0.5 ± 0.3	0.03 ± 0.01
101	J1325−577	201.279	−57.725	0.053	22.3	18.7 ± 0.8	33.7	9.2 ± 0.3	0.0	<4.5	−0.22 ± 0.03	−0.80 ± 0.05	−0.02 ± 0.02
102	J1326−621	201.616	−62.147	⋯	67.9	123.6 ± 1.8	66.8	24.8 ± 0.4	30.5	106 ± 4	0.23 ± 0.01	0.11 ± 0.02	0.024 ± 0.001
103	J1331−549	202.914	−54.947	0.122	9.9	8.7 ± 0.9	7.0	1.8 ± 0.3	0.0	<6.3	0.20 ± 0.10	−0.33 ± 0.08	0.18 ± 0.06
104	J1345−623	206.256	−62.382	0.089	13.4	13.1 ± 1.0	13.9	4.7 ± 0.3	0.0	<4.2	−0.06 ± 0.06	−0.88 ± 0.10	−0.01 ± 0.02
105	J1347−606	206.840	−60.648	⋯	17.9	32.9 ± 1.8	27.3	8.0 ± 0.3	11.2	35 ± 3	0.14 ± 0.04	0.22 ± 0.07	0.027 ± 0.007
106	J1356−645	209.147	−64.503	0.069	12.8	28 ± 2	27.5	8.5 ± 0.3	9.6	32 ± 3	0.02 ± 0.05	0.26 ± 0.09	7.967 ± 0.009
107	J1359−633	209.958	−63.352	⋯	13.8	13.7 ± 1.0	8.7	2.9 ± 0.3	2.5	9.0 ± 3.6	0.20 ± 0.08	−0.0 ± 0.2	0.04 ± 0.04
108	J1407−618	211.782	−61.891	⋯	23.1	25.0 ± 1.1	11.9	4.0 ± 0.3	4.8	17 ± 4	0.33 ± 0.05	0.00 ± 0.13	1.48 ± 0.01
109	J1412−653	213.095	−65.310	⋯	20.7	22.1 ± 1.1	10.9	2.7 ± 0.3	14.0	39 ± 3	0.44 ± 0.05	0.44 ± 0.07	0.01 ± 0.01
110	J1419−610	214.835	−61.011	⋯	21.1	22.4 ± 1.1	9.5	3.5 ± 0.4	5.9	23 ± 4	0.35 ± 0.06	0.20 ± 0.13	0.03 ± 0.01
111	J1420−626	215.199	−62.680	⋯	40.8	40.8 ± 1.0	20.6	6.6 ± 0.3	17.2	55 ± 3	0.33 ± 0.03	0.33 ± 0.05	5.236 ± 0.009
112	J1423−541	215.977	−54.177	0.158	7.6	6.8 ± 0.9	10.0	2.7 ± 0.3	0.0	<6.2	−0.11 ± 0.10	−0.23 ± 0.10	−0.09 ± 0.11
113	J1442−626	220.687	−62.635	0.039	30.3	25.4 ± 0.8	45.4	13.2 ± 0.3	2.7	8.2 ± 3.0	−0.24 ± 0.02	−0.36 ± 0.15	−0.01 ± 0.01
114	J1446−641	221.687	−64.128	⋯	8.7	6.8 ± 0.8	1.1	0.3 ± 0.3	4.1	12 ± 3	0.76 ± 0.19	0.4 ± 0.2	−0.00 ± 0.09
115	J1449−598	222.369	−59.808	⋯	15.9	15.7 ± 1.0	4.6	1.5 ± 0.3	3.5	12 ± 3	0.53 ± 0.09	0.05 ± 0.19	0.13 ± 0.03
116	J1453−553	223.284	−55.389	⋯	23.1	26.2 ± 1.1	19.9	5.5 ± 0.3	8.8	29 ± 3	0.21 ± 0.04	0.23 ± 0.09	0.25 ± 0.01
117	J1455−516	223.981	−51.673	⋯	9.8	9.2 ± 0.9	10.4	2.9 ± 0.3	2.5	8.9 ± 3.5	0.01 ± 0.09	0.2 ± 0.3	0.14 ± 0.06
118	J1502−601	225.726	−60.182	⋯	9.9	9.5 ± 1.0	4.8	1.4 ± 0.3	2.0	6.4 ± 3.1	0.36 ± 0.12	−0.0 ± 0.3	0.21 ± 0.05
119	J1509−667	227.378	−66.723	⋯	16.5	12.4 ± 0.8	4.4	1.0 ± 0.2	5.5	15 ± 3	0.60 ± 0.09	0.27 ± 0.14	0.09 ± 0.04
120	J1513−461	228.479	−46.122	0.084	13.8	15.0 ± 1.1	14.6	4.6 ± 0.3	0.0	<1.7	0.02 ± 0.06	−1.00 ± 0.10	−0.03 ± 0.05
121	J1514−591	228.532	−59.124	⋯	87.6	91.9 ± 1.0	70.0	26.6 ± 0.4	21.1	69 ± 3	0.05 ± 0.01	0.05 ± 0.03	0.008 ± 0.002
122	J1520−571	230.129	−57.195	⋯	395.5	574.2 ± 1.5	255.2	152.4 ± 0.6	54.7	208 ± 4	0.09 ± 0.00	−0.30 ± 0.01	3.712 ± 0.004
123	J1533−658	233.309	−65.862	0.133	8.3	6.2 ± 0.8	5.5	4.5 ± 0.8	3.6	27 ± 8	−0.38 ± 0.17	0.7 ± 0.3	0.41 ± 0.07
124	J1542−523	235.573	−52.373	⋯	179.4	209.4 ± 1.2	87.0	32.8 ± 0.4	81.6	304 ± 4	0.34 ± 0.01	0.36 ± 0.01	0.003 ± 0.001
125	J1547−625	236.951	−62.563	⋯	373.0	447.7 ± 1.2	272.9	133.9 ± 0.5	52.5	157 ± 3	0.03 ± 0.00	−0.32 ± 0.01	0.043 ± 0.001
126	J1548−455	237.126	−45.505	⋯	21.6	28.2 ± 1.3	15.8	4.9 ± 0.3	8.1	32 ± 4	0.30 ± 0.05	0.25 ± 0.10	0.04 ± 0.02
127	J1548−476	237.229	−47.698	0.135	9.0	9.7 ± 1.1	4.7	1.4 ± 0.3	1.8	7.4 ± 4.0	0.37 ± 0.13	0.1 ± 0.4	0.18 ± 0.07
128	J1551−543	237.910	−54.399	⋯	17.9	20.4 ± 1.1	8.4	3.3 ± 0.4	4.2	17 ± 4	0.33 ± 0.07	0.10 ± 0.16	0.11 ± 0.05
129	J1601−607	240.313	−60.750	⋯	64.3	203 ± 3	136.3	57.9 ± 0.4	20.7	66 ± 3	0.06 ± 0.01	−0.35 ± 0.02	0.001 ± 0.001
130	J1612−607	243.168	−60.732	⋯	82.1	112.4 ± 1.4	108.8	47.4 ± 0.4	15.3	55 ± 4	−0.14 ± 0.01	−0.16 ± 0.03	0.000 ± 0.001
131	J1617−595	244.460	−59.558	⋯	8.6	12.4 ± 1.4	12.4	3.9 ± 0.3	2.4	8.1 ± 3.4	0.01 ± 0.09	−0.0 ± 0.3	0.07 ± 0.05
132	J1629−613	247.312	−61.314	0.161	7.3	7.3 ± 1.0	15.8	4.2 ± 0.3	3.3	10 ± 3	−0.28 ± 0.08	0.3 ± 0.3	0.00 ± 0.03
133	J1640−324	250.222	−32.469	0.095	7.4	6.4 ± 0.9	5.1	1.3 ± 0.2	0.0	<6.5	0.24 ± 0.14	−0.15 ± 0.10	0.25 ± 0.09
134	J1641−346	250.358	−34.670	0.141	8.2	7.3 ± 0.9	3.0	0.7 ± 0.2	1.4	4.7 ± 3.3	0.53 ± 0.16	−0.0 ± 0.4	0.10 ± 0.09
135	J1650−601	252.530	−60.154	0.065	17.1	20.7 ± 1.2	19.2	6.5 ± 0.3	2.4	9.6 ± 4.0	0.00 ± 0.05	−0.2 ± 0.2	0.01 ± 0.02
136	J1650−330	252.549	−33.018	⋯	11.8	10.9 ± 0.9	7.5	1.9 ± 0.3	4.1	14 ± 3	0.30 ± 0.09	0.3 ± 0.2	0.07 ± 0.04
137	J1653−593	253.365	−59.328	⋯	16.1	26.3 ± 1.6	23.8	8.3 ± 0.3	3.3	13 ± 4	0.01 ± 0.05	−0.15 ± 0.17	0.03 ± 0.02
138	J1655−519	253.995	−51.965	⋯	14.8	14.4 ± 1.0	12.8	3.8 ± 0.3	5.3	19 ± 4	0.09 ± 0.06	0.32 ± 0.16	0.00 ± 0.05
139	J1702−299	255.506	−29.978	0.043	26.3	23.6 ± 0.9	25.5	7.0 ± 0.3	4.8	16 ± 3	0.04 ± 0.03	−0.02 ± 0.13	7.846 ± 0.008
140	J1709−266	257.424	−26.605	⋯	68.1	79.3 ± 1.2	74.6	25.4 ± 0.3	10.8	36 ± 3	−0.00 ± 0.01	−0.20 ± 0.05	8.776 ± 0.004
141	J1710−280	257.543	−28.084	⋯	41.1	46.8 ± 1.1	41.0	12.7 ± 0.3	10.4	35 ± 3	0.08 ± 0.02	0.05 ± 0.06	0.046 ± 0.005

Table 4
(Continued)

(1) No.	(2) 3MAXI	(3) R.A.	(4) Decl.	(5) σ_{stat} [a]	(6) $s_{D,4-10\,keV}$	(7) $f_{4-10keV}$ [b]	(8) $s_{D,3-4\,keV}$	(9) $f_{3-4\,keV}$ [c]	(10) $s_{D,10-20\,keV}$	(11) $f_{10-20keV}$ [d]	(12) HR1 [e]	(13) HR2 [f]	(14) σ^2_{rms} [g]
142	J1712−233	258.079	−23.333	⋯	200.5	345.5 ± 1.7	160.4	93.1 ± 0.6	40.7	186 ± 5	0.08 ± 0.00	−0.12 ± 0.01	−0.001 ± 0.000
143	J1713−241	258.262	−24.146	⋯	28.6	60 ± 2	31.4	15.2 ± 0.5	11.3	52 ± 5	0.12 ± 0.03	0.12 ± 0.06	0.004 ± 0.005
144	J1730−215	262.564	−21.579	⋯	17.5	15.1 ± 0.9	7.6	1.9 ± 0.3	0.0	<5.4	0.43 ± 0.07	−0.65 ± 0.06	−0.01 ± 0.05
145	J1731−169	262.935	−16.961	⋯	1116.8	3026 ± 3	775.6	908 ± 1	266.4	1110 ± 4	0.03 ± 0.00	−0.30 ± 0.00	0.009 ± 0.001
146	J1738−444	264.728	−44.445	⋯	804.7	2248 ± 3	507.2	573 ± 1	238.5	1217 ± 5	0.11 ± 0.00	−0.11 ± 0.00	0.057 ± 0.001
147	J1741−122	265.477	−12.244	⋯	10.6	9.0 ± 0.9	8.5	2.0 ± 0.2	2.2	6.8 ± 3.2	0.17 ± 0.09	0.1 ± 0.3	−0.05 ± 0.07
148	J1750−370	267.548	−37.062	⋯	155.8	504 ± 3	196.4	129.8 ± 0.7	53.9	234 ± 4	0.11 ± 0.01	−0.19 ± 0.01	0.107 ± 0.001
149	J1803−344	270.927	−34.422	0.024	48.3	48.6 ± 1.0	41.5	13.2 ± 0.3	9.0	30 ± 3	0.08 ± 0.02	−0.05 ± 0.07	17.000 ± 0.006
150	J1806−089	271.656	−8.967	0.090	8.9	7.8 ± 0.9	6.0	1.5 ± 0.2	3.1	10 ± 3	0.25 ± 0.12	0.3 ± 0.3	0.16 ± 0.11
151	J1807−369	271.989	−36.943	⋯	8.4	7.9 ± 0.9	8.9	2.4 ± 0.3	3.4	12 ± 4	0.02 ± 0.10	0.4 ± 0.3	13.35 ± 0.02
152	J1810−041	272.576	−4.160	0.077	15.2	13.4 ± 0.9	14.2	3.6 ± 0.3	5.9	19 ± 3	0.08 ± 0.06	0.34 ± 0.14	−0.02 ± 0.04
153	J1814+022	273.502	2.201	0.132	8.6	7.7 ± 0.9	11.8	3.1 ± 0.3	1.9	6.2 ± 3.2	−0.11 ± 0.09	0.1 ± 0.3	−0.03 ± 0.09
154	J1823−347	275.824	−34.796	0.112	10.2	9.7 ± 1.0	13.7	3.9 ± 0.3	1.9	6.6 ± 3.4	−0.12 ± 0.07	−0.0 ± 0.3	0.18 ± 0.07
155	J1823−303	275.914	−30.358	⋯	1264.5	3982 ± 3	796.1	1049 ± 1	420.1	2104 ± 5	0.09 ± 0.00	−0.13 ± 0.00	0.024 ± 0.001
156	J1825−000	276.352	−0.012	⋯	260.4	336.8 ± 1.3	204.6	101.6 ± 0.5	38.6	124 ± 3	0.03 ± 0.00	−0.30 ± 0.01	0.135 ± 0.001
157	J1828−253	277.249	−25.355	0.079	13.8	17.2 ± 1.3	18.6	6.3 ± 0.3	3.4	12 ± 4	−0.07 ± 0.05	−0.00 ± 0.19	14.02 ± 0.01
158	J1829−238	277.362	−23.817	⋯	446.7	713.9 ± 1.6	298.0	186.0 ± 0.6	140.6	551 ± 4	0.10 ± 0.00	0.06 ± 0.00	0.196 ± 0.001
159	J1834−210	278.523	−21.081	⋯	8.4	7.5 ± 0.9	7.6	1.9 ± 0.3	4.2	14 ± 3	0.10 ± 0.11	0.5 ± 0.2	0.11 ± 0.08
160	J1836−194	279.039	−19.400	⋯	24.7	22.7 ± 0.9	27.9	7.5 ± 0.3	5.7	19 ± 3	−0.02 ± 0.03	0.10 ± 0.12	10.379 ± 0.008
161	J1839+050	279.994	5.029	⋯	983.1	2731 ± 3	685.2	852 ± 1	227.0	950 ± 4	0.01 ± 0.00	−0.32 ± 0.00	0.015 ± 0.001
162	J1849−171	282.420	−17.163	0.177	6.5	5.6 ± 0.9	5.4	1.3 ± 0.2	2.3	7.7 ± 3.3	0.15 ± 0.15	0.3 ± 0.4	−0.23 ± 0.14
163	J1855−026	283.869	−2.607	⋯	51.7	53.3 ± 1.0	13.0	3.7 ± 0.3	25.8	83 ± 3	0.64 ± 0.03	0.39 ± 0.03	−0.003 ± 0.004
164	J1855+157	283.900	15.733	⋯	10.9	11.2 ± 1.0	8.0	2.3 ± 0.3	0.0	<7.3	0.22 ± 0.09	−0.37 ± 0.08	0.09 ± 0.05
165	J1858+033	284.579	3.335	⋯	14.8	16.7 ± 1.1	0.0	<0.2	2.9	10.5 ± 3.6	1.00 ± 0.10	−0.0 ± 0.2	1.44 ± 0.04
166	J1858+082	284.656	8.261	0.070	16.4	15.6 ± 1.0	6.6	1.8 ± 0.3	8.0	26 ± 3	0.46 ± 0.08	0.43 ± 0.12	13.84 ± 0.01
167	J1901+014	285.442	1.475	⋯	34.0	34.6 ± 1.0	27.3	8.7 ± 0.3	6.1	20 ± 3	0.12 ± 0.03	−0.09 ± 0.09	0.089 ± 0.010
168	J1904−108	286.119	−10.885	0.041	7.6	6.6 ± 0.9	4.9	1.2 ± 0.2	2.6	8.6 ± 3.2	0.27 ± 0.14	0.3 ± 0.3	0.14 ± 0.08
169	J1904−131	286.205	−13.166	0.104	10.9	9.2 ± 0.8	6.5	1.5 ± 0.2	4.3	14 ± 3	0.32 ± 0.10	0.4 ± 0.2	0.09 ± 0.06
170	J1910+097	287.509	9.729	⋯	52.4	204 ± 4	74.8	47.1 ± 0.6	37.0	153 ± 4	0.16 ± 0.02	0.05 ± 0.02	0.124 ± 0.001
171	J1910−057	287.560	−5.760	⋯	66.2	63.6 ± 1.0	129.5	50.1 ± 0.4	8.7	28 ± 3	−0.42 ± 0.01	−0.22 ± 0.06	14.905 ± 0.005
172	J1910+076	287.675	7.684	⋯	94.4	117.5 ± 1.2	33.2	12.7 ± 0.4	35.2	132 ± 4	0.49 ± 0.01	0.24 ± 0.02	0.008 ± 0.002
173	J1911+005	287.824	0.577	⋯	340.1	488.9 ± 1.4	264.0	154.3 ± 0.6	52.6	175 ± 3	0.00 ± 0.00	−0.31 ± 0.01	6.973 ± 0.004
174	J1911+049	287.989	4.939	⋯	98.1	117.8 ± 1.2	54.0	20.6 ± 0.4	29.7	98 ± 3	0.29 ± 0.01	0.10 ± 0.02	0.079 ± 0.002
175	J1915+109	288.806	10.938	⋯	2271.6	13859 ± 6	1398.5	3612 ± 3	726.7	5485 ± 8	0.10 ± 0.00	−0.26 ± 0.00	0.082 ± 0.003
176	J1918−052	289.707	−5.232	⋯	145.6	156.9 ± 1.1	107.4	38.9 ± 0.4	36.1	118 ± 3	0.12 ± 0.01	0.05 ± 0.02	0.109 ± 0.001
177	J1928+204	292.148	20.411	0.134	9.1	9.4 ± 1.0	6.7	2.0 ± 0.3	3.3	13 ± 4	0.19 ± 0.11	0.3 ± 0.3	0.07 ± 0.07
178	J1929+184	292.377	18.411	⋯	14.8	15.9 ± 1.1	6.2	2.1 ± 0.3	8.9	33 ± 4	0.42 ± 0.08	0.51 ± 0.11	0.69 ± 0.06
179	J1930+096	292.713	9.692	0.069	18.4	19.4 ± 1.1	20.7	6.2 ± 0.3	4.8	17 ± 3	0.00 ± 0.04	0.11 ± 0.14	0.26 ± 0.02
180	J1941+301	295.322	30.183	0.130	9.2	10.3 ± 1.1	3.8	1.2 ± 0.3	1.2	4.8 ± 4.1	0.47 ± 0.13	−0.2 ± 0.4	0.14 ± 0.10
181	J1941+258	295.488	25.861	0.129	9.4	10.0 ± 1.1	5.1	1.6 ± 0.3	3.0	12 ± 4	0.34 ± 0.12	0.3 ± 0.3	0.21 ± 0.05
182	J1942+224	295.602	22.466	⋯	8.7	9.9 ± 1.1	2.8	1.0 ± 0.3	2.2	9.6 ± 4.4	0.53 ± 0.16	0.2 ± 0.3	0.03 ± 0.08
183	J1944+212	296.092	21.207	⋯	10.0	11.3 ± 1.1	9.2	2.9 ± 0.3	2.1	8.3 ± 4.0	0.10 ± 0.09	0.0 ± 0.3	0.05 ± 0.06
184	J1945+274	296.365	27.410	⋯	58.9	68.2 ± 1.2	29.1	10.0 ± 0.3	22.6	93 ± 4	0.37 ± 0.02	0.33 ± 0.04	7.415 ± 0.005
185	J1946+449	296.688	44.920	⋯	7.3	8.9 ± 1.2	4.2	1.4 ± 0.3	0.0	<9.3	0.32 ± 0.15	−0.13 ± 0.09	0.44 ± 0.12
186	J1949+301	297.423	30.160	⋯	52.9	65.6 ± 1.2	37.0	13.5 ± 0.4	18.8	78 ± 4	0.22 ± 0.02	0.27 ± 0.04	8.259 ± 0.005
187	J1955+321	298.885	32.116	⋯	65.9	143 ± 2	47.2	24.2 ± 0.5	27.2	144 ± 5	0.31 ± 0.02	0.19 ± 0.03	0.486 ± 0.003
188	J1958+352	299.596	35.201	⋯	1297.3	5828 ± 4	1053.6	2565 ± 2	466.4	3273 ± 7	−0.16 ± 0.00	−0.10 ± 0.00	0.019 ± 0.001

Table 4
(Continued)

(1) No.	(2) 3MAXI	(3) R.A.	(4) Decl.	(5) $\sigma_{\rm stat}$ [a]	(6) $s_{D,4-10\,{\rm keV}}$	(7) $f_{4-10{\rm keV}}$ [b]	(8) $s_{D,3-4\,{\rm keV}}$	(9) $f_{3-4\,{\rm keV}}$ [c]	(10) $s_{D,10-20\,{\rm keV}}$	(11) $f_{10-20{\rm keV}}$ [d]	(12) HR1 [e]	(13) HR2 [f]	(14) $\sigma^2_{\rm rms}$ [g]
189	J1959+408	299.848	40.804	⋯	47.8	61.4 ± 1.3	37.2	14.6 ± 0.4	11.4	50 ± 4	0.14 ± 0.02	0.09 ± 0.06	0.002 ± 0.005
190	J1959+117	299.860	11.712	⋯	279.3	401.4 ± 1.4	264.8	168.7 ± 0.6	16.9	60 ± 4	−0.14 ± 0.00	−0.64 ± 0.01	0.118 ± 0.001
191	J1959+322	299.975	32.290	⋯	6.9	34 ± 5	12.1	6.0 ± 0.5	1.3	6.8 ± 5.3	0.29 ± 0.12	−0.6 ± 0.3	0.24 ± 0.01
192	J2008+325	302.075	32.528	⋯	11.7	14.6 ± 1.2	9.1	3.5 ± 0.4	2.6	12.2 ± 4.7	0.14 ± 0.08	0.1 ± 0.3	0.05 ± 0.06
193	J2015+370	303.996	37.083	⋯	15.7	18.9 ± 1.2	13.3	5.2 ± 0.4	1.8	8.5 ± 4.7	0.07 ± 0.06	−0.2 ± 0.3	0.08 ± 0.05
194	J2022+371	305.510	37.138	0.089	12.6	17.3 ± 1.4	15.3	26 ± 2	0.0	<34.0	−0.64 ± 0.07	0.14 ± 0.04	0.02 ± 0.05
195	J2032+376	308.041	37.644	⋯	111.3	160.3 ± 1.4	56.8	25.2 ± 0.4	33.4	153 ± 5	0.34 ± 0.01	0.17 ± 0.02	0.628 ± 0.002
196	J2032+409	308.097	40.954	⋯	779.0	2777 ± 4	389.6	475 ± 1	280.3	1895 ± 7	0.30 ± 0.00	0.00 ± 0.00	0.122 ± 0.002
197	J2037+418	309.409	41.897	⋯	31.4	65 ± 2	25.2	16.1 ± 0.6	1.2	6.6 ± 5.4	0.12 ± 0.03	−0.74 ± 0.15	0.055 ± 0.006
198	J2052+443	313.074	44.376	0.121	9.3	11.9 ± 1.3	12.2	4.8 ± 0.4	1.9	9.1 ± 4.8	−0.11 ± 0.08	0.1 ± 0.3	0.10 ± 0.06
199	J2056+497	314.114	49.732	⋯	13.3	15.7 ± 1.2	13.5	4.8 ± 0.4	2.6	11.9 ± 4.5	0.02 ± 0.06	0.1 ± 0.2	0.11 ± 0.04
200	J2103+456	315.844	45.674	⋯	34.8	46.4 ± 1.3	21.4	8.7 ± 0.4	11.1	51 ± 5	0.26 ± 0.03	0.23 ± 0.07	1.196 ± 0.006
201	J2123+423	320.999	42.339	⋯	7.8	9.3 ± 1.2	3.1	1.0 ± 0.3	4.7	21 ± 4	0.48 ± 0.16	0.5 ± 0.2	0.46 ± 0.15
202	J2124+509	321.142	50.995	⋯	42.2	58.1 ± 1.4	30.1	12.1 ± 0.4	13.3	61 ± 5	0.21 ± 0.02	0.22 ± 0.06	0.009 ± 0.006
203	J2128+570	322.082	57.027	⋯	21.4	24.0 ± 1.1	17.9	6.1 ± 0.3	4.7	19 ± 4	0.11 ± 0.04	0.08 ± 0.14	0.08 ± 0.02
204	J2134+511	323.593	51.180	⋯	16.0	21.3 ± 1.3	8.7	3.3 ± 0.4	7.3	34 ± 5	0.35 ± 0.07	0.40 ± 0.12	0.01 ± 0.03
205	J2136+475	324.025	47.575	⋯	8.3	10.1 ± 1.2	5.8	2.0 ± 0.3	2.6	12.0 ± 4.6	0.24 ± 0.12	0.3 ± 0.3	0.03 ± 0.09
206	J2142+435	325.685	43.516	⋯	25.1	30.8 ± 1.2	19.8	7.2 ± 0.4	6.8	30 ± 4	0.15 ± 0.04	0.18 ± 0.11	0.24 ± 0.02
207	J2143+572	325.772	57.286	0.149	8.0	9.0 ± 1.1	6.4	2.1 ± 0.3	0.0	<7.8	0.15 ± 0.12	−0.25 ± 0.10	0.20 ± 0.08
208	J2207+545	331.957	54.556	⋯	66.1	89.3 ± 1.4	36.6	14.9 ± 0.4	17.9	84 ± 5	0.31 ± 0.02	0.16 ± 0.04	0.205 ± 0.004
209	J2228+611	337.039	61.102	0.159	7.6	7.1 ± 0.9	4.1	1.2 ± 0.3	0.0	<6.0	0.32 ± 0.15	−0.33 ± 0.11	0.14 ± 0.08
210	J2235+634	338.912	63.401	⋯	9.4	8.9 ± 0.9	6.4	1.8 ± 0.3	6.3	22 ± 4	0.21 ± 0.11	0.57 ± 0.16	0.07 ± 0.09
211	J2245+534	341.294	53.402	0.120	9.9	11.3 ± 1.1	10.4	3.5 ± 0.3	1.0	4.4 ± 4.4	0.01 ± 0.09	−0.3 ± 0.5	0.15 ± 0.07
212	J2253+626	343.290	62.617	⋯	10.0	11.8 ± 1.2	19.4	6.0 ± 0.3	1.3	4.7 ± 3.6	−0.23 ± 0.06	−0.3 ± 0.4	−0.02 ± 0.05
213	J2323+588	350.855	58.824	⋯	261.9	387.4 ± 1.5	280.5	206.4 ± 0.7	20.9	80 ± 4	−0.25 ± 0.00	−0.54 ± 0.01	0.001 ± 0.001
214	J2346+517	356.609	51.716	⋯	9.1	10.5 ± 1.2	8.5	2.9 ± 0.3	0.0	<4.6	0.07 ± 0.10	−0.93 ± 0.15	0.11 ± 0.08

Notes.
[a] The 1σ statistical position error in units of degrees.
[b] The observed 4–10 keV flux in units of 10^{-12} erg cm^{-2} s^{-1}, converted from Crab units by assuming a Crab-like spectrum; 1 mCrab = 1.21×10^{-11} erg cm^{-2} s^{-1}.
[c] The observed 3–4 keV flux in units of 10^{-12} erg cm^{-2} s^{-1}, converted from Crab units by assuming a Crab-like spectrum; 1 mCrab = 3.98×10^{-12} erg cm^{-2} s^{-1}.
[d] The observed 10–20 keV flux in units of 10^{-12} erg cm^{-2} s^{-1}, converted from Crab units by assuming a Crab-like spectrum; 1 mCrab = 8.51×10^{-12} erg cm^{-2} s^{-1}.
[e] HR(3–4 keV, 4–10 keV) calculated with Equation (2).
[f] HR(4–10 keV, 10–20 keV) calculated with Equation (2).
[g] Excess variance calculated with Equation (3).

Table 5
Properties of the 73-day Sources in the MAXI/GSC Catalog at $|b| < 10°$

(1) No.	(2) 3MAXI	(3) R.A.	(4) Decl.	(5) σ_{stat}[a]	(6) $s_{D,4-10\ keV}$	(7) $f_{4-10keV}$[b]	(8) $s_{D,3-4\ keV}$	(9) f_{3-4keV}[c]	(10) $s_{D,10-20\ keV}$	(11) $f_{10-20keV}$[d]	(12) HR1[e]	(13) HR2[e]	(14) σ^2_{rms}[f]	(15) Period[g]
215	J0716−196	109.060	−19.695	0.144	8.0	30 ± 4	5.2	5 ± 1	1.4	20 ± 14	0.28 ± 0.13	−0.0 ± 0.4	2.98 ± 0.05	
216	J0836−432	129.022	−43.223	0.016	58.2	700 ± 12	24.4	95 ± 4	27.7	958 ± 35	0.40 ± 0.02	0.34 ± 0.03	7.99 ± 0.01	
217	J1619−382	244.769	−38.250	0.066	12.3	98 ± 8	10.5	27 ± 3	4.2	112 ± 26	0.08 ± 0.08	0.25 ± 0.19	11.6 ± 0.1	
218	J1719−284	259.804	−28.410	0.135	7.9	48 ± 6	6.1	11 ± 2	3.1	65 ± 21	0.15 ± 0.12	0.3 ± 0.3	10.5 ± 0.2	
219	J1846+007	281.560	0.800	0.077	11.8	70 ± 6	5.9	11 ± 2	2.9	52 ± 18	0.35 ± 0.10	0.0 ± 0.2	1.62 ± 0.05	
220	J1903+031	285.847	3.162	0.114	10.0	52 ± 5	7.6	14 ± 2	3.6	60 ± 16	0.09 ± 0.10	0.3 ± 0.2	12.8 ± 0.2	
221	J2023+336	305.919	33.698	0.165	6.6	55 ± 8	1.4	3 ± 2	1.5	41 ± 28	0.7 ± 0.2	0.1 ± 0.4	11.1 ± 0.4	

Notes.
[a] The 1σ statistical position error in units of degrees.
[b] The observed 4–10 keV flux in units of 10^{-12} erg cm^{-2} s^{-1}, converted from Crab units by assuming a Crab-like spectrum; 1 mCrab = 1.21×10^{-11} erg cm^{-2} s^{-1}.
[c] The observed 3–4 keV flux in units of 10^{-12} erg cm^{-2} s^{-1}, converted from Crab units by assuming a Crab-like spectrum; 1 mCrab = 3.98×10^{-12} erg cm^{-2} s^{-1}.
[d] The observed 10–20 keV flux in units of 10^{-12} erg cm^{-2} s^{-1}, converted from Crab units by assuming a Crab-like spectrum; 1 mCrab = 8.51×10^{-12} erg cm^{-2} s^{-1}.
[e] HR calculated with Equation (2).
[f] Excess variance calculated with Equation (3).
[g] The period when these source properties are measured.

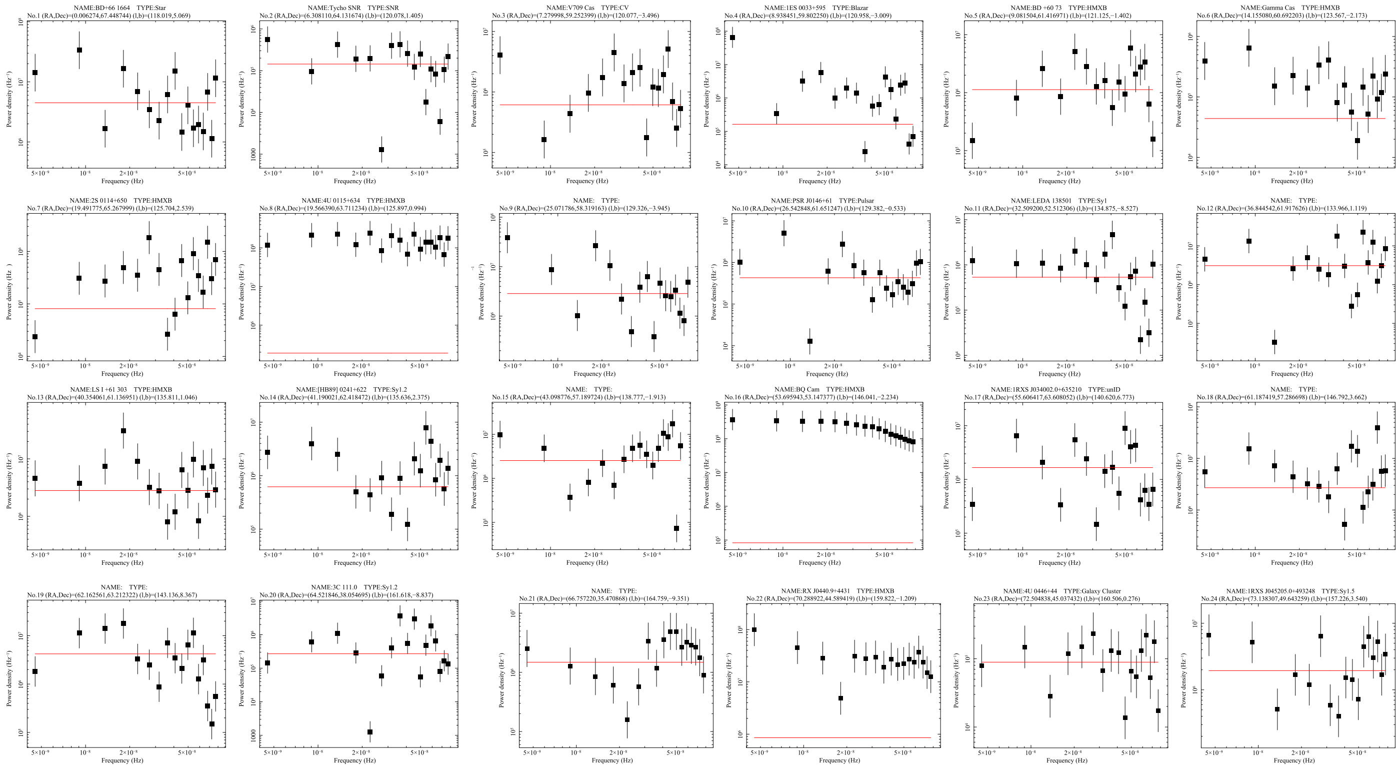

Figure 9. (a) The normalized periodograms. The red dotted lines show the level of Poisson fluctuations. The errors refer to the constant variance of 0.31 (Papadakis & Lawrence 1993; Isobe et al. 2015). (b) The normalized periodograms for 73-day sources. The red dotted lines show the level of Poisson fluctuations. The errors refer to the constant variance of 0.31 (Papadakis & Lawrence 1993; Isobe et al. 2015).

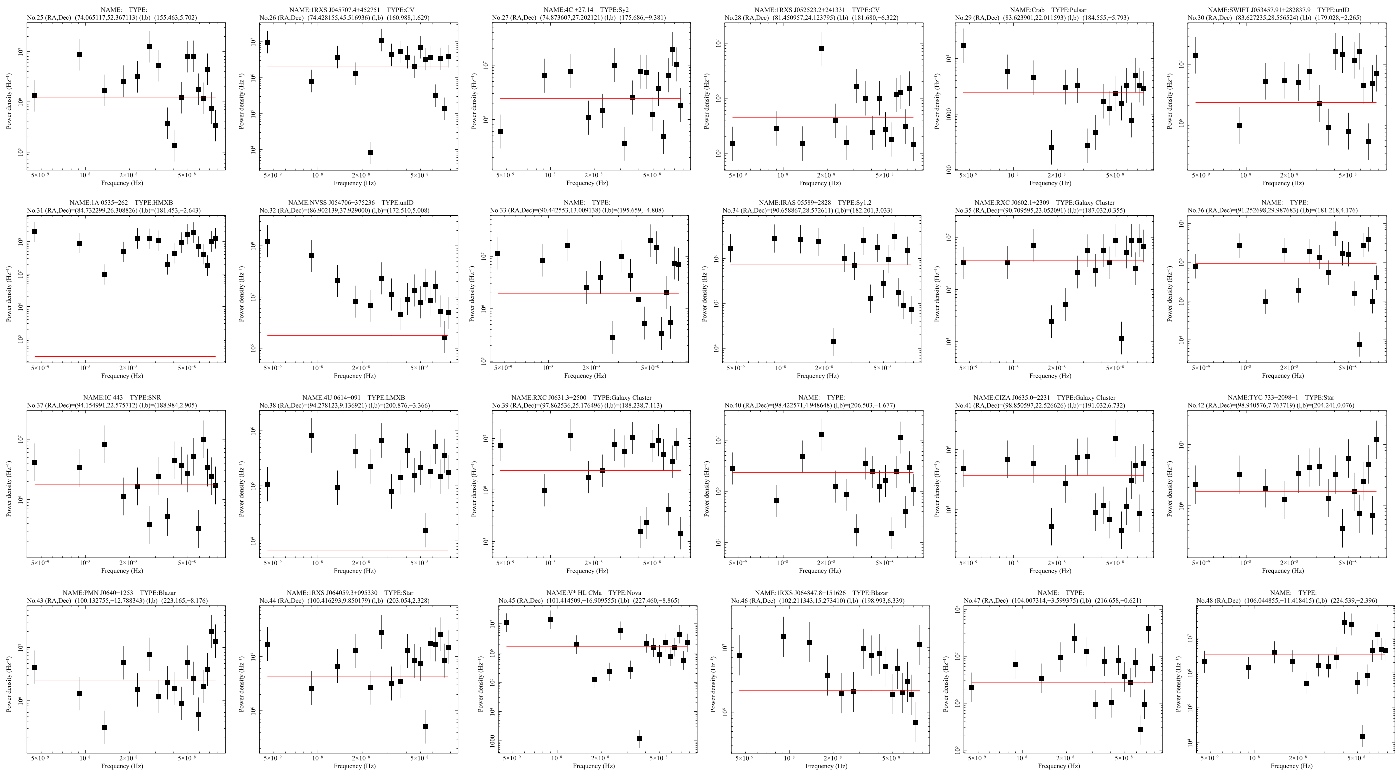

Figure 9. (Continued.)

calibration, which was estimated from the variation seen in the 73-day bin light curve of the Crab Nebula.

To quantify the variability of each source, we use the excess variance ($\sigma^2_{\rm rms}$) normalized by the square of the mean flux (Vaughan et al. 2003):

$$\sigma^2_{\rm rms} = \frac{1}{N\bar{x}^2}\sum_{i=1}^{N}[(x_i - \bar{x})^2 - \epsilon_i^2], \tag{3}$$

where N is the total number of light curve points, $\bar{x}$ is the mean of the flux, and x_i and ϵ_i are the flux and its error for each data point, respectively. The $\sigma^2_{\rm rms}$ value becomes larger in stronger variability. The error on $\sigma^2_{\rm rms}$ ($\Delta\sigma^2_{\rm rms}$) can be calculated via:

$$\Delta\sigma^2_{\rm rms} = \sqrt{\left(\sqrt{\frac{2}{N}}\frac{\overline{\epsilon^2}}{\bar{x}^2}\right)^2 + \frac{\overline{\epsilon^2}}{N}\frac{4\sigma^2_{\rm rms}}{\bar{x}^2}}, \tag{4}$$

where $\overline{\epsilon^2}$ is the mean of the square of ϵ_i. These values for each source are listed in the 14th Column of Tables 4 and 5.

Periodograms are commonly used to quantify the variability of X-ray sources. Employing the same method as Isobe et al. (2015), we made the periodograms of the individual MAXI sources from their 73-day bin light curves. We adopted the following formula to estimate the PSD for each source:

$$P(f) = \frac{[a^2(f) + b^2(f)]T}{\mu^2},$$
$$a(f) = \frac{1}{n}\sum_{j=0}^{n-1} x_j \cos(2\pi f t_j),$$
$$b(f) = \frac{1}{n}\sum_{j=0}^{n-1} x_j \sin(2\pi f t_j), \tag{5}$$

where f is the frequency of the flux variation, x_i is the source flux at time t_j, n is the number of data points, T is the total duration, and μ is the unweighted average of the source flux. A frequency range of 5×10^{-9} Hz to 2×10^{-8} Hz can be investigated from these light curves. Figures 9(a) and (b) show the normalized periodograms for all objects. We note that the result of Cyg X-1 is consistent with those obtained in Sugimoto et al. (2017).

4.3. Mean Properties of Each Source Type

Here, we discuss the overall properties of each source type. Table 8 (3rd to 5th columns) lists the median values of the excess variance and the means and its standard deviations of HRs. Galactic sources constitute the largest population (<50%) in our catalog. As expected, galaxy clusters, (isolated) pulsars, and supernova remnants show stable light curves, while X-ray binaries and blazars have large variabilities. Galaxy clusters, stars, and supernova remnants tend to show a softer spectrum. The majority of high-mass X-ray binaries are X-ray pulsars, which have a hard spectrum below 20 keV because of non-thermal emission characterized by a hard power-law-like spectrum (Nagase 1989). Low-mass X-ray binaries show a softer spectrum in the bright state, characterized by blackbody emission from the surface of a neutron star and multi-color disk emission (Mitsuda et al. 1984).

The unidentified and unmatched sources show, on average, large variability amplitudes ($\sigma^2_{\rm rms} \sim 0.1$–0.2), which are observed from blazars, stars, and X-ray binaries in our catalog. Since their mean HR2 values are ~ -0.1 we infer that the majority are not high-mass X-ray binaries or stars, which show mean HR2 values of ~ 0.1 and ~ -0.3, respectively. In fact, the mean values of HR1 and HR2 of the unidentified and

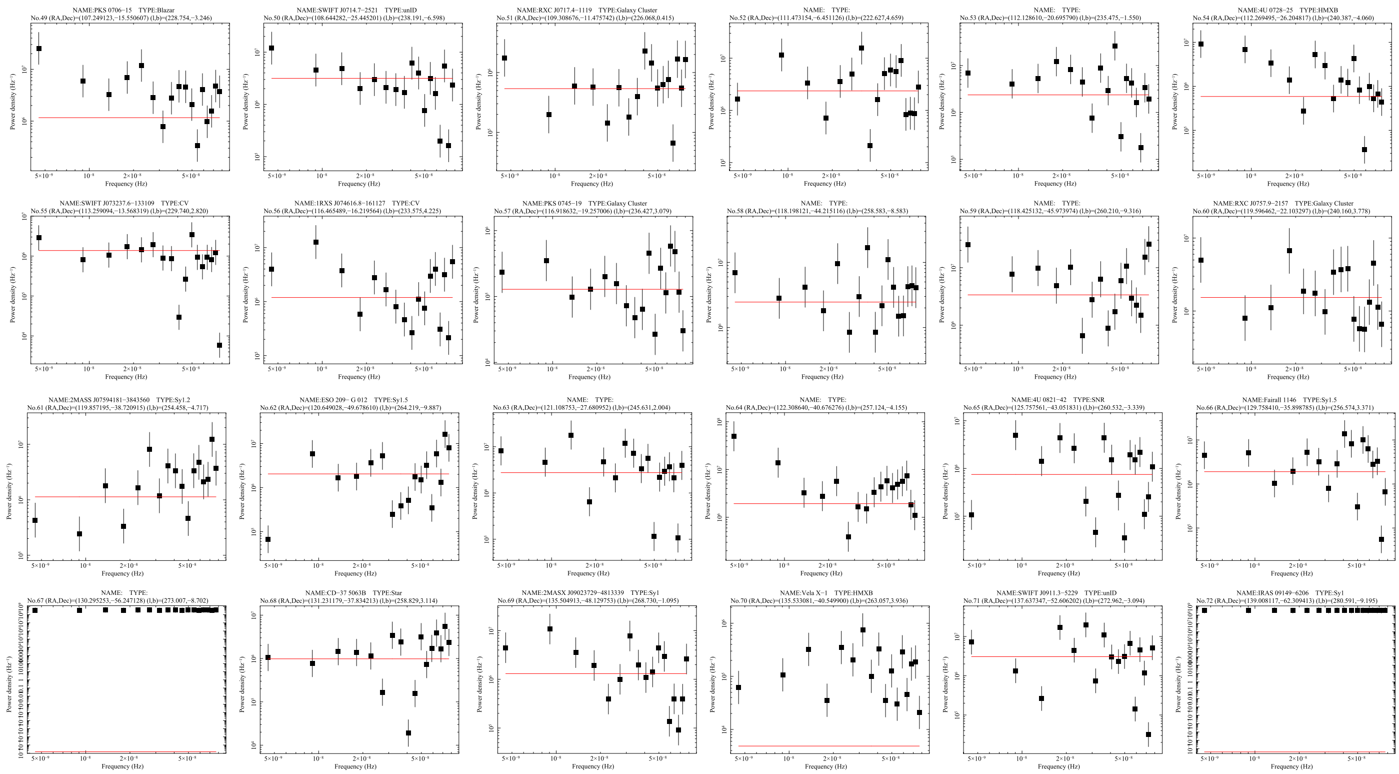

Figure 9. (Continued.)

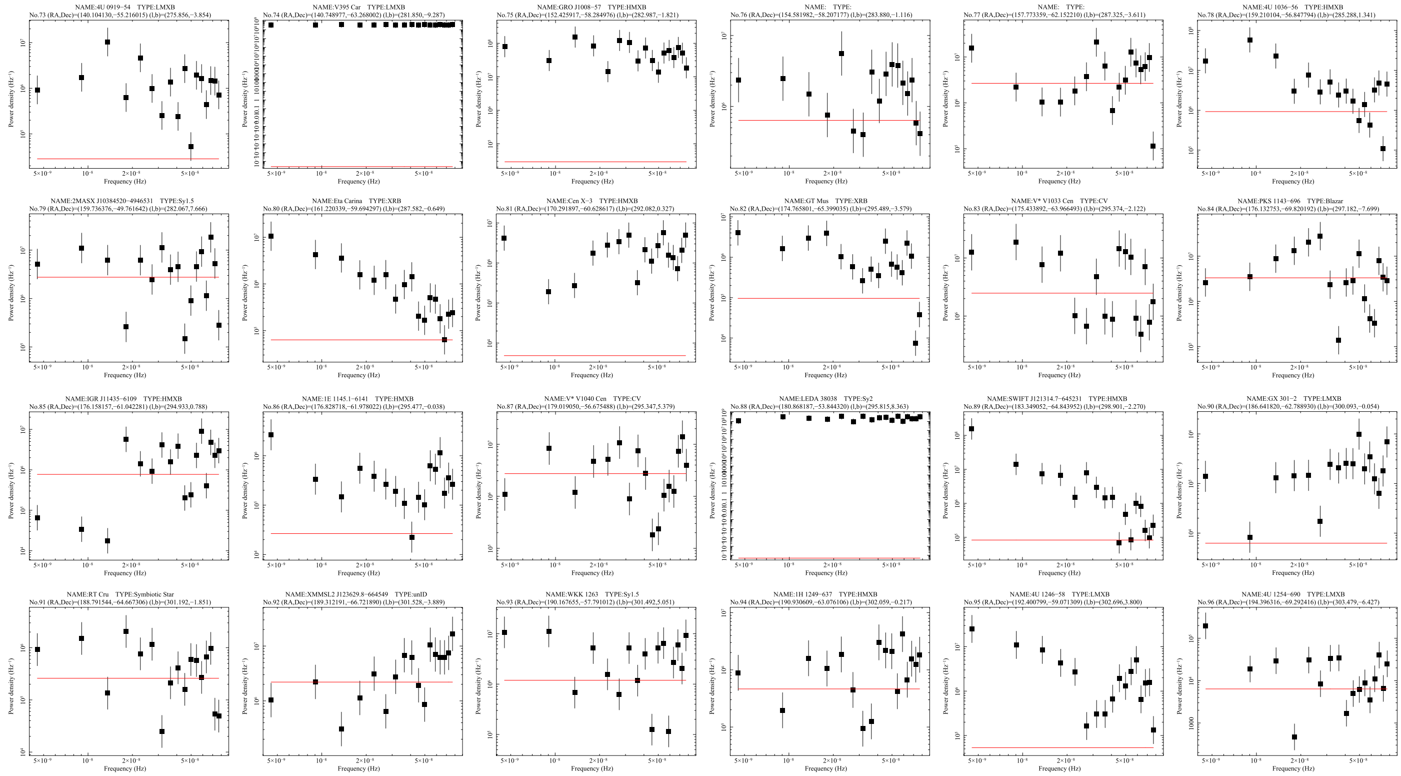

Figure 9. (Continued.)

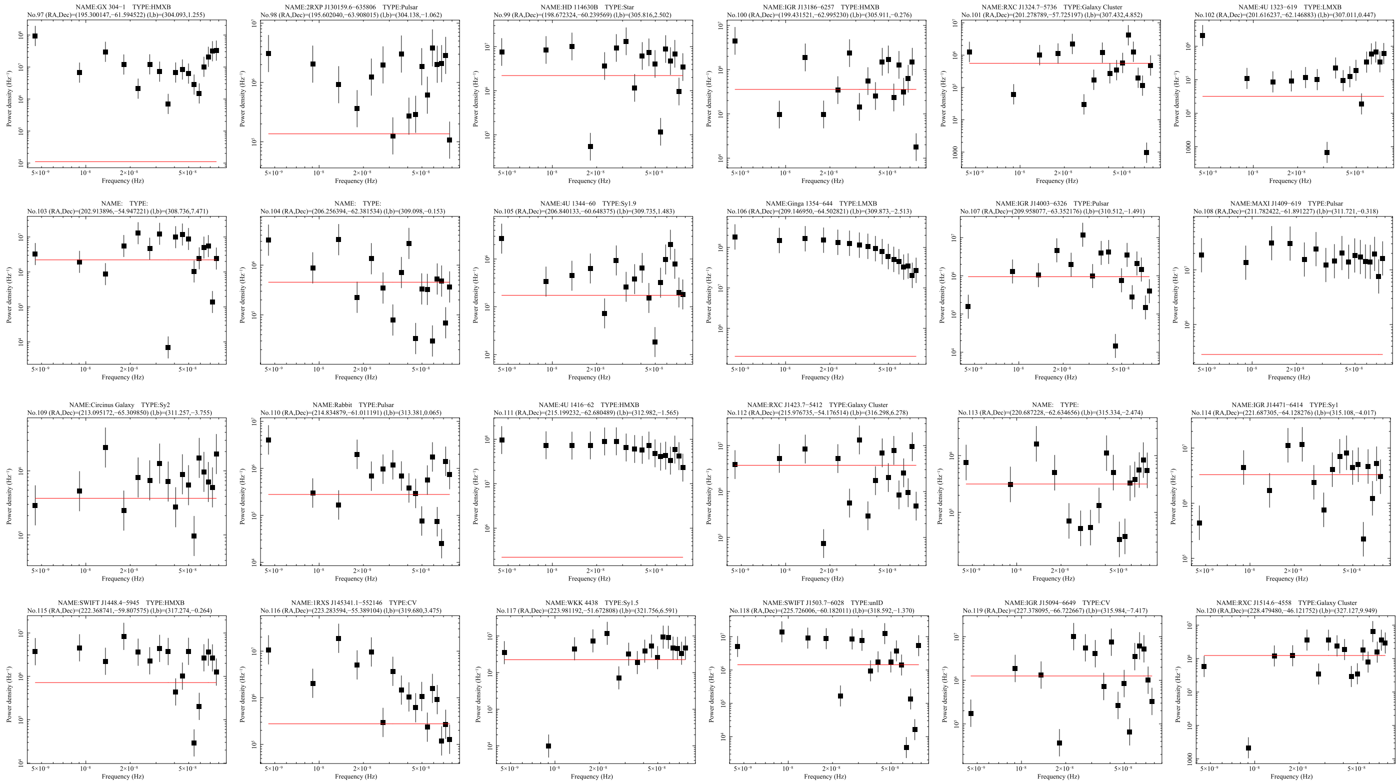

Figure 9. (Continued.)

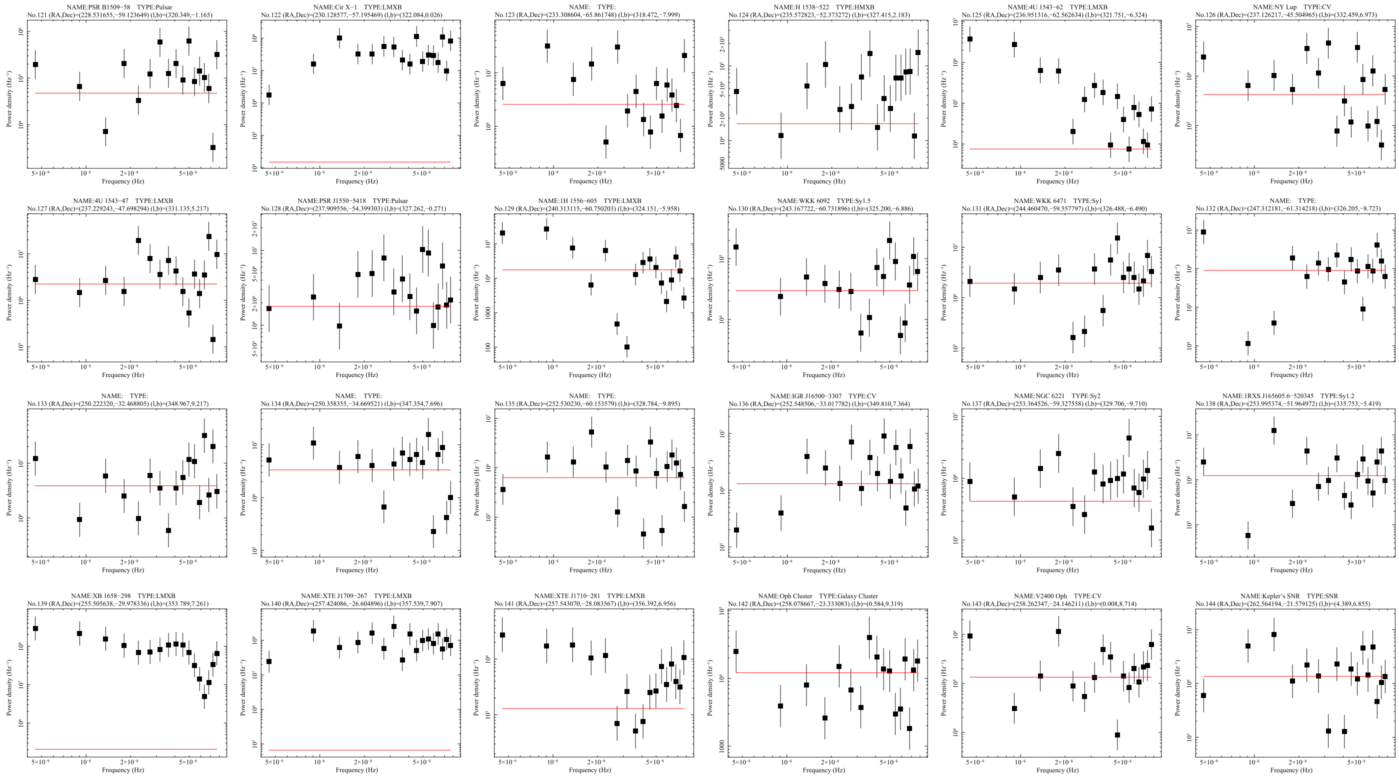

Figure 9. (Continued.)

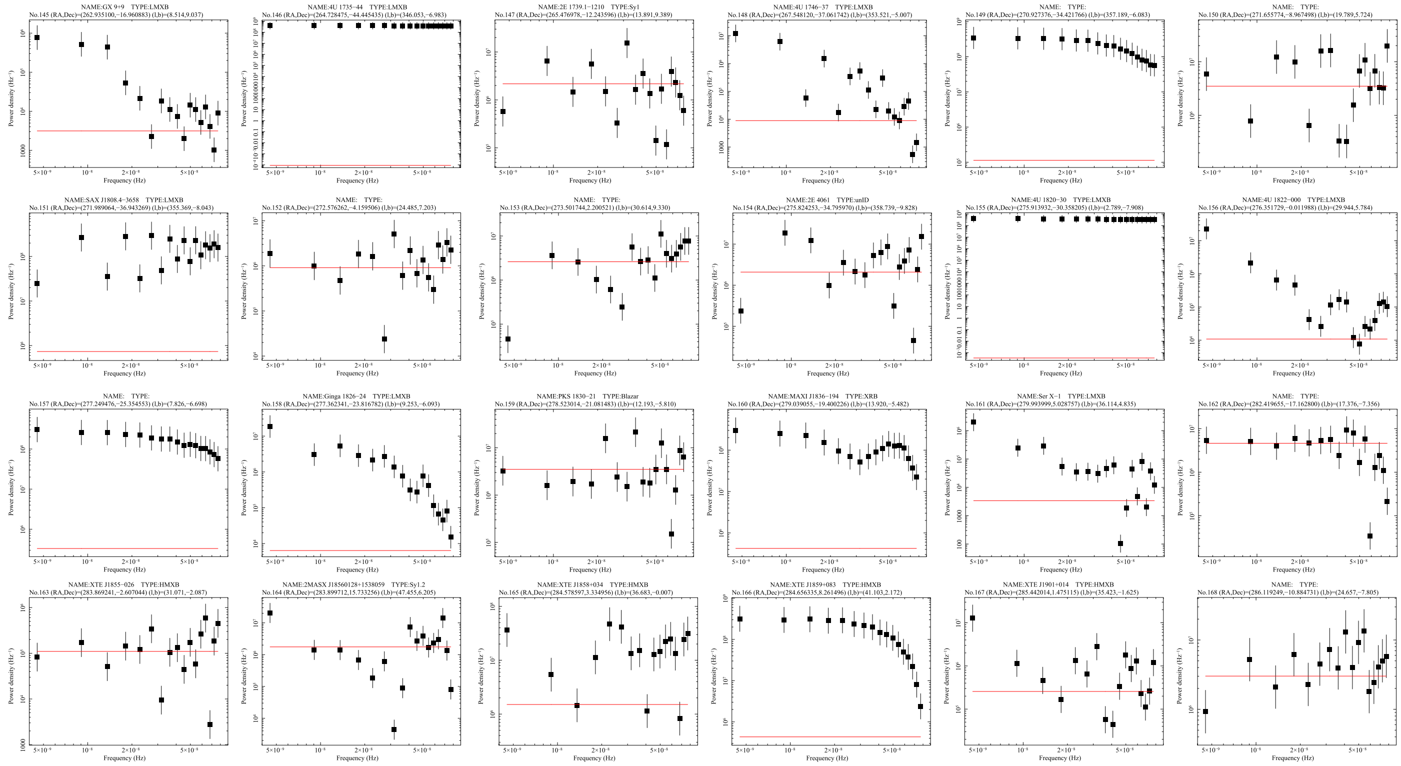

Figure 9. (Continued.)

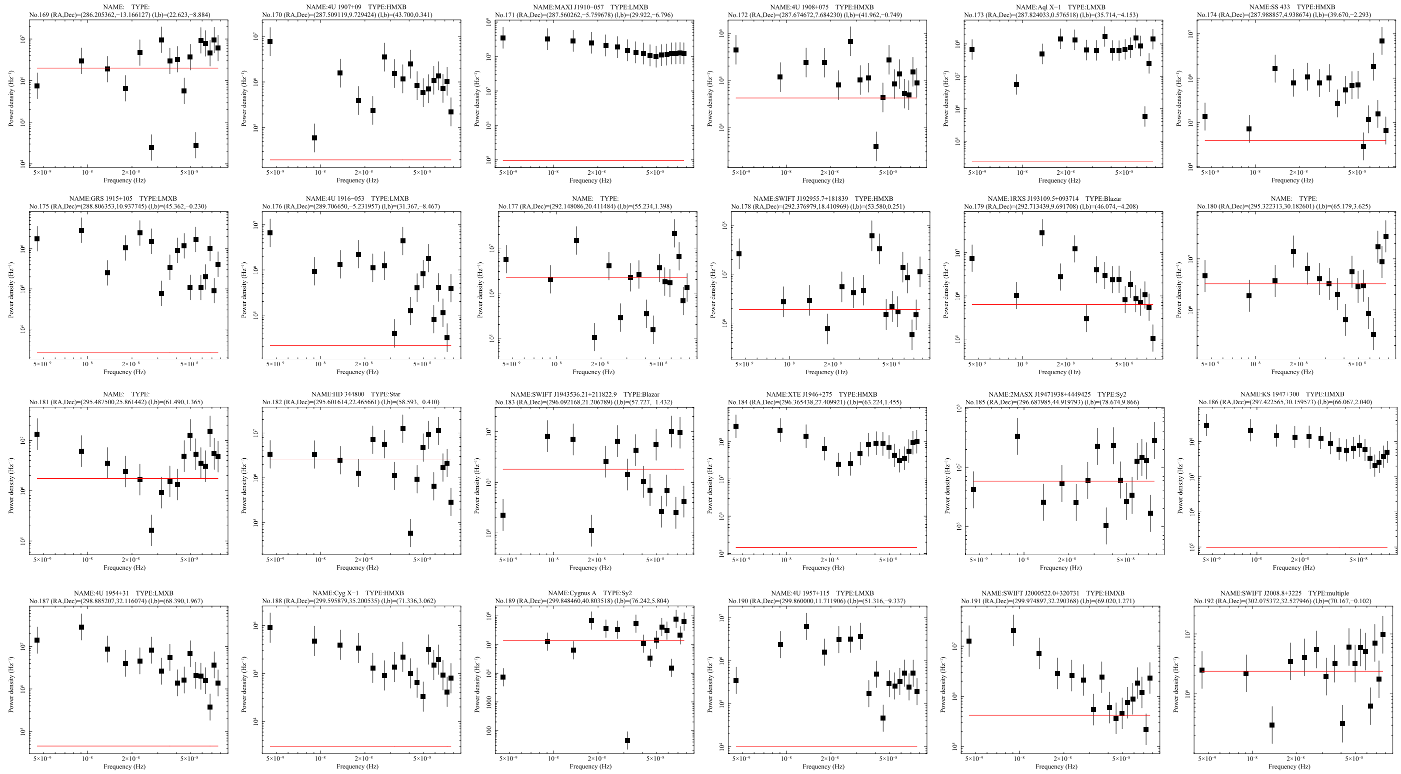

Figure 9. (Continued.)

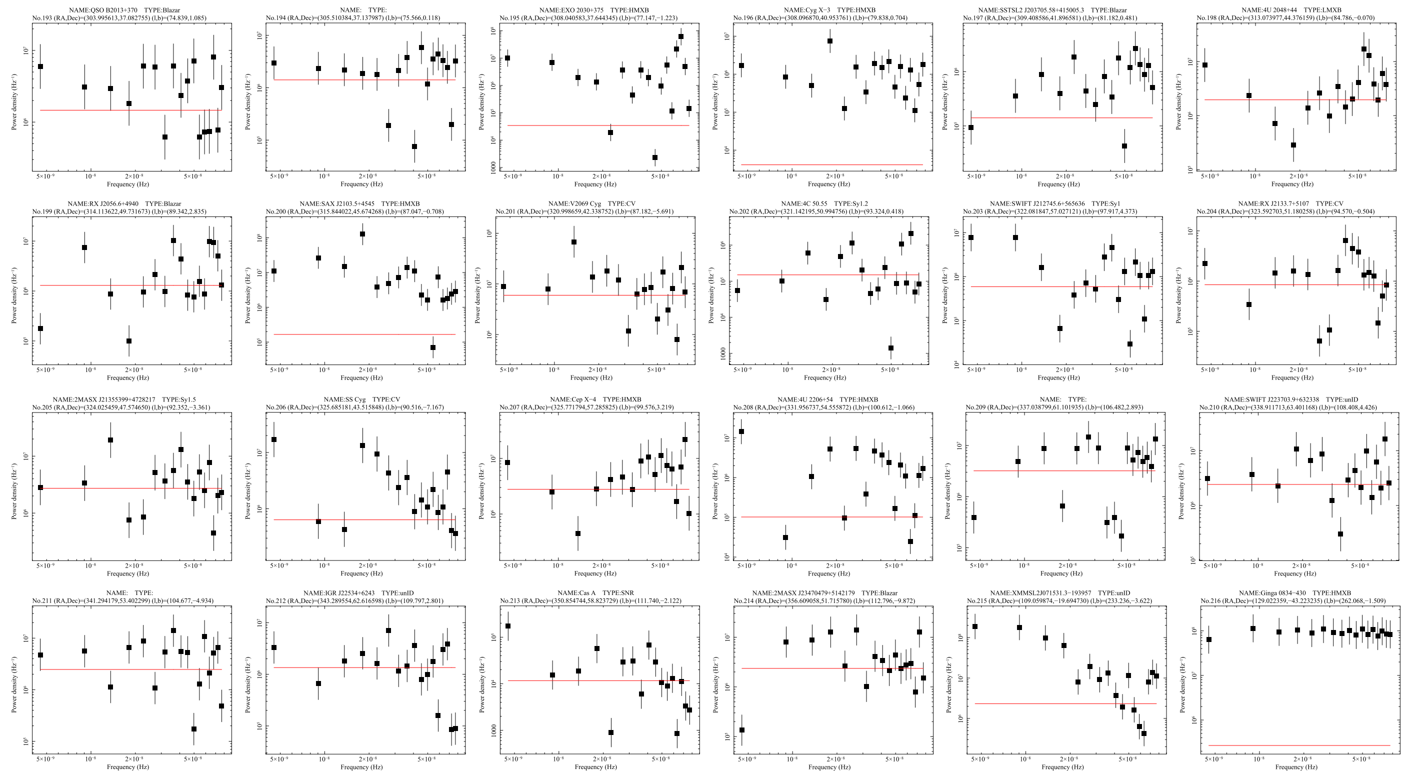

Figure 9. (Continued.)

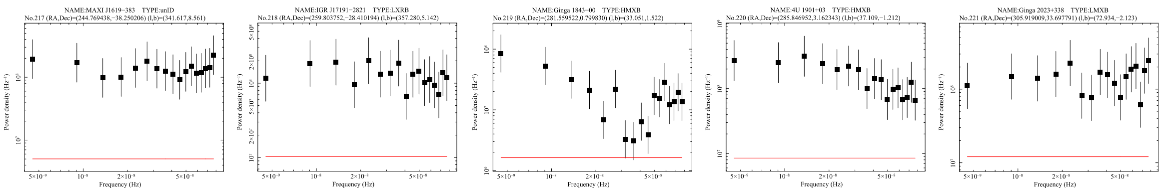

Figure 9. (Continued.)

Table 6
Possible Counterparts for the 7-year Sources in the MAXI/GSC Catalog at $|b| < 10°$

(1)	(2)	(3)	(4)	(5)	(6)	(7)	(8)	(9)
		Possible Counterpart						
No.	3MAXI	Name	R.A.	Decl.	Δposi[a]	Type[b]	Flag[c]	Note[d]
1	J0000+674	BD+66 1664	359.544	67.568	0.213	Star	NR	
2	J0025+641	Tycho SNR	6.284	64.165	⋯	SNR	B	
3	J0029+592	V709 Cas	7.204	59.289	⋯	CV	B	
4	J0035+598	1ES 0033+595	8.969	59.835	⋯	Blazar	B	T
5	J0036+614	BD +60 73	9.290	61.360	⋯	HMXB	B	
6	J0056+606	Gamma Cas	14.177	60.717	⋯	HMXB	B	
7	J0117+652	2S 0114+650	19.511	65.292	⋯	HMXB	B	
8	J0118+637	4U 0115+634	19.633	63.740	⋯	HMXB	B	T
9	J0140+583							
10	J0146+616	PSR J0146+61	26.593	61.751	⋯	Pulsar	B	T
11	J0210+525	LEDA 138501	32.393	52.443	⋯	Sy1	B	
12	J0227+619							
13	J0241+611	LS I+61 303	40.132	61.229	⋯	HMXB	B	
14	J0244+624	[HB89] 0241+622	41.240	62.468	⋯	Sy1.2	B	
15	J0252+571							
16	J0334+531	BQ Cam	53.749	53.173	⋯	HMXB	B	T
17	J0342+636	1RXS J034002.0+635210	55.008	63.870	0.372	unID	R	
18	J0404+572							
19	J0408+632							
20	J0418+380	3C 111.0	64.589	38.027	⋯	Sy1.2	B	
21	J0427+354							
22	J0441+445	RX J0440.9+4431	70.247	44.530	⋯	HMXB	B	T
23	J0450+450	4U 0446+44	72.435	45.046	0.050	Galaxy Cluster	UXM	
24	J0452+496	1RXS J045205.0+493248	73.021	49.546	⋯	Sy1.5	B	
25	J0456+523							
26	J0457+455	1RXS J045707.4+452751	74.285	45.464	⋯	CV	B	
27	J0459+272	4C +27.14	74.984	27.101	⋯	Sy2	B	
28	J0525+241	1RXS J052523.2+241331	81.344	24.226	⋯	CV	B	
29	J0534+220	Crab	83.633	22.015	⋯	Pulsar	B	
30	J0534+285	SWIFT J053457.91+282837.9	83.740	28.477	⋯	unID	B	
31	J0538+263	1A 0535+262	84.727	26.316	⋯	HMXB	B	T
32	J0547+379	NVSS J054706+375236	86.774	37.874	⋯	unID	B	
33	J0601+130							
34	J0602+285	IRAS 05589+2828	90.545	28.473	⋯	Sy1.2	B	
35	J0602+230	RXC J0602.1+2309	90.531	23.166	0.200	Galaxy Cluster	M	
36	J0605+299							
37	J0616+225	IC 443	94.200	22.467	0.117	SNR	XR	
38	J0617+091	4U 0614+091	94.280	9.137	⋯	LMXB	B	T
39	J0631+251	RXC J0631.3+2500	97.839	25.016	0.162	Galaxy Cluster	M	
40	J0633+049							
41	J0635+225	CIZA J0635.0+2231	98.764	22.525	⋯	Galaxy Cluster	B	
42	J0635+077	TYC 733-2098-1	98.993	7.922	0.166	Star	N	
43	J0640−127	PMN J0640−1253	100.030	−12.888	⋯	Blazar	B	
44	J0641+098	1RXS J064059.3+095330	100.247	9.892	0.172	Star	R	
45	J0645−169	V* HL CMa	101.322	−16.860	⋯	Nova	B	
46	J0648+152	1RXS J064847.8+151626	102.199	15.274	0.012	Blazar	R	
47	J0656−035							
48	J0704−114							
49	J0708−155	PKS 0706−15	107.301	−15.450	⋯	Blazar	B	
50	J0714−254	SWIFT J0714.7−2521	108.655	−25.290	⋯	unID	B	

Table 6
(Continued)

(1)	(2)	(3)	(4)	(5)	(6)	(7)	(8)	(9)
		Possible Counterpart						
No.	3MAXI	Name	R.A.	Decl.	Δposi[a]	Type[b]	Flag[c]	Note[d]
51	J0717−114	RXC J0717.4−1119	109.362	−11.331	0.154	Galaxy Cluster	M	
52	J0725−064							
53	J0728−206							
54	J0729−262	4U 0728−25	112.223	−26.108	⋯	HMXB	B	
55	J0733−135	SWIFT J073237.6−133109	113.156	−13.518	⋯	CV	B	
56	J0745−162	1RXS J074616.8−161127	116.570	−16.191	⋯	CV	B	
57	J0747−192	PKS 0745−19	116.881	−19.294	⋯	Galaxy Cluster	B	
58	J0752−442							
59	J0753−459							
60	J0758−221	RXC J0757.9−2157	119.495	−21.962	0.170	Galaxy Cluster	M	
61	J0759−387	2MASS J07594181−3843560	119.924	−38.732	⋯	Sy1.2	B	
62	J0802−496	ESO 209- G 012	120.492	−49.777	⋯	Sy1.5	B	
63	J0804−276							
64	J0809−406							
65	J0823−430	4U 0821−42	125.826	−42.907	0.153	SNR	UXNR	
66	J0839−358	Fairall 1146	129.628	−35.993	⋯	Sy1.5	B	
67	J0841−562							
68	J0844−378	CD-37 5063B	131.140	−37.963	0.148	Star	NR	
69	J0902−481	2MASX J09023729−4813339	135.656	−48.226	⋯	Sy1	B	
70	J0902−405	Vela X-1	135.529	−40.555	⋯	HMXB	B	
71	J0910−526	SWIFT J0911.3−5229	137.773	−52.547	⋯	unID	B	
72	J0916−623	IRAS 09149−6206	139.039	−62.325	⋯	Sy1	B	
73	J0920−552	4U 0919−54	140.111	−55.207	⋯	LMXB	B	
74	J0922−632	V395 Car	140.644	−63.295	⋯	LMXB	B	
75	J1009−582	GRO J1008−57	152.446	−58.293	⋯	HMXB	B	T
76	J1018−582							
77	J1031−621							
78	J1036−568	4U 1036−56	159.391	−56.799	⋯	HMXB	B	
79	J1038−497	2MASX J10384520−4946531	159.688	−49.782	⋯	Sy1.5	B	
80	J1044−596	Eta Carina	161.265	−59.684	⋯	Star	B	S
81	J1121−606	Cen X-3	170.316	−60.623	⋯	HMXB	B	
82	J1139−653	GT Mus	174.873	−65.398	⋯	Star	B	S
83	J1141−639	V^{*} V1033 Cen	175.346	−64.172	0.209	CV	N	
84	J1144−698	PKS 1143−696	176.473	−69.900	⋯	Blazar	B	
85	J1144−610	IGR J11435−6109	175.967	−61.150	⋯	HMXB	B	
86	J1147−619	1E 1145.1−6141	176.869	−61.954	⋯	HMXB	B	
87	J1156−566	V^{*} V1040 Cen	178.863	−56.698	0.089	CV	NR	
88	J1203−538	LEDA 38038	180.699	−53.835	⋯	Sy2	B	
89	J1213−648	SWIFT J121314.7−645231	183.321	−64.880	⋯	HMXB	B	
90	J1226−627	GX 301−2	186.657	−62.771	⋯	LMXB	B	T
91	J1235−646	RT Cru	188.724	−64.566	⋯	CV	B	C
92	J1237−667	XMMSL2 J123629.8-664549	189.125	−66.764	0.085	unID	N	
93	J1240−577	WKK 1263	190.357	−57.834	⋯	Sy1.5	B	
94	J1243−630	1H 1249−637	190.709	−63.058	⋯	HMXB	B	
95	J1249−590	4U 1246−58	192.414	−59.087	⋯	LMXB	B	T
96	J1257−692	4U 1254−690	194.405	−69.289	⋯	LMXB	B	
97	J1301−615	GX 304−1	195.322	−61.602	⋯	HMXB	B	
98	J1302−639	2RXP J130159.6−635806	195.494	−63.968	⋯	Pulsar	B	
99	J1314−602	HD 114630B	198.238	−59.820	0.472	Star	NR	
100	J1317−629	IGR J13186−6257	199.607	−62.971	⋯	HMXB	B	
101	J1325−577	RXC J1324.7−5736	201.180	−57.614	0.123	Galaxy Cluster	MNR	
102	J1326−621	4U 1323−619	201.650	−62.136	⋯	LMXB	B	T
103	J1331−549							
104	J1345−623							
105	J1347−606	4U 1344−60	206.900	−60.618	⋯	Sy1.9	B	
106	J1356−645	Ginga 1354−644	209.550	−64.733	0.288	LMXB	X	
107	J1359−633	IGR J14003−6326	210.190	−63.429	⋯	Pulsar	B	
108	J1407−618	MAXI J1409−619	212.011	−61.983	⋯	Pulsar	B	T
109	J1412−653	Circinus Galaxy	213.291	−65.339	⋯	Sy2	B	
110	J1419−610	Rabbit	214.678	−60.967	⋯	Pulsar	B	
111	J1420−626	4U 1416−62	215.303	−62.698	⋯	HMXB	B	
112	J1423−541	RXC J1423.7−5412	215.930	−54.203	0.038	Galaxy Cluster	M	

Table 6
(Continued)

(1)	(2)	(3)	(4)	(5)	(6)	(7)	(8)	(9)
		Possible Counterpart						
No.	3MAXI	Name	R.A.	Decl.	Δposi[a]	Type[b]	Flag[c]	Note[d]
113	J1442−626							
114	J1446−641	IGR J14471−6414	221.617	−64.233	⋯	Sy1	B	
115	J1449−598	SWIFT J1448.4−5945	222.179	−59.704	⋯	HMXB	B	
116	J1453−553	1RXS J145341.1−552146	223.456	−55.362	⋯	CV	B	
117	J1455−516	WKK 4438	223.823	−51.571	⋯	Sy1.5	B	
118	J1502−601	SWIFT J1503.7−6028	226.067	−60.356	⋯	unID	B	
119	J1509−667	IGR J15094−6649	227.358	−66.823	⋯	CV	B	
120	J1513−461	RXC J1514.6−4558	228.651	−45.981	0.184	Galaxy Cluster	MR	
121	J1514−591	PSR B1509−58	228.481	−59.136	⋯	Pulsar	B	
122	J1520−571	Cir X-1	230.170	−57.167	⋯	LMXB	B	T
123	J1533−658							
124	J1542−523	H 1538−522	235.597	−52.386	⋯	HMXB	B	
125	J1547−625	4U 1543−62	236.976	−62.570	⋯	LMXB	B	
126	J1548−455	NY Lup	237.061	−45.478	⋯	CV	B	
127	J1548−476	4U 1543−47	236.855	−47.714	0.252	LMXB	UXN	
128	J1551−543	PSR J1550−5418	237.725	−54.307	⋯	Pulsar	B	
129	J1601−607	1H 1556−605	240.260	−60.738	⋯	LMXB	B	
130	J1612−607	WKK 6092	242.964	−60.632	⋯	Sy1.5	B	
131	J1617−595	WKK 6471	244.652	−59.455	⋯	Sy1	B	
132	J1629−613							
133	J1640−324							
134	J1641−346							
135	J1650−601							
136	J1650−330	IGR J16500−3307	252.482	−33.117	⋯	CV	B	
137	J1653−593	NGC 6221	253.193	−59.217	⋯	Sy2	B	
138	J1655−519	1RXS J165605.6−520345	254.024	−52.061	⋯	Sy1.2	B	
139	J1702−299	XB 1658−298	255.525	−29.950	0.033	LMXB	X	
140	J1709−266	XTE J1709−267	257.377	−26.656	⋯	LMXB	B	T
141	J1710−280	XTE J1710−281	257.552	−28.131	⋯	LMXB	B	
142	J1712−233	Oph Cluster	258.108	−23.376	⋯	Galaxy Cluster	B	
143	J1713−241	V2400 Oph	258.152	−24.246	⋯	CV	B	
144	J1730−215	*Kepler*'s SNR	262.673	−21.480	⋯	SNR	B	
145	J1731−169	GX 9+9	262.934	−16.962	⋯	LMXB	B	
146	J1738−444	4U 1735−44	264.743	−44.450	⋯	LMXB	B	
147	J1741−122	2E 1739.1−1210	265.476	−12.197	⋯	Sy1	B	
148	J1750−370	4U 1746−37	267.553	−37.052	⋯	LMXB	B	
149	J1803−344	1RXS 180408.9−342058	271.052	−34.313	0.150	LMXB		T
150	J1806−089							
151	J1807−369	SAX J1808.4−3658	272.115	−36.979	⋯	LMXB	B	
152	J1810−041							
153	J1814+022							
154	J1823−347	2E 4061	275.910	−34.904	0.129	unID	NR	
155	J1823−303	4U 1820−30	275.919	−30.361	⋯	LMXB	B	T
156	J1825−000	4U 1822−000	276.342	−0.012	⋯	LMXB	B	
157	J1828−253	MAXI J1828−249	277.243	−25.030	0.325	LMXB		T
158	J1829−238	Ginga 1826−24	277.367	−23.791	⋯	LMXB	B	
159	J1834−210	PKS 1830−21	278.416	−21.061	⋯	Blazar	B	
160	J1836−194	MAXI J1836−194	278.931	−19.320	⋯	XRB	B	T
161	J1839+050	Ser X-1	279.990	5.036	⋯	LMXB	B	
162	J1849−171							
163	J1855−026	XTE J1855−026	283.877	−2.605	⋯	HMXB	B	
164	J1855+157	2MASX J18560128+1538059	284.002	15.632	⋯	Sy1.2	B	
165	J1858+033	XTE J1858+034	284.679	3.434	⋯	HMXB	B	T
166	J1858+082	XTE J1859+083	284.750	8.233	0.097	HMXB	X	T
167	J1901+014	XTE J1901+014	285.421	1.438	⋯	HMXB	B	
168	J1904−108							
169	J1904−131							
170	J1910+097	4U 1907+09	287.408	9.830	⋯	HMXB	B	
171	J1910−057	MAXI J1910−057	287.595	−5.799	⋯	LMXB	B	T
172	J1910+076	4U 1908+075	287.700	7.596	⋯	HMXB	B	
173	J1911+005	Aql X-1	287.817	0.585	⋯	LMXB	B	
174	J1911+049	SS 433	287.957	4.983	⋯	HMXB	B	

Table 6
(Continued)

(1)	(2)	(3)	(4)	(5)	(6)	(7)	(8)	(9)
		Possible Counterpart						
No.	3MAXI	Name	R.A.	Decl.	Δposi[a]	Type[b]	Flag[c]	Note[d]
175	J1915+109	GRS 1915+105	288.798	10.946	⋯	LMXB	B	
176	J1918−052	4U 1916−053	289.699	−5.238	⋯	LMXB	B	
177	J1928+204							
178	J1929+184	SWIFT J192955.7+181839	292.482	18.311	⋯	HMXB	B	
179	J1930+096	1RXS J193109.5+093714	292.790	9.621	0.103	Blazar	R	T
180	J1941+301							
181	J1941+258							
182	J1942+224	HD 344800	295.712	22.563	⋯	Star	B	
183	J1944+212	SWIFT J1943536.21+211822.9	295.984	21.306	⋯	Blazar	B	
184	J1945+274	XTE J1946+275	296.414	27.365	⋯	HMXB	B	T
185	J1946+449	2MASX J19471938+4449425	296.831	44.828	⋯	Sy2	B	
186	J1949+301	KS 1947+300	297.377	30.207	⋯	HMXB	B	T
187	J1955+321	4U 1954+31	298.926	32.097	⋯	LMXB	B	T
188	J1958+352	Cyg X-1	299.590	35.202	⋯	HMXB	B	
189	J1959+408	Cygnus A	299.868	40.734	⋯	Sy2	B	
190	J1959+117	4U 1957+115	299.851	11.709	⋯	LMXB	B	
191	J1959+322	SWIFT J2000522.0+320731	300.091	32.189	⋯	HMXB	B	
192	J2008+325	SWIFT J2008.8+3225	302.196	32.430	⋯	multiple	B	
193	J2015+370	QSO B2013+370	303.870	37.183	⋯	Blazar	B	
194	J2022+371							
195	J2032+376	EXO 2030+375	308.063	37.638	⋯	HMXB	B	
196	J2032+409	Cyg X-3	308.107	40.958	⋯	HMXB	B	
197	J2037+418	SSTSL2 J203705.58+415005.3	309.273	41.835	⋯	Blazar	B	
198	J2052+443	4U 2048+44	312.589	44.562	0.393	LMXB	UNR	
199	J2056+497	RX J2056.6+4940	314.178	49.668	⋯	Blazar	B	
200	J2103+456	SAX J2103.5+4545	315.899	45.751	⋯	HMXB	B	
201	J2123+423	V2069 Cyg	320.937	42.301	⋯	CV	B	
202	J2124+509	4C 50.55	321.164	50.973	⋯	Sy1.2	B	
203	J2128+570	SWIFT J212745.6+565636	321.937	56.944	⋯	Sy1	B	
204	J2134+511	RX J2133.7+5107	323.432	51.124	⋯	CV	B	
205	J2136+475	2MASX J21355399+4728217	323.975	47.473	⋯	Sy1.5	B	
206	J2142+435	SS Cyg	325.678	43.586	⋯	CV	B	
207	J2143+572	Cep X-4	324.875	56.983	0.573	HMXB	X	T
208	J2207+545	4U 2206+54	331.984	54.519	⋯	HMXB	B	T
209	J2228+611							
210	J2235+634	SWIFT J223703.9+632338	339.156	63.492	⋯	unID	B	
211	J2245+534							
212	J2253+626	IGR J22534+6243	343.480	62.727	⋯	unID	B	
213	J2323+588	Cas A	350.850	58.815	⋯	SNR	B	
214	J2346+517	2MASX J23470479+5142179	356.770	51.705	⋯	Blazar	B	

Notes.
[a] Angular separation between the MAXI position and that of possible a counterpart in units of degrees.
[b] Sy: Seyfert galaxy, AGN: active galactic nucleus, L(H)MXB: low(high)-mass X-ray binary, XRB: X-ray binary, SNR: supernova remnant, CV: cataclysmic variable, unID: unidentified source.
[c] Cross-matching flag: B, U, X, N, M, and R indicate that the source has one or more counterparts in the BAT105, 4U, XTEASMLONG, XMMSL2, MCXC, and 1RXS, respectively. The counterpart name listed in column (3) is quoted from the catalog expressed by the leftmost letter in this column.
[d] T: Transient or new MAXI source. S: Classified as an XRB in the original catalog (BAT105). C: Classified as a symbiotic star in the original catalog (BAT105).

Table 7
Possible Counterparts for the 73-day Source in the MAXI/GSC Catalog at $|b| < 10°$

(1)	(2)	(3)	(4)	(5)	(6)	(7)	(8)	(9)
		Possible Counterpart						
No.	3MAXI	Name	R.A.	Decl.	Δposi[a]	Type[b]	Flag[c]	Note[d]
215	J0716−196	XMMSL2 J071531.3-193957	108.880	−19.666	0.172	unID	N	
216	J0836−432	Ginga 0834−430	128.979	−43.185	0.050	HMXB	X	
217	J1619−382	MAXI J1619−383	244.925	−38.375	0.175	unID		T
218	J1719−284	IGR J17191−2821	259.808	−28.327	0.083	LMXB	X	T
219	J1846+005	Ginga 1843+00	281.403	0.863	⋯	HMXB	B	
220	J1903+031	4U 1901+03	285.905	3.192	0.065	HMXB	UX	T
221	J2023+336	Ginga 2023+338	306.016	33.867	0.187	LMXB	X	

Notes.
[a] Angular separation between the MAXI position and that of a possible counterpart in units of degree.
[b] Sy: Seyfert galaxy, AGN: active galactic nucleus, L(H)MXB: low(high)-mass X-ray binary, XRB: X-ray binary, SNR: supernova remnant, CV: cataclysmic variable, unID: unidentified source.
[c] Cross-matching flag: B, U, X, N, M, and R indicate that the source has one or more counterparts in the BAT105, 4U, XTEASMLONG, XMMSL2, MCXC, and 1RXS, respectively. The counterpart name listed in column (3) is quoted from the catalog expressed by the leftmost letter in this column.
[d] T: Transient or new MAXI source.

unmatched sources are similar to those of blazars or low-mass X-ray binaries, which are good candidates.

4.4. log N–log S Relation

The log N–log S relation (number counts) represents a basic statistical property of sources detected in a survey observation. To derive this relation, we need to create the sensitivity map, which gives the minimum flux of a source detectable with the adopted significance threshold ($s_{D,4-10\,\mathrm{keV}} > 6.5$) as a function of sky position. Following our previous works (Hiroi et al. 2011, 2013), we estimated the sensitivity at each position using the coverage map (Figure 1) and the background+GRXE map. Here, we utilized simple analytical formulae that are calibrated with the actual relations among flux, significance, exposure, and background from the cataloged sources. The sensitivity map enables us to calculate the survey area as a function of limiting sensitivity (area curve, Figure 10). By dividing the observed flux distribution of sources by the area curve, the log N–log S relation in the differential form is obtained, where the surface number density $n(S)\ dS$ of sources with fluxes between S and $S + dS$ is given. In this paper, considering the low number statistics, we represent it in the integral form $N(>S) \equiv \int_S n(S)dS$, i.e., the total surface number density of sources with fluxes larger than S.

Figure 11 plots the spatially averaged log N–log S relation in the 4–10 keV band of the MAXI sources at $|b| < 10°$ obtained from the whole survey area (excluding the Galactic center and Vela SNR regions). Unlike the case of the high-Galactic-latitude sky, where extragalactic populations are dominant, we expect large variation of source number density among different directions at low Galactic latitudes. To demonstrate this, we also calculated the log N–log S relations from two separate Galactic longitude regions, (1) $l = 30°$–$105°$ and $l = 255°$–$330°$, and (2) $l = 105°$–$255°$, both at $|b| < 10°$. The results and corresponding survey area are also plotted in Figures 10 and 11, respectively.

We find that the slope of the log N–log S relation is flat regardless of the Galactic longitude, which can be roughly approximated by $N(>S) \propto S^{-0.5}$. To evaluate the contributions from different populations, in Figure 12 we compare the log N–log S relations of the identified extragalactic objects (AGNs and galaxy clusters), LMXBs, and HMXBs, which are the most dominant ones in our catalog. As noted, the log N–log S slopes for LMXBs and HMXBs are even flatter than those for 0.5, and they are consistent with the results by Grimm et al. (2002) using the *RXTE*/ASM data at $|b| < 20°$. In a future work, our catalog will be useful to constrain the X-ray luminosity function of Galactic-disk sources covering low luminosity ranges down to $L_X \sim 10^{34-35}$ erg s^{-1} (assuming a mean distance of 10 kpc).

5. Conclusion

We have provided the first MAXI/GSC source catalog at low Galactic latitudes, $|b| < 10°$, outside the Galactic center region ($|b| < 5°$, $l < 30°$, and $l > 330°$), based on the data obtained in 7 years from 2009 August 13 to 2016 July 31. To overcome source confusion in crowded regions, we have accurately calibrated the PSF of each GSC camera and improved the background model by utilizing the onboard data. We have also taken into account the contribution of the Galactic ridge X-ray emission employing the model in Revnivtsev et al. (2006). Finally, we have detected 221 sources with a detection significance of $s_{D,4-10\,\mathrm{keV}} > 6.5$, 180 of which have 1 or more counterpart (s) after cross-matching with other X-ray catalogs. The 73-day bin light curves over 7 years, and their periodograms for all the cataloged sources, are presented. To complete sample information, we are working on the identification of the remaining sources, whose results will be reported in future papers.

We thank Dr. Kyuseok Oh for sharing the *Swift*/BAT 105 month catalog with us prior to publication. Part of this work was financially supported by Grants-in-Aid for JSPS Fellows (T.H., T.K.) and for Scientific Research 17H06362 (Y.U., N.K., T.M., H.N., and A.Y.), 16K17672 (M.S.), 16K17667(Y.

Table 8
Mean Properties for Each Source Type

Category	Number of Sources[a]	$\sigma^2_{\rm rms}$ [a,b]	HR1[a,c]	HR2[a,d]
Unidentified	13	0.126	0.13 ± 0.05	−0.13 ± 0.11
Blazars	12	0.111	0.04 ± 0.02	−0.11 ± 0.11
Galaxy Clusters	11	−0.018	0.02 ± 0.03	−0.45 ± 0.10
Seyfert Galaxies	29	0.028	0.18 ± 0.03	0.12 ± 0.04
Cataclysmic Variables	17	0.043	0.27 ± 0.04	0.07 ± 0.10
Stars	8	0.116	0.13 ± 0.07	−0.34 ± 0.13
Isolated Pulsars	8	0.038	0.22 ± 0.12	0.05 ± 0.04
Supernova Remnants	5	0.001	−0.32 ± 0.20	−0.30 ± 0.17
High Mass X-ray Binaries	42	0.205	0.31 ± 0.03	0.13 ± 0.04
Low Mass X-ray Binaries	34	0.127	0.09 ± 0.04	−0.09 ± 0.04
X-ray Binary[e]	1	10.38	−0.02	0.10
Unmatched	41	0.119	0.11 ± 0.04	−0.06 ± 0.06

Notes.
[a] 73-day sources are included.
[b] The median of excess variance calculated by Equation (3).
[c] The mean and its standard deviation of HR(3–4 keV, 4–10 keV) calculated by Equation (2).
[d] The mean and its standard deviation of HR(4–10 keV, 10–20 keV) calculated by Equation (2).
[e] The X-ray binary whose donor star is not firmly identified (MAXI J1836–194).

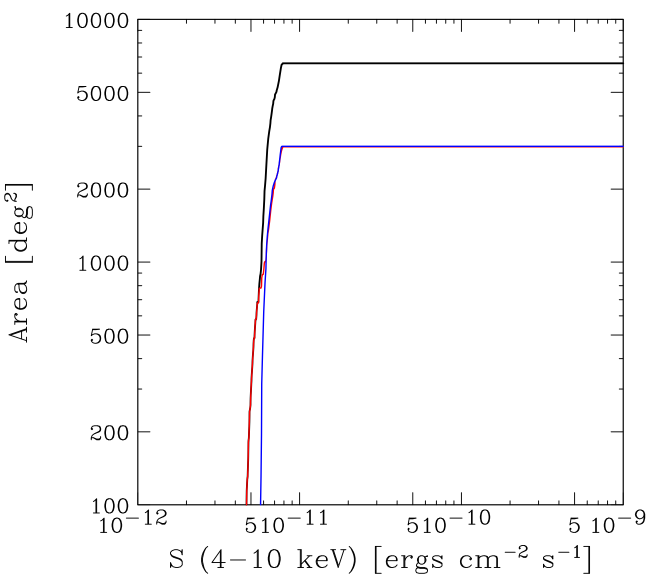

Figure 10. Survey area as a function of limiting sensitivity in the 4–10 keV band for $s_{D,4-10\,\rm keV} > 6.5$ (black: the whole survey area, red: $l = 30°–105°$ and $l = 255°–330°$, blue: $l = 105°–255°$).

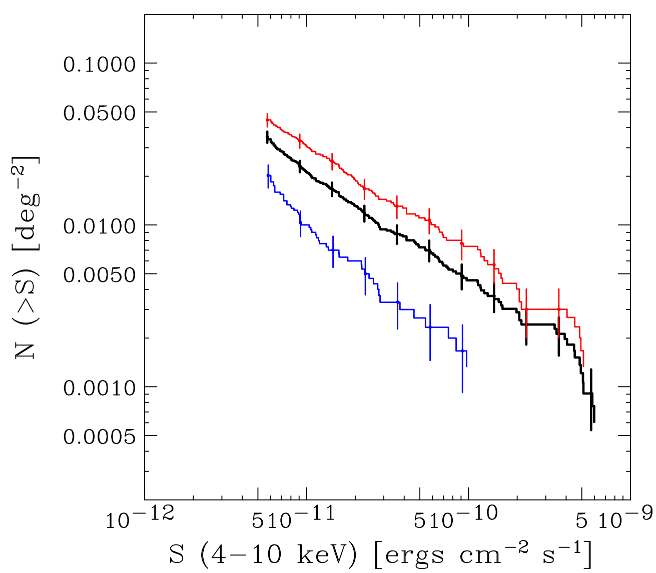

Figure 11. Spatially averaged log N–log S relations in the 4–10 keV band of the 7-year sources at $|b| < 10°$ (black: from the whole survey area, red: from the $l = 30°–105°$ and $l = 255°–330°$ region, blue: from the $l = 105°–255°$ region). The attached error bars correspond to 1σ.

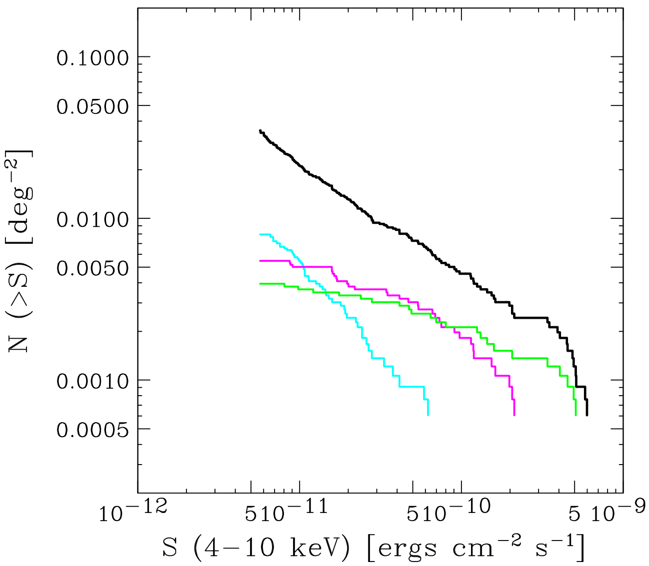

Figure 12. Spatially averaged log N–log S relations in the 4–10 keV band obtained from the whole survey area for different populations (black: total, green: LMXBs, magenta: HMXBs, cyan: extragalactic).

S.), and 17K05392(Y.T.) from the Ministry of Education, Culture, Sports, Science and Technology (MEXT) of Japan. Y. T. thanks Ryo Sasaki for a useful discussion on stellar X-ray emission. M.S. acknowledges support by the Special Postdoctoral Researchers Program at RIKEN.

Appendix
PSF Calibration

In Hiroi et al. (2013), the PSF of the GSC was assumed to have a two-dimensional Gaussian profile in the coordinate system based on the collimator angle (ϕ and θ; see Sugizaki et al. 2011, for the definition) around the original source positions. However, the actual profile deviates from the Gaussian in the direction of the anode wires (i.e., the ϕ axis), due to the variation in the position where photons are absorbed in the gas counters, which depends on their incident angles and the energy of photons. In addition, the finite slit width makes the profile broader (see Sugizaki et al. 2011). These effects are negligible for most X-ray sources compared with their

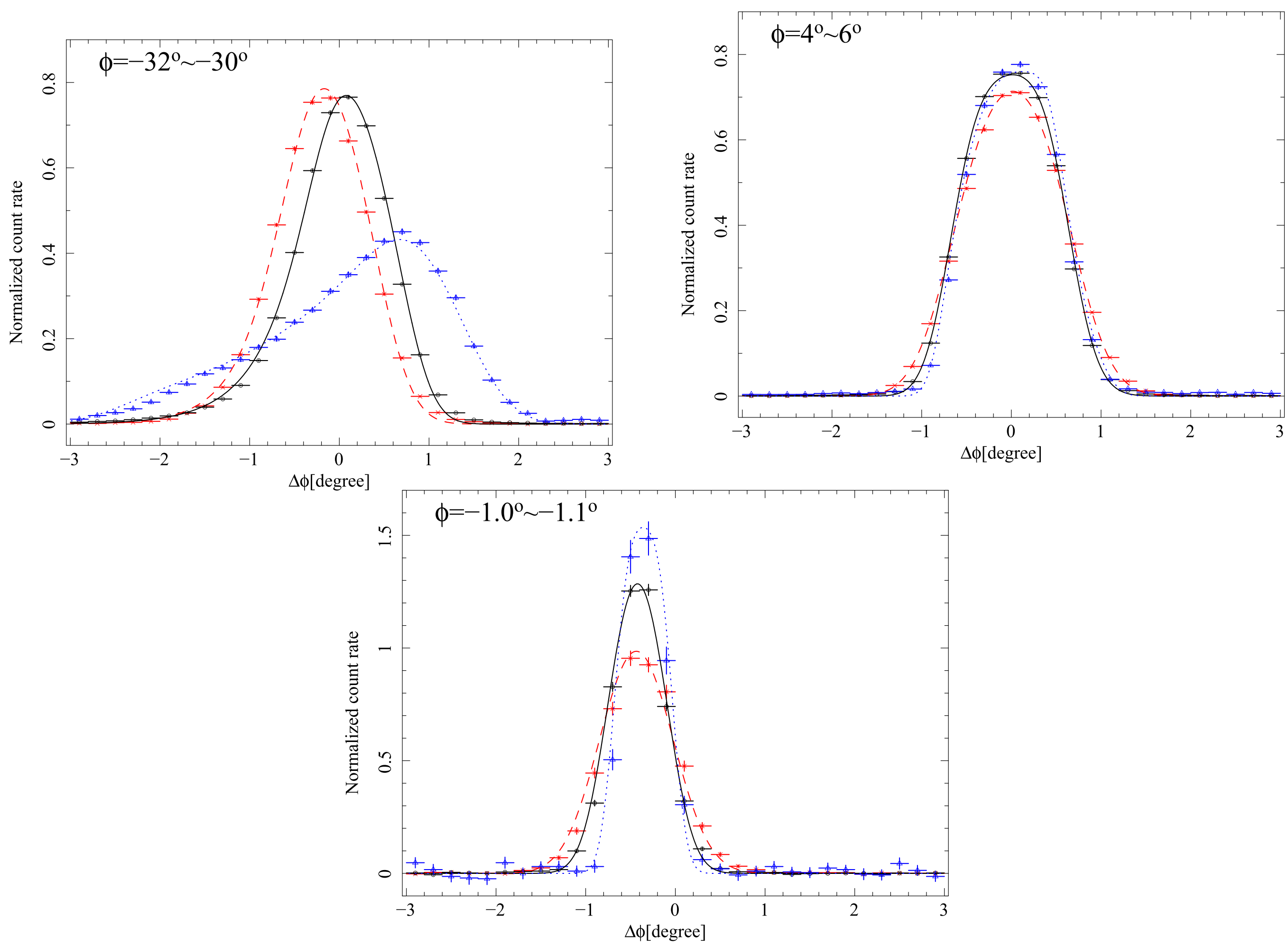

Figure 13. PSF cross-section profiles of GSC5 with an anode voltage of 1650 V and their best-fit models along the detector anode-wire direction at (a) $\phi = -32^\circ \sim -30^\circ$, (b) $4^\circ \sim 6^\circ$, (c) $-1.1^\circ \sim 1^\circ\!.0$ in 3–4 keV (crosses and red dashed line), 4–10 keV (circles and black solid line), and 10–20 keV (triangles and blue dotted line).

statistical errors, but significant in brightest Galactic sources, such as Sco X-1, Crab Nebula, and Cyg X-1.

To measure the actual PSF profile in each camera, we collected the event data from several brightest isolated sources, such as Sco X-1, and Crab, and integrated them separately for each incident angle and energy band. Figures 13(a)–(c) show the PSF cross-sectional profiles obtained from the real event data, with their best-fit models in the 3–4 keV, 4–10 keV, and 10–20 keV bands, along the anode-wire direction for incident angles (ϕ) of $-32°$ to $-30°$, $4°$ to $6°$, and $-1\overset{\circ}{.}1$ to $-1\overset{\circ}{.}0$, respectively. As noted in Figure 13(a), the PSF shapes at larger ϕ becomes more asymmetric at higher energies, because higher-energy photons travel deeper before being absorbed in the gas counter and the effects of variation in the photon-absorption position become more significant. Narrower PSFs are formed at $\phi \sim 0°$ (Figure 13(c)), due to the shielding effect by the support structure of the counter's beryllium window, perpendicular to the anode wires. We note that the width of the PSF profile also depends on the voltage of the anode wires, 1650 or 1550 V.

Considering the results above, we constructed a PSF database and used it in the simulation for the sources detected in the image analysis Section 3. The database consists of FITS files of PSF data for each camera and each anode voltage (1550 and 1650 V). In these files the PSF profiles along the wire anodes are tabulated as histograms separately for each ϕ range, and in energy bands of 3–4 keV, 4–10 keV and 10–20 keV, in a proper format that *maxisim* can refer to.

ORCID iDs

T. Hori https://orcid.org/0000-0001-8204-790X
Y. Ueda https://orcid.org/0000-0001-7821-6715
T. Kawamuro https://orcid.org/0000-0002-6808-2052
N. Kawai https://orcid.org/0000-0001-9656-0261
A. Tanimoto https://orcid.org/0000-0002-0114-5581
Y. Sugawara https://orcid.org/0000-0001-6749-1199

References

Baumgartner, W. H., Tueller, J., Markwardt, C. B., et al. 2013, ApJS, 207, 19
Bird, A. J., Bazzano, A., Bassani, L., et al. 2010, ApJS, 186, 1
Bird, A. J., Bazzano, A., Malizia, A., et al. 2016, ApJS, 223, 15
Bird, A. J., Malizia, A., Bazzano, A., et al. 2007, ApJS, 170, 175
Cash, W. 1979, ApJ, 228, 939
Cooke, B. A., Griffiths, R. E., & Pounds, K. A. 1970, in IAU Symp. 37, Non-Solar X- and Gamma-Ray Astronomy, ed. L. Gratton (Dordrecht: Reidel), 280
Ebisawa, K., Bourban, G., Bodaghee, A., Mowlavi, N., & Courvoisier, T. J.-L. 2003, A&A, 411, L59
Ebisawa, K., Tsujimoto, M., Paizis, A., et al. 2005, ApJ, 635, 214
Eguchi, S., Hiroi, K., Ueda, Y., et al. 2009, in Proc. of the RIKEN Symp., 44
Forman, W., Jones, C., Cominsky, L., et al. 1978, ApJS, 38, 357
Górski, K. M., Hivon, E., Banday, A. J., et al. 2005, ApJ, 622, 759
Grimm, H.-J., Gilfanov, M., & Sunyaev, R. 2002, A&A, 391, 923
Grindlay, J. E., Hong, J., Zhao, P., et al. 2005, ApJ, 635, 920
Hands, A. D. P., Warwick, R. S., Watson, M. G., & Helfand, D. J. 2004, MNRAS, 351, 31
Hiroi, K., Ueda, Y., Hayashida, M., et al. 2013, ApJS, 207, 36
Hiroi, K., Ueda, Y., Isobe, N., et al. 2011, PASJ, 63, S677
Islam, N., & Paul, B. 2016, NewA, 47, 81
Isobe, N., Sato, R., Ueda, Y., et al. 2015, ApJ, 798, 27
Matsuoka, M., Kawasaki, K., Ueno, S., et al. 2009, PASJ, 61, 999
Mihara, T., Nakajima, M., Sugizaki, M., et al. 2011, PASJ, 63, S623
Mitsuda, K., Inoue, H., Koyama, K., et al. 1984, PASJ, 36, 741
Nagase, F. 1989, PASJ, 41, 1
Nebot Gómez-Morán, A., Motch, C., Barcons, X., et al. 2013, A&A, 553, A12
Negoro, H., Kohama, M., Serino, M., et al. 2016, PASJ, 68, S1
Oh, K., Koss, M., Markwardt, C. B., et al. 2018, ApJS, 235, 4
Papadakis, I. E., & Lawrence, A. 1993, MNRAS, 261, 612
Piffaretti, R., Arnaud, M., Pratt, G. W., Pointecouteau, E., & Melin, J.-B. 2011, A&A, 534, A109
Revnivtsev, M., Sazonov, S., Gilfanov, M., Churazov, E., & Sunyaev, R. 2006, A&A, 452, 169
Revnivtsev, M., Sazonov, S., Jahoda, K., & Gilfanov, M. 2004, A&A, 418, 927
Saxton, R. D., Read, A. M., Esquej, P., et al. 2008, A&A, 480, 611
Sugimoto, J., Kitamoto, S., Mihara, T., & Matsuoka, M. 2017, PASJ, 69, 52
Sugizaki, M., Mihara, T., Serino, M., et al. 2011, PASJ, 63, S635
Sugizaki, M., Mitsuda, K., Kaneda, H., et al. 2001, ApJS, 134, 77
Vaughan, S., Edelson, R., Warwick, R. S., & Uttley, P. 2003, MNRAS, 345, 1271
Voges, W., Aschenbach, B., Boller, T., et al. 1999, A&A, 349, 389
Wilson-Hodge, C. A., Cherry, M. L., Case, G. L., et al. 2011, ApJL, 727, L40
Wood, K. S., Meekins, J. F., Yentis, D. J., et al. 1984, ApJS, 56, 507
Yamauchi, S., & Koyama, K. 1993, ApJ, 404, 620